

DARK NOISE AND THE APO-OPSIN EFFECT IN RETINAL RODS AND CONES

by

Daniel Silverman

A dissertation submitted to the Johns Hopkins University in conformity with the  
requirements for the degree of Doctor of Philosophy

Baltimore, Maryland

October 2018

## Abstract

Our visual system is exceedingly complex, but initiating light detection requires only a small number of reactions in retinal rods and cones. In the first stages of vision, the exact nature of signal amplification and dark noise is still uncertain. For dim-light vision in rods, one photoexcited rhodopsin was long reported to activate several hundred downstream effector molecules during the single-photon response. This extremely high gain at the receptor-to-effector step has been challenged more recently, but estimates remain dispersed and rely on some non-intact-rod measurements. With two independent approaches, using exclusively intact mouse rods, we obtained measurements of the electrical effect from a single-downstream-effector complex, which was only ~12- to 14-fold smaller than the single-photon response. If downstream effector responses sum linearly, our estimate for the effective signal amplification in rods is only ~12 to 14 effectors per photoexcited rhodopsin. From these experiments, we also found that rod apo-opsin, after photoexcitation of rhodopsin and release of chromophore, produces single-downstream-effector responses occurring randomly approximately once per day. After apo-opsin re-conjugates to chromophore, rhodopsin is more than  $\sim 10^4$ -fold more stable, limiting the rate of “false” activation events in darkness to only one in ~160 years on average. Many mutations in rhodopsin have been implicated in visual impairment, with speculation that, in certain cases, altered amplification or dark noise may be the underlying cause. We have also developed an approach to isolate activity from rhodopsin mutants in mouse rods to elucidate their role in disrupting vision. Separately, we have investigated fundamental questions about signal amplification, dark noise, and apo-opsin activity in cones and in unique photoreceptors that express hybrid rod/cone visual pigments.

## Acknowledgments

While many experiments were done in the solitude of a darkroom, I am very fortunate to have colleagues, friends, and family who have provided feedback and ideas as well as moral support during this work. I have learned a great deal in the past six years and was able to persevere thanks to those around me.

Thank you to King-Wai Yau for giving me the opportunity to work in his laboratory. When I was applying to graduate school, I came across a recent publication from his laboratory on the activation of visual pigments by light and heat (1), and was captivated by the question of how the thermal stability of visual pigments affects light-detection in the nervous system. After working with King for a number of years, I have seen how much thought and effort he puts into every paper. I greatly appreciate King's dedication to research and to doing things well.

Wendy Yue, Dong-Gen Luo, Li-Hui Cao, and Chih-Chun Lin have each helped me in one way or another to optimize the suction-pipette recording technique. These recordings take patience and persistence, and this group of people had worked tirelessly to maintain a high standard for stable, low noise data before I joined the lab. I have also benefited greatly from scientific discussions with Wendy Yue, who always provides thoughtful feedback and suggestions during our research planning, data analysis, and of course, unexpected troubleshooting to maintain equipment.

Qian Wang, Yanghui Sheng, Lujing Chen, Rongchang Li, Xiaozhi Ren, Zheng Jiang, Tian Xue, Xiaojun Li, Parinaz Bina, and Zuying Chai have provided engaging scientific discussions and technical advice. I admire their work ethic and it has always

been enjoyable to learn about their research progress and how they have overcome challenges.

Terry Shelley in the Department of Neuroscience Machine Shop has been one of my closest friends during my time here. Not only has he provided invaluable technical support, but also has frequently initiated thought-provoking conversations, provided life advice, and shared countless jokes.

Liusong Ding, the laboratory manager, has been instrumental in all aspects of our research by performing routine genotyping, purchasing reagents, and helping to maintain crucial equipment. He also frequently shared interesting foods during lab meetings and lunches (including bamboo, chicken feet, and homegrown vegetables from his garden).

I would like to give a special thanks to my thesis committee Jeremy Nathans, Elizabeth Glowatzki, and Randall Reed for the discussions of our progress over the years and for their continued support, advice, and interesting insights.

I would also like to thank our collaborators Rikard Frederiksen, Jeannie Chen, M. Carter Cornwall, Kazumi Sakai, Takahiro Yamashita, and Yoshinori Shichida for providing important data for the completion of this work.

I am grateful to the Biochemistry, Cellular and Molecular Biology graduate program and especially Carolyn Machamer and Arhonda Gogos for providing a supportive and collegial environment for biological research. I hope to maintain friendships with the 2012 entering class (Mateusz Dobrowolski, Caitlyn Bowman, Phil Cox, Donald Freed, Leah Greenspan, Kapil Ramachandran, Tyler Wied, Rebecca Keener, He Gu, Sara Sanders, Liz Calzada, Tu Lu, Yulong Liu, Yi Zhou, Shih-Chin Wang, Nathalie Gerassimov, Neil Neumann, Terry Clister, Shih-Chin Wang, Toby, Zhuwei Xu, and Samarjeet Samarjeet).

Finally, I am most fortunate to have a family that has supported me throughout my life. My parents, Ann and Ken, exemplify the virtues of hard work, persistence, and compassion. My younger brother, Jake Silverman, is a passionate and creative person and I have enjoyed attending his concerts in Baltimore and Washington D.C. during graduate school. I am also greatly indebted to my wife, Anna Q. Han, who has gotten me to the finish line of graduate school through her understanding during late work nights as well as her encouragement, sense of humor, and keen problem solving. Anna's family, Steve, Feng, and Philip, has provided many family dinners and rounds of Mahjong for enjoyable weekend diversions. My aunt, Susan, has also been supportive throughout and has given us some of her paintings to brighten our home.

## **Author Contributions**

Chapter 2 describes research designed by D. Silverman, W. W. S. Yue, and K-W. Yau and executed in close collaboration with W. W. S. Yue.

Chapter 3 describes research designed by D. Silverman and K-W. Yau and executed in close collaboration with Z. Chai, P. Bina, and W. W. S. Yue.

Chapter 4 describes research designed by D-G. Luo, K-W. Yau, and D. Silverman and executed by D-G. Luo and D. Silverman.

Chapter 5 describes research designed by D. Silverman and K-W. Yau and executed in collaboration with R. Frederiksen.

Figures produced by others are indicated in figure legends.

In memory of Nikolai Maximay and David T. Yue

## Table of Contents

Abstract.....	ii
Acknowledgments.....	iii
Author Contributions .....	vi
List of Figures.....	xi
List of Tables .....	xiii
Chapter 1. Introduction .....	1
1.1 How vision begins.....	1
1.2 Signal amplification and the apo-opsin effect in rods.....	2
1.3 Dark noise and visual impairment from rhodopsin mutants .....	3
1.4 Dark noise and the apo-opsin effect in cones.....	3
1.5 Hybrid rod/cone pigments.....	5
1.6 Future questions .....	6
1.7 Figures.....	7
Chapter 2. The apo-opsin effect and amplification in rod phototransduction .....	17
2.1 Past work on Rho*-to-G <sub>T</sub> * amplification factor in rods. ....	17
2.2 Introduction .....	19
2.3 Wild-type apo-opsin (WT-Opn) produces detectable electrical noise after a bleach. .....	21
2.4 A WT-Opn Molecule Constitutively Produces ~1 Single-G <sub>T</sub> *·PDE* Effect Per Day. ....	23
2.5 Mutation at Rho’s ERY-Motif Severely Reduces G <sub>T</sub> Activation in Mouse Rods without Affecting Downstream Phototransduction Cascade. ....	25
2.6 Unitary Response of <i>REY</i> Rods Represents Single-G <sub>T</sub> *·PDE* Effect. ....	27
2.7 Number of Single-G <sub>T</sub> *·PDE* Effects Produced Per WT-Rho* During the Single- Photon Response. ....	30
2.8 Discussion .....	32
2.9 Figures.....	37
Chapter 3. Dark noise and visual impairment from a rhodopsin mutant .....	57
3.1 Past work on pigment noise theory .....	57
3.2 Introduction.....	58
3.3 Measuring mutant-Rho activity in mouse rods .....	61
3.4 Estimating mutant-Rho content from the probability of failure.....	62



3.5 Dark noise and the thermal isomerization rate of mutant Rho in mouse rods .....	63
3.6 Activation-energy barrier for isomerization.....	64
3.7 Accessibility of the chromophore-binding pocket .....	65
3.8 Degeneration caused by D190N-Rho and its relationship to transducin signaling. 65	
3.9 Discussion .....	67
3.10 Figures.....	68
Chapter 4. Dark noise and the apo-opsin effect in cones.....	75
4.1 Introduction .....	75
4.2 Sensitivity and Response Kinetics of Goldfish Red-, Green- and Blue-Sensitive Cones.....	77
4.3 GTP-Dependent PDE Activity in Darkness.....	78
4.4 Quantitative Measurement of PDE Activity in Darkness. ....	80
4.5 Dark GTP-dependent PDE activity and the “equivalent” background light.....	81
4.6 Background-Light Adaptation.....	85
4.7 Discussion .....	86
4.8 Figures.....	87
Chapter 5. Hybrid rod/cone pigments.....	101
5.1 Introduction .....	101
5.2 Alligator rhodopsin .....	102
5.3 Tokay gecko pigments .....	103
5.4 Discussion .....	104
5.5 Figures.....	105
Chapter 6. Methods.....	109
6.1 Physiology (Chapters 2, 3, 4, 5).....	109
6.2 Suction-pipette recording from mouse rods (Chapters 2, 3).....	109
6.3 Photobleaching (Chapter 2).....	110
6.4 Bleaching calculations (Chapter 2) .....	112
6.5 Analysis of post-bleach noise (Chapter 2) .....	113
6.6 Validation of Campbell’s theorem (Chapter 2).....	114
6.7 Power Spectral Analysis (Chapter 2) .....	115
6.8 Incubation with 11- <i>cis</i> -retinal (Chapter 2).....	116
6.9 Quantal analysis (Chapters 2, 3, 5) .....	116
6.10 Measurement of thermal isomerization noise (Chapters 2, 3, 5) .....	117

6.11 Western blot (Chapter 2).....	117
6.12 Immunohistochemistry (Chapter 2) .....	119
6.13 Isoelectric focusing to quantify pigment content (Chapter 3).....	120
6.14 Histology (Chapter 3).....	121
6.15 Microspectrophotometry measurements from mouse rods (Chapters 2 and 3) ..	122
6.16 Quantitative RT-PCR of D190N-Rho (Chapter 3).....	123
6.17 Generation of Rho <sup>Opn1MW</sup> knock-in mice (Chapter 3) .....	123
6.18 Mouse retina.....	124
6.19 List of mouse lines (Chapters 2, 3) .....	125
6.20 Retinae from other vertebrates (Chapters 4, 5) .....	126
6.21 Suction-pipette recordings from goldfish cones (Chapter 4) .....	127
6.22 Truncated-cone recordings (Chapter 4).....	128
6.23 Cell identification, light stimuli (Chapter 4).....	128
6.24 Quantitative analysis of truncated-cone recordings (Chapter 4).....	129
6.25 Weber-Fechner relation in goldfish cones (Chapter 4) .....	130
6.26 Application of 11- <i>cis</i> -retinal A1 and 11- <i>cis</i> -retinal A2 to goldfish cones during a suction-pipette recordings (Chapter 4).....	130
6.27 Suction-pipette recordings from alligator rods (Chapter 5) .....	130
6.28 Microspectrophotometry measurements from alligator rods (Chapter 5).....	131
6.29 Animal care and use (Chapters 2, 3, 4, 5) .....	132
6.30 Figures .....	133
References.....	139
Appendix.....	150
A.1 Convolution of 2 exponential-decay functions .....	150
A.2 Convolution of 3 exponential-decay functions: .....	151
A.3 Convolution of 4 exponential-decay functions: .....	152
A.4 Shape Factor for the convolution of 2 exponential-decay functions.....	153
A.5 Convolution of the single-G <sub>T</sub> *·PDE* electrical response with the REY-Rho*· G <sub>T</sub> *·PDE* lifetime probability density function:.....	154
A.6 Convolution of the single-G <sub>T</sub> * response with the REY-R* lifetime distribution (Example):.....	155
A.7 Simulating a Poisson Process in MATLAB:.....	155
CURRICULUM VITAE FOR Ph.D. CANDIDATES .....	158

## List of Figures

Figure 1-1. Horizontal section through a human eye.....	7
Figure 1-2. Diagram of retinal circuitry and human retinal cross-section.....	8
Figure 1-3. Mutations found in genes implicated in autosomal dominant retinitis pigmentosa.....	11
Figure 1-4. The phototransduction pathway in rods and cones.....	12
Figure 1-5. The peak-absorption wavelength distributions of visual pigments.....	14
Figure 1-6. Rods and cones from various vertebrate species.....	16
Figure 2-1. Post-bleach noise from Opn in <i>Rho</i> <sup>WT/WT</sup> ; <i>Gcaps</i> <sup>-/-</sup> rods.....	38
Figure 2-2. Generation and characterization of <i>Gnat1</i> <sup>Tg</sup> ; <i>Gnat1</i> <sup>-/-</sup> mice.....	40
Figure 2-3. Unitary events underlying constitutive Opn-triggered activity in <i>Rho</i> <sup>WT/WT</sup> ; <i>Gcaps</i> <sup>-/-</sup> rods.....	42
Figure 2-4. Characterization of <i>Rho</i> <sup>REY/REY</sup> ; <i>Gcaps</i> <sup>-/-</sup> retinae and heterologously expressed REY-Rho.....	44
Figure 2-5. Photoresponses of <i>REY</i> rods.....	45
Figure 2-6. Estimate of single-G <sub>T</sub> * effect from REY-Rho* responses.....	47
Figure 2-7. Comparison of individual G <sub>T</sub> * effects with the unitary WT-Rho* response.....	49
Figure 2-8. Dominant time constants in various genotypes and cell conditions.....	50
Figure 2-9. Evaluation of Opn noise in dark-adapted rods.....	52
Figure 2-10. Kinetics of Meta-II formation and decay for WT- and REY-Rho.....	54
Figure 3-1. D190N-Rho responses can be isolated and quantified by largely silencing G-protein signaling from endogenous Rho.....	69
Figure 3-2. Dark noise from D190N-Rho and WT-Rho.....	70
Figure 3-3. The activation-energy barrier for isomerization is unchanged in D190N-Rho.....	71
Figure 3-4. Retinal degeneration caused by D190N-Rho is not rescued by removing G <sub>T</sub> α.....	74
Figure 4-1. Flash-response properties of goldfish photoreceptors.....	87
Figure 4-2. Truncated cone preparation.....	88
Figure 4-3. GTP-dependent PDE dark activities in cones.....	89

Figure 4-4. Quantification of PDE dark activities. ....	90
Figure 4-5. “Equivalent” dark light for PDE dark activities.....	91
Figure 4-6. Collected data of “equivalent” dark light.....	92
Figure 4-7. Effect of 11- <i>cis</i> -retinal exposure on the sensitivity of goldfish red cones....	93
Figure 4-8. “Equivalent” background light of apo-opsin in red cones. ....	95
Figure 4-9. Cone adaptation by steady light. ....	97
Figure 4-10. The effect of background light on response kinetics. ....	98
Figure 4-11. Deleterious effects of prolonged 11- <i>cis</i> -retinal exposure. ....	100
Figure 5-1. Rod-like dark noise, sensitivity, and response kinetics measured from dark-adapted alligator rods.....	105
Figure 5-2. Minimal chromophore-exchange of rhodopsin in alligator rods measured by microspectrophotometry. ....	107
Figure 5-3. Amino acid sequence alignment of C-termini from various visual pigments. ....	108
Figure 6-1. Suction-pipette Recording.....	133
Figure 6-2. Bleaching to produce apo-opsin in rods.....	134
Figure 6-3. Validation of bleaching procedures and calculations.....	136
Figure 6-4. Validation of Campbell’s Theorem by Poisson Process Simulation. ....	137
Figure 6-5. Suction-pipette recording from various animals. ....	138

## List of Tables

Table 1-1. Genes implicated in autosomal dominant retinitis pigmentosa.....	9
Table 2-1. Parameters from noise analysis of mouse rods of various bleaching levels....	55
Table 2-2a. Parameters of flash responses of mouse rods of various genotypes.....	56
Table 2-2b. Parameters of flash responses of mouse rods after various bleaching levels.	56
Table 3-1. Parameters of flash responses of mouse rods for evaluating effects of D190N-Rho.....	72
Table 3-2. Parameters of dark noise for evaluating effects of D190N-Rho .....	72
Table 4-1. Comparison of red cone dimensions, dark current, and sensitivity.....	96
Table 4-2. Effects of 11- <i>cis</i> -retinal on goldfish cones and the “equivalent” background light of apo-opsin activity .....	96
Table 5-1. Comparison of rod outer segment dimensions, sensitivity and kinetics .....	106

## Chapter 1. Introduction

### 1.1 How vision begins

The perception of light occurs effortlessly the moment we open our eyes. This requires signal amplification following photon absorption by rod and cone photoreceptors in the retina (Fig. 1-1) as well as extremely low thermal noise throughout retinal circuitry (Fig. 1-2). Light perception is one of the most fundamental functions of our nervous system and yet it can be significantly deteriorated by a host of monogenic retinal disorders (Table 1-1 and Fig. 1-3). Rhodopsin initiates dim-light vision, and numerous rhodopsin mutants have been implicated in retinal degeneration and night blindness [Fig. 1-3b, (2–4)], but the exact role of these mutants in visual impairment is still being actively investigated. Even though rhodopsin was first discovered more than 140 years ago, the phototransduction cascade (Fig. 1-4)—the series of molecular events signaling light detection in both rods and cones—has only been uncovered within the past few decades, allowing for a deeper understanding of how vision begins in health and disease.

Rods and cones differ in their response kinetics, sensitivity, and ability to adapt to steady light allowing for vision down to our perception of perhaps only ~5 photons in the middle of the night and across a  $10^9$ -fold range of light intensity on a sunny day. The major rod- and cone-specific genes involved in phototransduction have been identified and many macromolecular structures solved, but quantitative details of the process are still not generally agreed upon. In this thesis, I examine fundamental properties of signal amplification and dark noise in rod and cone phototransduction, as well as certain intriguing aspects of hybrid visual pigments and phototransduction in unique animals.

## 1.2 Signal amplification and the apo-opsin effect in rods

For decades, extensive debate has focused on the magnitude of signal amplification during the single-photon response mediated by a single rhodopsin molecule in rods. One major obstacle has been that all estimates relied on variable measurements of the rate of G-protein activation by photoexcited rhodopsin in disrupted outer segment fragments at room temperature (requiring somewhat uncertain temperature correction to 37°C), and some disagreement about the active lifetime of rhodopsin (5–9). To perhaps circumvent these issues, in **Chapter 2**, we have focused on quantifying the electrical effect of a single G-protein/phosphodiesterase molecular complex in intact mouse rods and discuss how this measurement may provide a straightforward estimate of signal amplification in rods. To quantify this effect, I studied the exceedingly weak signaling of apo-opsin in mouse rods, believed to be many orders of magnitude less effective at signaling than photoexcited rhodopsin – an ability so weak that the unitary apo-opsin effect may correspond to the activation of a single downstream effector. We found that the unitary-apo-opsin effect matches closely with the unitary response from a rhodopsin mutant with a substantially-weakened G-protein binding site and we concluded that both measurements indeed correspond to the elementary electrical effect of a G-protein/phosphodiesterase complex in rods. Comparing these measurements to the single-photon response from wild-type rhodopsin, we were able to estimate the amplification factor at the receptor-to-effector step in rod phototransduction. Importantly, our estimate is based entirely on measurements from intact rods at physiological temperature (37°C).

### **1.3 Dark noise and visual impairment from rhodopsin mutants**

Relatively high signal amplification in rods is important for our incredible photosensitivity in darkness. Hecht et al. first demonstrated that a healthy dark-adapted human observer can perceive a light stimulus leading to only ~5 to 8 absorbed photons (10). This feat also requires an extremely quiet dark noise imparted by rhodopsin's thermal stability, nonetheless giving rise to occasional "false" activation in darkness that the nervous system confuses with real light (11). Over 100 rhodopsin mutants have been implicated in retinal degeneration and night blindness [Fig. 1-3b; (12)], with speculation that some of these mutants may augment rhodopsin's dark isomerization rate (13, 14). Only a few animal models expressing rhodopsin mutants have been developed, and there is still great uncertainty about whether particular mutants actually produce higher amounts of dark noise in the outer segment. This uncertainty is largely due to the difficulty in distinguishing mutant rhodopsin activity from that of endogenous rhodopsin in mouse rods. In **Chapter 3**, I describe an approach to isolate, for the first time, light responses and dark noise from D190N-rhodopsin to better understand its role in disease.

### **1.4 Dark noise and the apo-opsin effect in cones**

Compared to rods, much less is known about signal amplification at the receptor-to-effector step as well as the exact amount of dark noise in cones, which mediate vision across an extensive range of light intensity with rapid response recovery as well as fast pigment regeneration. There has been speculation that relatively high dark noise, measured qualitatively, in red-sensitive cones (also referred to simply as red cones) acts as an "equivalent" background light that speeds response kinetics and lowers sensitivity in much



the same way as adaptation to real light (15, 16). The red cone pigment is in fact less stable than rhodopsin, with a lower energy barrier for isomerization indicated by a longer wavelength (lower energy) of peak absorption (17, 18). Thus, it has been shown that the salamander red cone pigment does produce considerable dark noise in salamander red cones (19).

Very little has been reported about the exact amounts of dark noise produced in other cone types, and even in red cones, dark noise has not been thoroughly quantified. The peak-absorption wavelength of cone pigments varies much more widely than that of rod pigments (Fig. 1-5a,b), not only allowing for color vision, but also providing a wide range of dark noise across cone types. Pigments from some fish (including goldfish), amphibians, and reptiles are conjugated to a unique chromophore known as 11-*cis*-3,4-dehydroretinal derived from Vitamin A2 instead of 11-*cis*-retinal from Vitamin A1 (Fig. 1-5c), which expands the spectral range to longer peak-absorption wavelengths. The functional consequences of such a range in thermal isomerization noise in cones is not yet understood. Additionally, cone pigments are known to spontaneously dissociate from 11-*cis*-retinal without isomerization (20, 21), yielding cone-apo-opsin and some level of its constitutive activity (21). To quantify each potential source of dark noise in various cone types and to study the relationship between dark noise and cone function, in **Chapter 4**, we studied acutely-isolated goldfish cones to quantify dark noise and signal amplification in red, green, and blue cones. Using a truncated-cone preparation, spontaneous signaling in darkness was quantified from GTP-dependent and GTP-independent sources. To determine if any apo-opsin was present in dark-adapted goldfish cones contributing constitutive GTP-dependent signaling, I measured the effect of 11-*cis*-retinal exposure (A1

and A2) on the sensitivity of goldfish cones. Dark noise in goldfish red cones was highest, followed by that of green cones, and lowest in blue cones, in which GTP-dependent spontaneous activity was undetectable. Red and green cones indeed appeared to contain apo-opsin molecules that would contribute to dark GTP-dependent activity.

### **1.5 Hybrid rod/cone pigments**

The majority of rod and cone pigments have distinctive physical properties that segregate according to the cell type where they are expressed (22). Rhodopsins, expressed in rods across the animal kingdom, are extremely stable in darkness, have a closed/inaccessible chromophore-binding pocket, and a relatively slow decay of photointermediates after isomerization. Cone pigments, have a range of stability according to their wide range of peak-absorption wavelengths, have an open/accessible chromophore-binding pocket, and exhibit a relatively fast decay of photointermediates. The photoreceptors where rod and cone pigments are expressed are also functionally segregated in various animals. In all known cases, rods have low dark noise, high sensitivity, and slow response kinetics, while cones have variable amounts of dark noise, lower sensitivity, and faster response kinetics (23, 24). In Chapter 5, we consider examples of intermediate visual pigments, from alligator (25) and from a nocturnal gecko (26, 27), that share properties of rhodopsin and of cone pigments. It is still not known how these pigments function in situ and whether their amino acid sequences may help to identify residues influencing thermal isomerization or photointermediate decay.

## 1.6 Future questions

In retinae from certain species of fish, reptiles, birds, and primates there is a specialized region of densely-packed cones known as the fovea. The primate fovea – crucial for seeing fine details – is made up of morphologically distinct cones, each with its own direct line of communication to a midget ganglion cell via a single midget bipolar cell (28). While my focus has been on fundamental aspects of phototransduction studied in peripheral rods and cones, it is important to consider ultimately making comparisons with the physiology of foveal cones. Interestingly, there has been a recent report that foveal cones have slower response kinetics than peripheral cones (29). The reason for these kinetic differences was proposed to come from differences in phototransduction between peripheral and foveal cones, but the exact mechanism is still unknown.

Finally, rod phototransduction serves as a model GPCR-mediated system in that it is one of the most accessible and quantifiable signaling pathways. The methodology and analysis developed to study the single-photon response and dark noise in rods could be adapted to other sensory systems for comparison. Using very brief stimuli would allow for isolation of the impulse response to study signaling reaction kinetics and using fluctuation analysis would allow for estimation of the elementary response (e.g. that produced by a single active receptor). While these approaches have been used to study olfactory transduction (30), little is known about how signal amplification and noise compares across the diversity of GPCR pathways in the body.

## 1.7 Figures

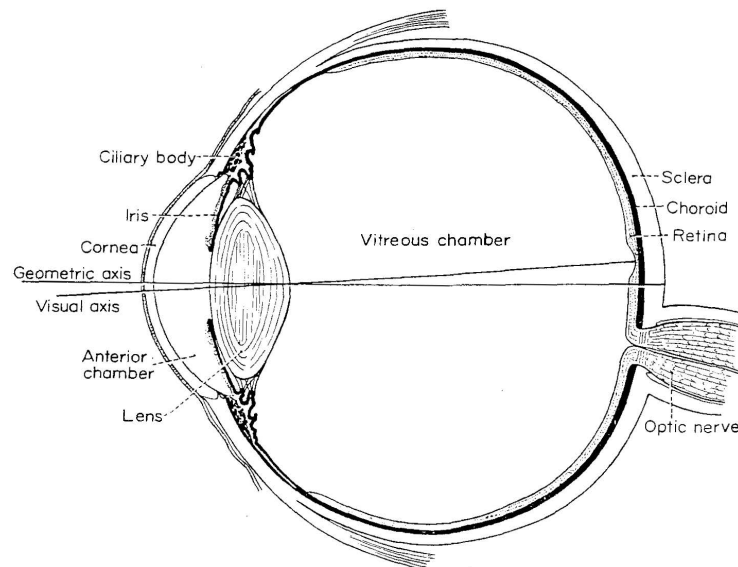


**Figure 1-1. Horizontal section through a human eye.** The outermost, opaque layer is called the sclera, and blocks light from entering the eye except where the sclera is absent at the transparent cornea. Beneath the sclera is a melanin-pigmented vascular layer that nourishes the outer layers of the retina. The amount of light entering the eye is controlled by a contractile iris sphincter muscle, anterior to the lens, and surrounding the pupil aperture. Light is refracted when passing through the cornea and then again when passing through the lens. The position of an image entering the eye is controlled by the shape of the lens, which can be adjusted by contraction of the ciliary muscle. Vision begins when photons in an image are absorbed by photoreceptors in the retina and visual information is transmitted to the brain via the optic nerve. High-acuity vision occurs at the fovea, which is slightly off-centered in the retina. The position of light rays entering the eye can be defined with respect to the center of the eye (geometric axis) or with respect to the center of the fovea (visual axis) Anatomical drawing from (31).

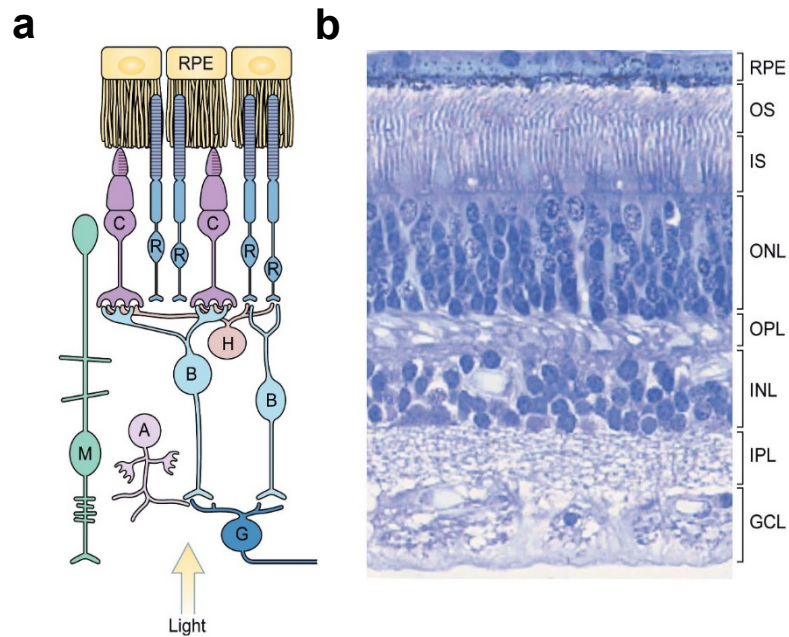


**Figure 1-2. Diagram of retinal circuitry and human retinal cross-section.** **a**, The mouse retina and the peripheral human retina are similarly organized into circuits stratified in layers formed by five neuronal classes (rods, R; cones, C; bipolar cells, B; ganglion cells, G; horizontal cells, H; and amacrine cells, A; as well as one glial cell type called the Müller glia, M). Retinal pigment epithelium cells (RPE) are involved in regenerating visual pigments in photoreceptor outer segments. **b**, Histological cross-section of peripheral human retina. Photons pass through the entire retina before being absorbed by visual pigments in the photoreceptor outer segment layer (OS). The inner segment (IS) mediates protein trafficking between photoreceptor cell bodies and their outer segments. The outer nuclear layer (ONL) consists of photoreceptor cell bodies that extend processes into the outer plexiform layer (OPL) where the bipolar cells synapse with rod and cone terminals. Bipolar cell bodies form much of the inner nuclear layer (INL) and their axons project to the inner plexiform layer (IPL), forming synapses with amacrine cells or retinal ganglion cells with cell bodies in the ganglion cell layer (GCL). The particular morphology and synaptic connections of a ganglion cell allow the cell to process information about certain features of a visual image. Figure adapted from (32).

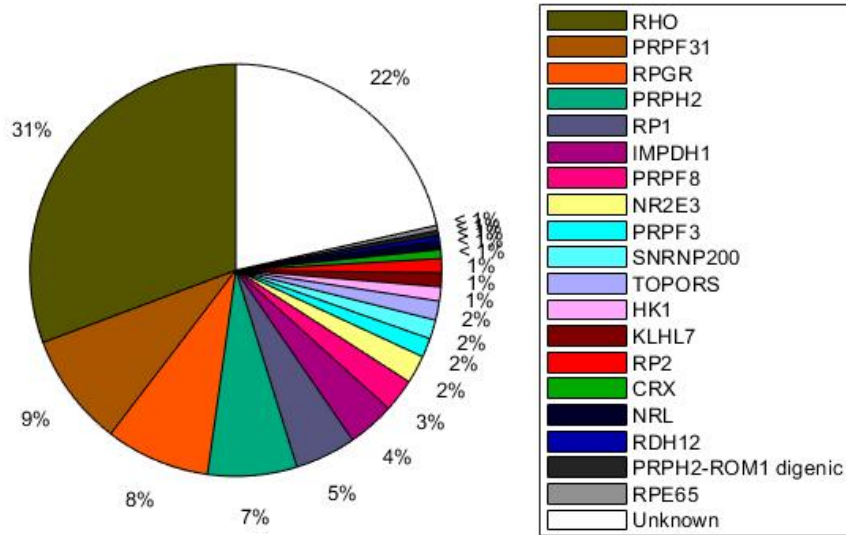
**Table 1-1. Genes implicated in autosomal dominant retinitis pigmentosa**

Gene	Description	Some additional disorders involving this gene	General physiological function
RHO, OPN2	Rhodopsin	Dominant congenital stationary night blindness	Phototransduction Outer segment structure
GUCA1B	Guanylate cyclase activating protein 1B	Dominant macular dystrophy	Phototransduction Ca <sup>2+</sup> -dependent negative feedback
RPE65	Retinal pigment epithelium-specific 65 kD protein	Recessive Leber congenital amaurosis	Visual cycle
RDH12	Retinol dehydrogenase 12	Recessive Leber congenital amaurosis	Visual cycle
PRPH2	Peripherin 2	Dominant macular dystrophy Dominant cone-rod dystrophy	Outer segment structure
ROM1	Retinal outer segment membrane protein 1	Digenic retinitis pigmentosa with PRPH2	Outer segment structure

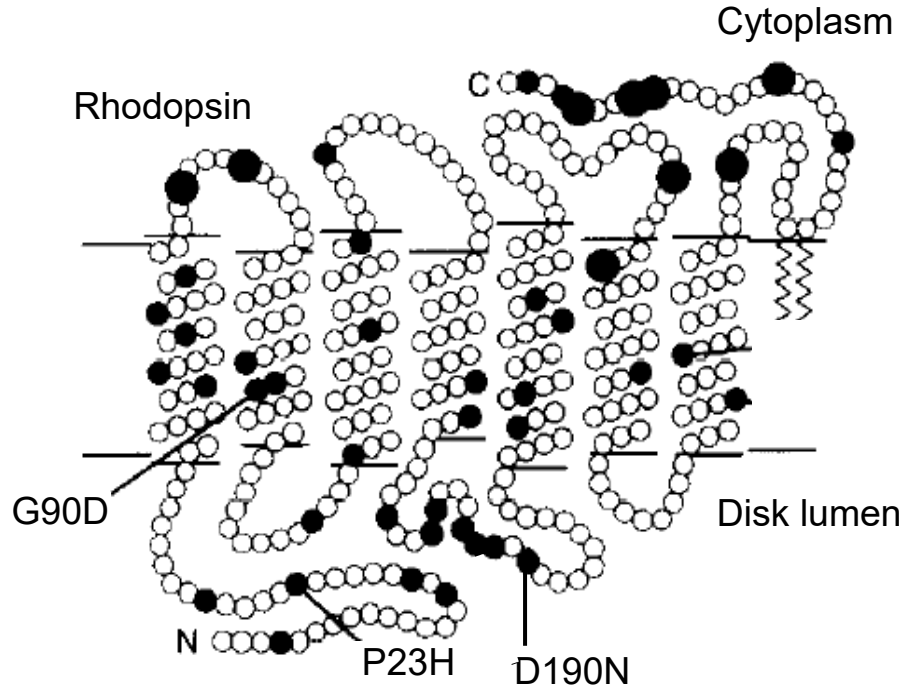
Several well-known genes where mutations have been found to be involved in autosomal dominant retinitis pigmentosa. Adapted from (33).

**a**

### Proportion of Mutations in Genes Implicated in Autosomal Dominant Retinitis Pigmentosa

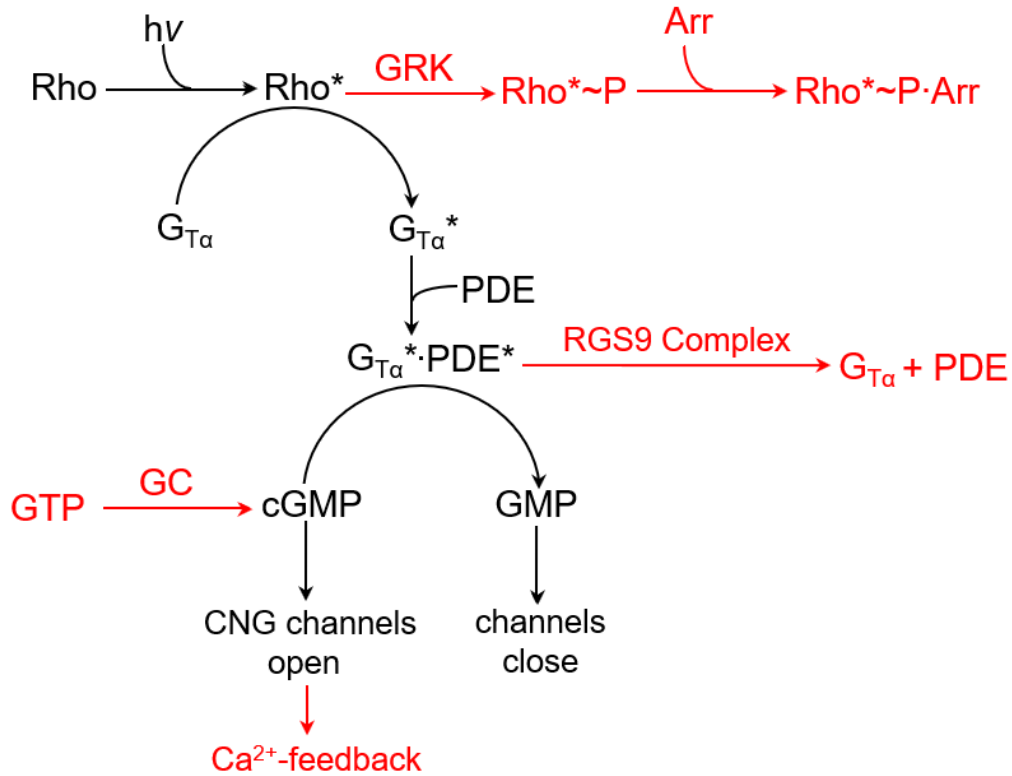


**b**

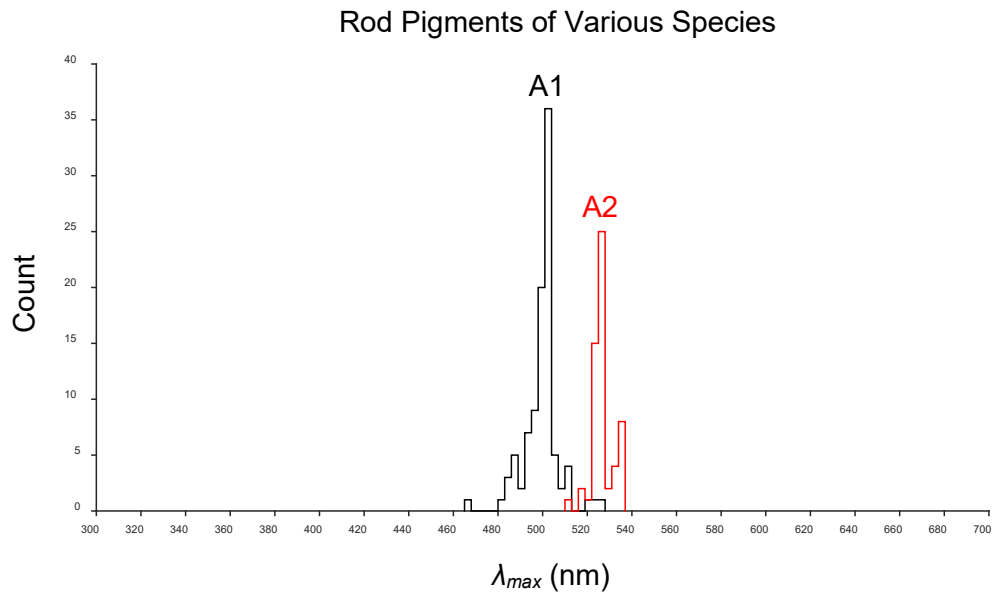
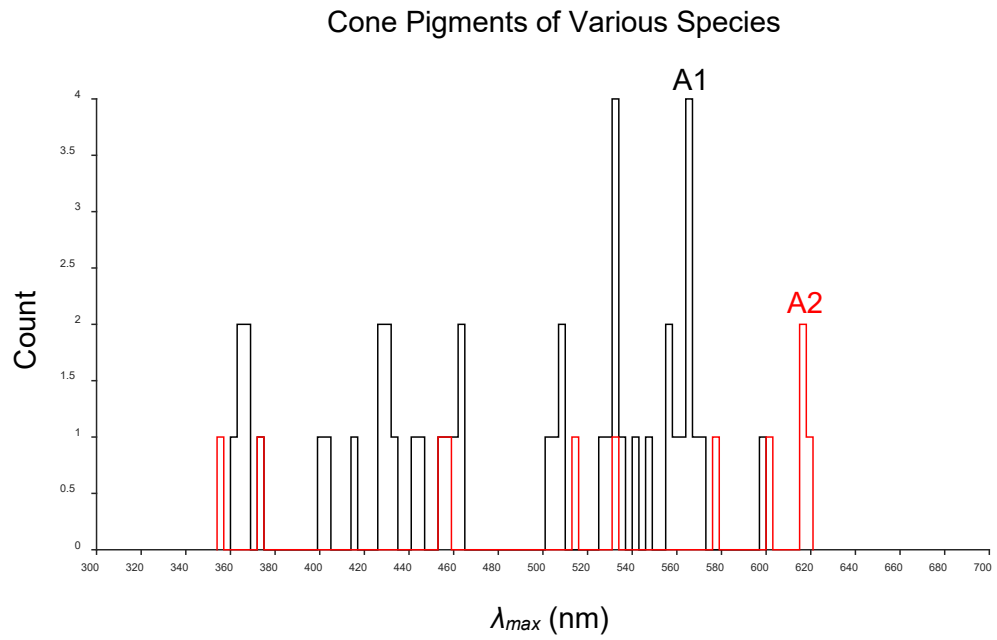
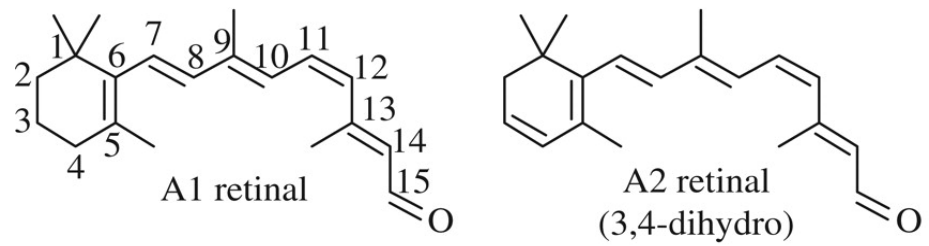


**Figure 1-3. Mutations found in genes implicated in autosomal dominant retinitis pigmentosa.** **a**, Proportions of various mutations found across 270 families with autosomal dominant retinitis pigmentosa. Adapted from (33). Among these mutations, 30.7% were found in RHO. **b**, Secondary structure of rhodopsin showing the position of mutations implicated in congenital stationary night blindness (e.g. G90D) and autosomal dominant retinitis pigmentosa (e.g. P23H and D190N). Small filled symbols are missense mutations. Large filled symbols are insertions, deletions, frameshift, and nonsense mutations. Adapted from (4).





**Figure 1-4. The phototransduction pathway in rods and cones.** Vision begins when photon absorption triggers isomerization of rod or cone visual pigments (Rho\* or P\*) that catalyze GTP-for-GDP exchange on a number of G-protein molecules (G<sub>Tα</sub>\*), which in turn disinhibit phosphodiesterase (PDE) molecules leading to the hydrolysis of cGMP molecules resulting in the closure of cGMP-gated ion channels and ultimately membrane hyperpolarization as the electrical signal processed by the visual system. Response termination steps are shown in red: i) quenching of Rho\* activity by phosphorylation (mediated by GRK-1 in rods), and arrestin binding (Arrestin-1 in rods) ii) deactivation of the G<sub>Tα</sub>\*·PDE\* complex by GTP hydrolysis (enhanced through interaction with the RGS9-1 complex, iii) restoration of dark cGMP content by guanylate cyclase (RETGC1 and RETGC2 in rods), which catalyzes the production of cGMP from GTP, and iv) Ca<sup>2+</sup>-dependent negative feedback at multiple stages of the cascade.

**a****b****c**

**Figure 1-5. The peak-absorption wavelength distributions of visual pigments. a,** Histogram showing the distribution of peak-absorption wavelengths ( $\lambda_{max}$ ) of wild type rod pigments from various animal species obtained from difference spectra of retinal extracts or microspectrophotometry (34). **b,** Histogram showing the distribution of peak-absorption wavelengths ( $\lambda_{max}$ ) of wild type cone pigments from various animal species obtained from microspectrophotometry or heterologous expression of cloned genes [e.g. Refs. (35, 36)]. **c,** Structures of 11-*cis*-retinal (A1 form) and 11-*cis*-3,4-dehydroretinal (A2 form). Pigments conjugated to A1 are shown in black and pigments conjugated to A2 are shown in red.

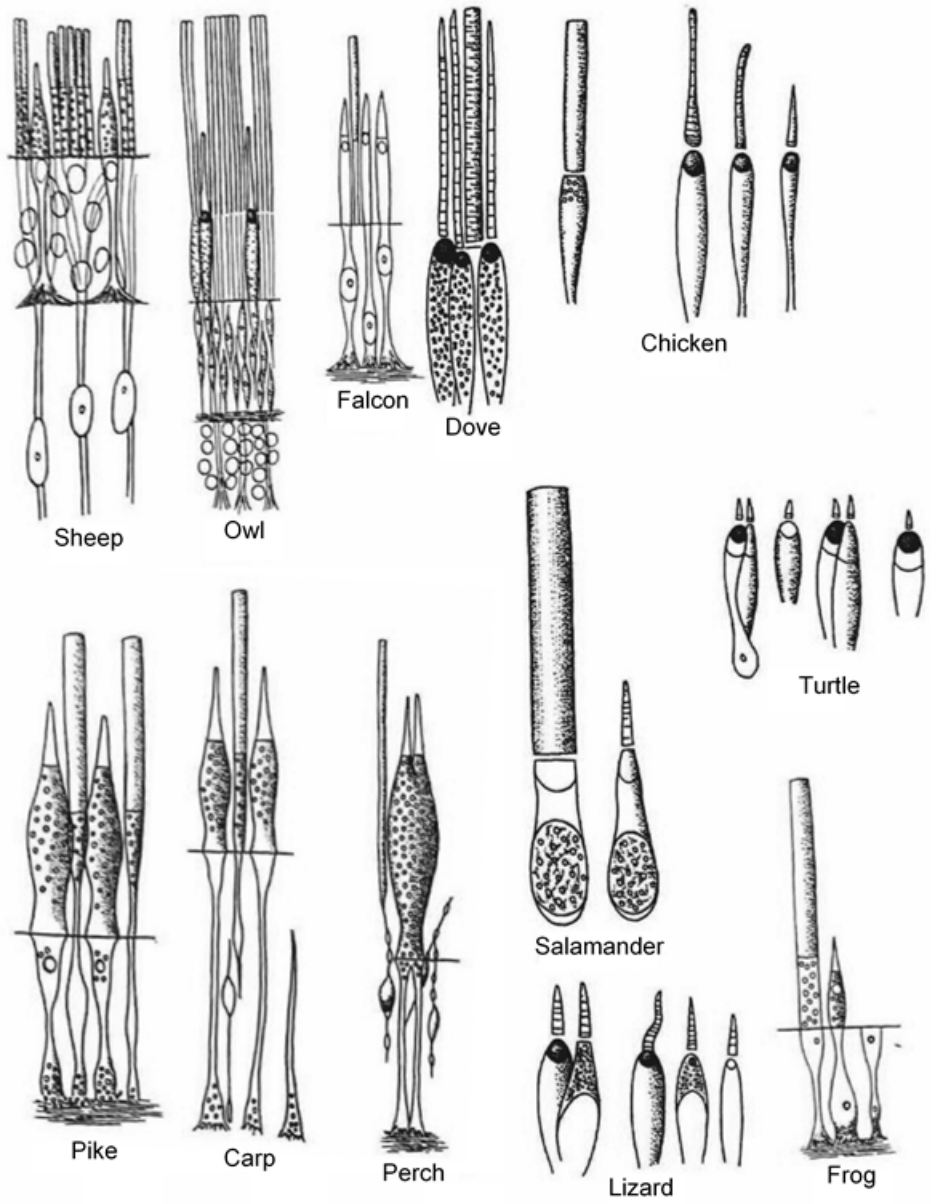


**Figure 1-6. Rods and cones from various vertebrate species.** The outer segment is an elongated cilium developed from an extensive plasma membrane and many membranous structures stacked perpendicular to the cell's long axis. This orientation holds visual pigments, and specifically their chromophore dipoles, in position for photon absorption (aligned with the electric vector of incident light). The visual pigment concentration is as high as ~3 to 3.5 mM in single rod and cone outer segments from a variety of species (37, 38). All known rod and cone (ciliary) vertebrate photoreceptors employ a similar transduction pathway for image-forming vision (39). The dimensions of photoreceptors, however, are highly variable. The membranous structures housing pigments in rods are intracellular disks, whereas in cones, they are part of a tortuous plasma membrane providing a faster route for chromophore regeneration of cone pigments. Drawings of rods and cones from (40).

## Chapter 2. The apo-opsin effect and amplification in rod phototransduction

### 2.1 Past work on Rho\*-to-G<sub>T</sub>\* amplification factor in rods.

Before the present work, the amplification factor at the Rho\*-to-G<sub>T</sub>\* step in rod phototransduction has been extensively studied, derivable from the multiplicative product of the G<sub>T</sub>-activation rate by a Rho\* ( $\nu_{RG}$ ) and Rho\*'s lifetime ( $\tau_R$ ). Results, however, have been highly variable,. The  $\nu_{RG}$  value, reviewed in Refs. (41–43), at room temperature measured with nucleotide-binding from disrupted rod outer segment (ROS) membranes (6, 44–48) or pH changes produced by PDE\* activity (49) ranged from 20-300 G<sub>T</sub>\* s<sup>-1</sup> per Rho\* in amphibian (6, 46–48) and from 12-800 G<sub>T</sub>\* s<sup>-1</sup> per Rho\* in mammal (44, 45, 49). Separate measurements from near-infrared-light-scattering studies on ROS membrane preparations, dissociated-rod suspensions or intact retinæ during visible-light stimulation at room temperature (5, 50–53) gave a much higher  $\nu_{RG}$  value of ~1000 G<sub>T</sub>\* s<sup>-1</sup> per Rho\* in amphibian and >3,300 G<sub>T</sub>\* s<sup>-1</sup> per Rho\* in mammal (5, 50), but the exact nature of the scattered-light signal is uncertain (6, 42). Thus, for multiple reasons – varied experimental conditions including non-native preparations, required correction to 37 °C, and uncertain signal interpretation – significant imprecision still exists in the estimation of  $\nu_{RG}$ .

Separately, Rho\*'s  $\tau_R$  is also equivocal in value, although less serious than  $\nu_{RG}$  because at least the more recent measurements were all from intact mammalian rods. In some elegant experiments (7), it was concluded that  $\tau_R$  in mouse rods might be ≤80 msec (37 °C), later reduced to ~40 msec with further experiments and computational modeling (54). Values broadly similar (55) or somewhat larger (9), with integration time of 60-70 msec, were subsequently reported/proposed. However, a much larger estimate (~0.4 sec)

has also been suggested (8). Additionally, estimates of  $\tau_R$  have been made with amphibian rods at room temperature by using elaborate experimental manipulations and computational modeling (involving a truncated-rod preparation and computational modeling), giving  $\tau_R$  values as high as  $\sim 2.8$  sec at room temperature (56, 57).

Currently, a fairly prevalent value in the field for the Rho\*-to-G<sub>T</sub>\* amplification factor is  $\sim 16$  G<sub>T</sub>\* per Rho\* at 37°C (43), calculated from a  $\nu_{RG}$  of  $\sim 400$  G<sub>T</sub>\* s<sup>-1</sup> per Rho\* [temperature-corrected to at 37°C from a measured  $\sim 150$  G<sub>T</sub>\* s<sup>-1</sup> per Rho\* at room temperature obtained with “optimized” radiolabeled-nucleotide binding in amphibian ROS fragments (6) and a Rho\*  $\tau_R$  of  $\sim 40$  msec mentioned above (54)]. Nonetheless, a  $\nu_{RG}$  of 1,000 G<sub>T</sub>\* s<sup>-1</sup> per Rho\* at 37°C [based on light scattering measurements (52)] was still adopted most recently in a modeling study (58).

Overall, the amplification factor at the Rho\*-to-G<sub>T</sub>\* step in rods is leaning toward lower values, although still far from reaching universal agreement. Perhaps owing to the diverse estimates over the years, the notion of a lower gain has not penetrated into the general scientific community, despite the widespread importance of GPCR signaling. As a result, the early publicized concept of a high amplification of hundreds of G<sub>T</sub>\* per Rho\*, based on a  $\nu_{RG}$  of  $\sim 1000$  G<sub>T</sub>\* s<sup>-1</sup> per Rho\* in fragmented frog ROSs and a purely hypothetical Rho\*  $\tau_R$  of  $\sim 0.5$  sec at room temperature (5), has continued to take hold, being still frequently quoted in textbooks and even generalized to other GPCR pathways (see 2.2).

## 2.2 Introduction

G-protein-coupled receptors (GPCRs) function in diverse neurophysiological pathways such as sensory transduction, synaptic transmission, hormone signaling, neuroinflammatory responses, as well as many other pathways outside of the nervous system. Over past decades, there has been an ever-expanding identification of GPCRs and their downstream signaling components in various cell types. Furthermore, advances in structural biology and biochemistry have elucidated the different conformational states of GPCRs and the downstream components' molecular interacting domains. Nonetheless, much less is known about the dynamics of these component interactions, especially in the native neuronal environment.

Rod phototransduction in many ways has been a particularly useful model of GPCR signaling. Apart from being one of the very first GPCR pathways discovered, the high photosensitivity of rods permits their light response to be resolved and analyzed down to the level of action of a single photoactivated rhodopsin molecule (Rho\*) [i.e., single-photon response, (59)], providing an important basis for understanding phototransduction and signal processing through the retinal circuitry. Rho\* activates the G-protein transducin ( $G_T$ ), which in turn activates a cGMP-phosphodiesterase (PDE) to hydrolyze cGMP, lowering the latter's concentration and closing some cyclic-nucleotide-gated (CNG), non-selective cation channels that are open in darkness. Early work suggested that many hundreds of active  $G_T$  molecules ( $G_T^*$ s) are generated by a single Rho\* [Ref. (5)], with each  $G_T^*$  (consisting of its  $\alpha$ -subunit,  $G_{T\alpha}$ , with GTP bound) then activating a PDE molecular complex (60) (represented by  $G_T^* \cdot PDE^*$ ). A large  $G_T^*/Rho^*$  ratio thus offered seemingly an attractive amplification mechanism for producing the high photosensitivity



of rods (5). For over thirty years, this concept of high gain from rhodopsin to G protein has taken hold as a textbook dogma (61–63), to such an extent as to become also a general signature of GPCR signaling (61, 64, 65). Although this high gain in phototransduction has subsequently been challenged (43), later estimates nonetheless are not all in agreement, and above all still depend partly on non-intact rod measurements and/or computational modeling with uncertain validity (Supplementary Text). As such, the widespread concept of high gain at the receptor-to-G-protein step has largely persisted even today. At the same time, this large amplification has discouraged further dissection of the single-photon response into its constituent single- $G_T^* \cdot PDE^*$  effects for a more thorough understanding of the visual process.

In this work, we present the very first measurements of the single- $G_T^* \cdot PDE^*$  effect in live, intact rods by two independent methods that exploit specific situations conferring weak signaling to  $G_T^*$ . We took advantage of the weak constitutive activity (66) of wild-type apo-opsin (WT-Opn, i.e., photobleached Rho, which lacks chromophore) in order to quantify the randomly triggered single- $G_T^* \cdot PDE^*$  effects occurring in darkness. Independently, a targeted mutation of rhodopsin's G-protein-binding site (REY-Rho) (67, 68) allowed us to extract a light-evoked single- $G_T^* \cdot PDE^*$  effect in native mouse rods. Among a number of observations, we most importantly found that the wild-type single-photon response is composed probably of only 12-14  $G_T^* \cdot PDE^*$ s, contrary to the long-held belief of a much larger number. We provide a rationalization for this new picture of GPCR signaling.

### 2.3 Wild-type apo-opsin (WT-Opn) produces detectable electrical noise after a bleach.

To evaluate the single- $G_T^* \cdot PDE^*$  effect, we quantified the constitutive activity of wild-type apo-opsin in darkness (WT-Opn, i.e., Rho without chromophore). Cornwall and Fain (66) first established Opn's constitutive activity, reporting each Opn molecule in salamander to be  $\sim 10^{-7}$ -fold as effective in activating transduction as a steady light producing  $\sim 1 \text{ Rho}^* \text{ sec}^{-1}$ , thus exceedingly weak in activity [see also Ref. (69)]. A similar observation was made in mouse rods (70). We interpret this huge quantitative difference in activity between  $\text{Rho}^*$  and Opn to reflect one or both of two factors: (i) the very low probability of Opn being active (such as, formally, by occasionally transitioning into an active state,  $\text{Opn}^*$ , i.e.,  $\text{Opn} \xrightleftharpoons{\quad} \text{Opn}^*$ ), and (ii) a very low probability of  $\text{Opn}^*$  successfully producing any  $G_T^*$ . Our rationale nonetheless is that, no matter how unlikely to occur, the unitary event underlying this activity should still involve no less than a single- $G_T^* \cdot PDE^*$  effect.

Fig. 2-1a shows a continuous recording in darkness from a *WT* rod (in *Gcaps*<sup>-/-</sup> background) subjected to an intense light pulse at time zero that saturated the response and produced an  $\sim 1\%$  bleach of the cell's rhodopsin (Methods). The *Gcaps*<sup>-/-</sup> genotype removed in rods the expression of the guanylate-cyclase-activating proteins (71), GCAP1 and GCAP2, which normally regulate cGMP synthesis via  $\text{Ca}^{2+}$ -feedback to produce light adaptation in phototransduction. The single-photon response of *Gcaps*<sup>-/-</sup> rods is  $\sim 5$ -fold as large as normal (71), therefore facilitated our data analysis of small signals. Before bleaching, the dark current was relatively quiet except for some level of "continuous" noise (11, 72) and occasional blips ("discrete" events) representing spontaneous (thermal)

isomerization of single Rho molecules (1, 11). After bleaching, the slowly-recovering dark current became much noisier for minutes, reflecting sustained Rho\* activity (73, 74). Also, this increase in noise arose partly from constitutive Opn activity. In order to focus on Opn-associated noise, we kept the rods in darkness for 1-3 hours after a bleach to allow a near-complete decay of Rho\* to Opn (70) before proceeding to recordings (Methods). Normally, Opn *in situ* would not persist indefinitely because of its reversion to Rho by free chromophore from the retinal pigment epithelium (RPE); in our preparation, however, this regeneration did not occur because the RPE was removed (Methods). It was literally impossible to record for multiple hours from the same cell both before and after bleaching, so we compared averaged data from cohorts of unbleached and bleached cells.

Fig. 2-1b shows sample dark recordings from *WT* rods, either unbleached (left) or at different times after a 5% bleach (right), indicating the elevated dark noise long after bleaching. We confirmed that the post-bleach noise arose from constitutive activation of  $G_T$  due to Opn because it quieted down upon converting Opn to Rho with exogenous 11-*cis*-retinal (Fig. 2-1b, right bottom). The aggregate presence of Opn led to random unitary Opn\* effects that summated (similar to responses triggered by a dim steady light) to produce a post-bleach shift (slight decrease) in the mean dark current and an increase in the dark-current variance. In the collected data of Fig. 2-1c, top and bottom, the horizontal blue lines indicate cohort-averaged mean and noise variance of post-5%-bleach dark current against time, versus cohort-averaged control dark values (black lines), both excluding visible discrete events (marked by stars in Fig. 2-1b; see Methods). These post-bleach parameters returned close to unbleached levels upon regeneration of Opn to Rho by exogenous 11-*cis*-retinal (green lines; Methods). Incidentally, incubating unbleached,

dark-adapted mouse rods with 11-*cis*-retinal did not have any obvious effect on dark noise (Fig. 2-9), confirming previous reports of negligible Opn in the absence of bleaching (21, 75–77).

The cohort difference in values between pre- and post-bleach dark-current means and variances measured above can be analyzed to extract the amplitude and the frequency of the unitary responses (78, 79), as described below.

#### **2. 4 A WT-Opn Molecule Constitutively Produces ~1 Single-G<sub>T</sub>\*·PDE\* Effect Per Day.**

In the 5%-bleach experiment of Fig. 2-1b,c, the changes in steady-dark-current mean and noise variance increased linearly ( $R^2 = 0.95$  and  $0.99$ , respectively) with the number of WT-Opn's produced by bleaching (Table 2-1), consistent with a Poisson process underlying the occurrence of WT-Opn-associated electrical events. With this premise, the event amplitude is given by the post-bleach dark current's variance/mean ratio (i.e., after subtracting unbleached dark values; Methods), taking into account the underlying unitary event's waveform determined from the cohort-averaged difference power spectrum (Fig. 2-1d and Chapter 6). The unitary-event frequency could then be calculated from either the post-bleach noise variance or the change in steady mean current (Methods). In this manner, we obtained a unitary-event amplitude ( $a'$ ) of  $0.29 \pm 0.10$  pA and an event frequency of  $15.5 \pm 5.8$  sec<sup>-1</sup> (mean  $\pm$  SD,  $n = 15$  cells). Corresponding experiments with 1% and 8% bleaches gave similar  $a'$  values and event waveforms, with event frequencies roughly in proportion to the number of Opn's formed as one might expect (Figs. 2-2a, b and Table 2-1).

To check whether the above Opn-associated events indeed represented single- $G_T^* \cdot PDE^*$  effects, we repeated the bleaching experiments with *Gnat1<sup>Tg</sup>;Gnat1<sup>-/-</sup>;Rho<sup>WT/WT</sup>;Gcaps<sup>-/-</sup>* mouse rods, which under-expressed  $G_T\alpha$  drastically (Fig. 2-3). Despite an event waveform with a moderately slower decay (Fig. 2-2c and Table 2-1) – this being in parallel to the slower recovery of the unitary light response described below for this genotype (inset in Fig. 2-6c left) – as well as a stronger bleach required for achieving a comparable post-bleach noise (Fig. 2-2d), such  $G_T\alpha$ -underexpressing rods nonetheless gave  $a'$  values similar to those for rods with normal  $G_T\alpha$  level (Fig. 2-2e and Table 2-1). In short, each post-bleach unitary event is indeed likely to be mediated by one  $G_T^* \cdot PDE^*$ .

Unlike the roughly constant profile of the unitary Opn-associated effect, the single-photon-response decreased progressively in amplitude with higher bleaches (Fig. 2-2f and legend; Table 2-2b). Thus, bleaching appeared to reduce the number of  $G_T^*$ s activated by a  $Rho^*$ , due probably in part to a shorter  $Rho^*$ 's lifetime (Fig. 2-8 and legend).

In the plot of event rate against opsin content [Fig. 2-2b, right, taking  $6.5 \times 10^7$  rhodopsins per mouse rod (1)], the slope of the linear-regression line (dashed; constrained to go through the origin) gives a molecular rate constant for WT-Opn of  $8.6 \times 10^{-6}$  events  $\text{sec}^{-1}$ . In other words, each WT-Opn molecule *in situ* constitutively elicits an electrical response mediated by one  $G_T^* \cdot PDE^*$  at a frequency of about once per  $\sim 1.3$  days at 37°C. In comparison, an *in situ* rhodopsin molecule at 37°C spontaneously and irreversibly isomerizes in  $\sim 160$  years on average (1, 18, 80). Thus, 11-*cis*-retinal serves as an extremely effective negative agonist by reducing WT-Opn's constitutive activity rate by  $\sim 4.5 \times 10^4$ -fold, while simultaneously rendering rhodopsin photosensitive and giving a single-photon response more than an order of magnitude larger than the noise events from an Opn\*. Thus,

by being able to resolve the unitary-event amplitude triggered by an  $\text{Opn}^*$ , we also succeeded for the first time in quantifying the “effective” temporal stability of  $\text{Opn}$  *in situ* (only “effective” because the  $\text{Opn} \xrightarrow{\text{Rho}^*} \text{Opn}^*$  transitions could be more frequent, but only a fraction led to  $\text{G}_T^*$ ).

Being the decay end-product of  $\text{Rho}^*$ ,  $\text{Opn}$  is reported to remain heterogeneously phosphorylated for many hours afterwards, at least in the high-bleach condition (50-70% bleach), and the subsequent dephosphorylation is accelerated by lactate (81). However, we did not observe any increase in post-5%-bleach noise after adding 4-mM lactate to the BSA-Locke’s solution for storing the bleached retina (not shown). Bleaching also induces arrestin/transducin translocations between the rod outer segment and inner segment (82, 83), although such translocations may have recovered during the long time period experienced in our experiments. At the low bleaching levels we used, there is no easy way to quantify with single-cell precision the various  $\text{Opn}$  phosphorylation states or the degrees of arrestin/transducin translocations for correlation with noise measurements. If these phenomena did persist in our post-bleach measurements and affect  $\text{Opn}$ ’s constitutive activity, this in principle would not affect our derived single- $\text{G}_T^* \cdot \text{PDE}^*$  effect profile but would potentially affect the molecular rate of  $\text{Opn}$ ’s constitutive activity – for example if dephosphorylated  $\text{Opn}$  produces  $\text{G}_T^*$ s more frequently.

## **2. 5 Mutation at Rho’s ERY-Motif Severely Reduces $\text{G}_T$ Activation in Mouse Rods without Affecting Downstream Phototransduction Cascade.**

Another strategy for measuring the single- $\text{G}_T^* \cdot \text{PDE}^*$  effect in intact rods was to reduce drastically the affinity of  $\text{Rho}^*$  for  $\text{G}_T$  so that a  $\text{Rho}^*$  would activate at most one

$G_T^*$  in its active lifetime, i.e., being unproductive in most cases, and only occasionally leading to a single  $G_T^*$  according to the Poisson distribution. As such, the single- $G_T^*$ ·PDE\* effect would become the elementary unit underlying the light response, extractable by fluctuation analysis.

Previous heterologous-expression studies have shown that mutating Rho's G-protein-interaction motif from Glu-Arg-Tyr (ERY) to REY severely impaired its binding to  $G_T$  without affecting light absorption (67, 68). Thus, Wendy Yue made such a mouse line (denoted  $Rho^{REY/REY}$ ) and bred it into  $Gcaps^{-/-}$  background. Below,  $Rho^{WT/WT};Gcaps^{-/-}$  and  $Rho^{REY/REY};Gcaps^{-/-}$  lines are referred to as *WT* and *REY*, respectively, when appropriate.

The *REY* retina shows normal morphology (Fig. 2-4a). Moreover, REY-Rho targets correctly to rod outer segments (Fig. 2-4b) and has normal light absorption *in vitro* (Fig. 1c) as well as *in situ* (Fig. 2-4d), with peak absorption at 500 nm. Microspectrophotometry suggested an expression of REY-Rho slightly lower than *WT* (note peak amplitudes in Fig. 1d) but this does not affect data analysis and conclusions. The levels of various rod-phototransduction proteins, including  $G_T\alpha$ , are also normal in *REY* retinæ (Fig. 2-4e).

*REY* rods had similar dark-current amplitudes but slower response kinetics than *WT* (Fig. 2-5a and Table 2-2a). To examine whether the slower kinetics came from the mutant pigment or from secondary changes downstream, we expressed wild-type human red cone pigment transgenically at a low level in *REY* rods (i.e.,  $hOpn1lw^{Tg};Rho^{REY/REY};Gcaps^{-/-}$ ). Previously, we found that transgenic human red cone pigment produced responses with normal Rho-like kinetics in *WT* rods (18), thus serving here as a useful test case. Using 560-nm light that preferentially activates the red cone pigment over REY-Rho, we found

that *hOpn1lw<sup>Tg</sup>;Rho<sup>REY/REY</sup>;Gcaps<sup>-/-</sup>* rods gave small responses with normal kinetics, versus the slowed responses of *REY* rods (Fig. 2-5b and inset). Thus, the *REY* mutation does not affect signal transduction downstream.

More importantly, as a proxy for light sensitivity, the flash intensity ( $\sigma$ ) required for producing a half-maximal response in *WT* and *REY* rods was found to be  $\sim 6$  and  $\sim 46,168$  photons  $\mu\text{m}^{-2}$  at 500 nm, respectively, differing by  $>7,400$ -fold (Fig. 2-5c, see also flash sensitivities in Table 2-2a). Given the normal light absorption by *REY*-Rho, as well as its near-normal expression level and those of other phototransduction components, this drastically lower sensitivity is consistent with *REY*-Rho\*'s exceedingly low efficiency in activating  $G_T$ .

In short, the *REY* mutation greatly reduced the functional coupling between Rho\* and  $G_T$ , potentially providing a tool for estimating the single- $G_T$ \*·PDE\* effect.

## **2. 6 Unitary Response of *REY* Rods Represents Single- $G_T$ \*·PDE\* Effect.**

We carried out fluctuation analysis to extract the elementary unit underlying the light responses of *WT* and *REY* rods, respectively. Rods were subjected to a series of repeated, identical diffuse flashes to elicit an ensemble of small responses (Fig. 2-6a, top) within the linear foot of the respective flash intensity-response relations (Fig. 2-5c). In *WT* rods, each Rho\* produces many  $G_T$ \*·PDE\*s. In *REY* rods, however, *REY*-Rho\*'s exceedingly low signaling efficiency (Fig. 2-5c) means that it triggers mostly nothing, sometimes only a single- $G_T$ \*·PDE\* effect, and almost never more than a single- $G_T$ \*·PDE\* effect, making the single- $G_T$ \*·PDE\* effect the unitary response. For both genotypes, we quantified the response fluctuations by measuring the ensemble mean ( $\mu$ ) and ensemble



variance ( $\sigma^2$ ) of the flash responses (Fig. 2-6a, lower left and right). Whether *WT* or *REY* rods, the response variance and the square of the mean response matched fairly well in waveform for most cells examined, consistent with the stochastic occurrence of fairly constant unitary events. From the Poisson distribution, we obtained the unitary amplitude,  $a$ , from  $a = \sigma^2/\mu$  at the response's initial rising phase (Chapter 6), giving  $3.11 \pm 0.43$  pA for *WT* rods [ $n = 15$  rods; black symbols in Fig. 2-6b, left; cf. Refs. (71, 84)] and  $0.13 \pm 0.04$  pA for *REY* rods ( $n = 12$  rods; gray symbols in Fig. 2-6b, right).

To verify that *REY* rods' unitary responses indeed reflected the effect of just a single  $G_T^* \cdot PDE^*$ , we shortened REY-Rho\*'s lifetime by using a transgenic line (*Grk1<sup>SS61L</sup>*) that has a higher-than-normal expression of rhodopsin kinase, GRK1 (55, 85), thus speeding up the phosphorylation of REY-Rho\* and hence its shutoff. As such, if the normal single-photon (unitary) response involved  $\gg 1$   $G_T^*$ , a shorter REY-Rho\* lifetime might lead to fewer  $G_T^*$ s on average, thus a smaller mutant single-photon response. In contrast, if the *REY* rod's single-photon response involved literally no more than one  $G_T^*$ , a shorter REY-Rho\* lifetime in the *Grk1<sup>SS61L</sup>* genotype should not affect the unitary size but only reduce REY-Rho\*'s probability of producing any  $G_T^*$ , thus lowering sensitivity further (see flash sensitivities in Table 2-2a). Indeed, the *Grk1<sup>SS61L</sup>* background reduced WT-Rho\*'s single-photon response to  $\sim 1.3$  pA [red symbols in Fig. 2-6b, left; cf. Ref. (85)] but left REY-Rho\*'s unitary-response amplitude unchanged (pink symbols in Fig. 3b, right). Conversely, reducing GRK1's level with the *Grk1<sup>+/-</sup>* background (86) increased WT-Rho\*'s single-photon response [green symbols in Fig. 3b, left; cf. Ref. (85)] but again did not affect REY-Rho\*'s unitary response (dark-green symbols in Fig. 3b, right), suggesting that the deficiency in  $G_T$ -activation by REY-Rho is so severe that it cannot be overcome

easily by a longer REY-Rho\*'s lifetime. Note that the GRK mutations did affect the kinetics of the light response from REY-Rho (Fig. 3b, right top; see also Supplementary Fig. 1), confirming an effect on the REY-Rho\* lifetime. In fact, the *Grk1*<sup>S561L</sup> transgene had an obviously bigger impact on the kinetics of small responses in the *REY* background than in *WT* rods (Fig. 3b and Supplementary Table 1a), which may suggest that the inactivation of REY-Rho\* has become the rate-limiting step in photoresponse-termination in these rods.

As an alternative to manipulating REY-Rho\*'s lifetime for validating the single-G<sub>T</sub>\*·PDE effect, we lowered drastically the expression level of G<sub>T</sub> so as to reduce the encounters between Rho\* and G<sub>T</sub>. With the same reasoning as above, we expected this manipulation to reduce the unitary response of *WT* but not *REY* rods. To this end, we generated a mouse line (*Gnat1*<sup>Tg</sup>;*Gnat1*<sup>-/-</sup>;*Rho*<sup>WT/WT</sup>;*Gcaps*<sup>-/-</sup>) with rod G<sub>T</sub>α expressed transgenically under the mouse opsin promoter (Fig. 4a) and the endogenous rod G<sub>T</sub>α gene ablated (87). This genotype brought rod's G<sub>T</sub>α level down to ~6% of *WT* (Fig. 4b), leading to an ~4-fold decrease in light sensitivity (Fig. 4c), but did not affect light absorption by pigment or protein expression of phototransduction components in both *WT* and *REY* backgrounds (Figs. 4d, e).

Under-expression of G<sub>T</sub>α decreased the unitary response amplitude in *WT* rods by 2- to 3-fold (blue symbols in Fig. 3c, left), which is quite a small change given the large decrease in G<sub>T</sub>α protein level (~17-fold). This observation may be explained by a much higher encounter rate between Rho\* and G<sub>T</sub> normally in rods [estimated to be ~17,000 s<sup>-1</sup> for mammalian rods at 37 °C; see Ref. (41)] compared to the rate of G<sub>T</sub>\* production per Rho\* (see Supplementary Text), presumably reflecting the time required for G<sub>T</sub> activation

(i.e., GDP/GTP exchange in  $G_{T\alpha}$  and the subsequent dissociation of  $G_T^*$  from  $Rho^*$ ) during which any further collisions between  $Rho^*$  and other  $G_T$ s would be inconsequential. Thus, although the  $Rho^*$ - $G_T$  encounter rate may be diffusion-limited and roughly proportional to  $G_T$  concentration (41), this rate can be much lower without a large effect on the single-photon-response amplitude. Incidentally, apart from its smaller amplitude, the single-photon response of  $Gnat1^{Tg};Gnat1^{-/-};Rho^{WT/WT};Gcaps^{-/-}$  rods also had a recovery time constant,  $\tau_{rec}$ ,  $\sim 2$  times that in  $WT$  rods (Fig. 2-6c, Table 2-2a; see legends), possibly suggesting that  $G_{T\alpha}$  may shut off more slowly when under-expressed.

More importantly, the unitary-response amplitude remained constant in  $REY$  rods under-expressing  $G_{T\alpha}$  (light blue symbols in Fig. 2-6c, right), further supporting the notion that each  $REY$ - $Rho^*$  activated  $G_T$  with exceedingly low probability, thus producing literally at most one  $G_T^*\cdot PDE^*$ . Taken altogether, we have succeeded in isolating and estimating the response triggered by a single  $G_T^*\cdot PDE^*$ .

## **2. 7 Number of Single- $G_T^*\cdot PDE^*$ Effects Produced Per $WT$ - $Rho^*$ During the Single-Photon Response.**

Compared side by side, the single- $G_T^*\cdot PDE^*$  effect estimated from the  $REY$ - $Rho$  experiments is smaller in amplitude but more prolonged temporally than that from the bleaching experiments (Fig. 2-7a, left). These differences can be explained if, in the repeated-flash experiment, the consequential  $REY$ - $Rho^*$ s (i.e., those successful in eliciting electrical responses) had triggered their respective  $G_T^*\cdot PDE^*$ s not all at the same time instant, but according to a temporal probability density function (see Appendix) after the flash, hence stretching the  $G_T^*$ -effect waveform in time after averaging. Indeed, the time

integrals of the two single- $G_T^* \cdot PDE^*$  effect profiles (i.e., areas under the waveforms) were roughly equal, being  $0.14 \pm 0.03$  pC,  $n = 10$  cells for REY-Rho\* and  $0.12 \pm 0.04$  pC,  $n = 15$  cells for WT-Opn\* after a 5% bleach (Fig. 2-7b). Interestingly, single- $G_T^* \cdot PDE^*$  effects obtained from various other genotypes and bleaching conditions used above produced time-integral values all within a similar range (Fig. 2-7b), although we do not fully understand the slightly varying kinetics in different conditions (e.g. slower decay in the  $G_T\alpha$  under-expressor). One potential factor contributing to the probability density function in REY rods is a long lifetime of REY-Rho\*. However, spectroscopic measurements on heterologously-expressed REY-Rho indicated that at least the post-flash formation and decay of its meta-II state, which activates  $G_T$ , are not any slower than those of WT-Rho (Fig. 2-10). In the *in situ* situation, on the other hand, there could still be a delay in the production of  $G_T^*$  by REY-Rho\*, the phosphorylation of REY-Rho\* and its subsequent binding by arrestin, all of which have been suggested to involve the ERY site or neighboring molecular surfaces (67, 88–91). Dividing the time-integrated profile of the WT single-photon response ( $1.66 \pm 0.52$  pC,  $n = 23$ ; Fig. 2-7b) by that of the single- $G_T^* \cdot PDE^*$  effect (both in *Gcaps*<sup>-/-</sup> background) yields an estimate of 12-14  $G_T^* \cdot PDE^*$  effects per WT-Rho\*. We expect a similar value in the *Gcaps*<sup>+/+</sup> genotype because the GCAP proteins operate downstream of rhodopsin. This calculation assumes that single- $G_T^* \cdot PDE^*$  effects sum linearly during the WT-Rho\* response. There is currently no clear evidence of any significant nonlinearity. Thus, the single-photon response amplitude from a WT-Rho\* appears to decrease roughly in proportion to the number of  $G_T^* \cdot PDE^*$ s produced when Rho\*'s effective lifetime is shortened (85).

It is worth here to go a little further into the physical correlate of the single- $G_T^* \cdot PDE^*$  effect. A generally accepted picture today is that each  $Rho^*$ -produced  $G_T^*$  successfully finds and activates one of the two catalytic subunits ( $PDE\alpha$  or  $PDE\beta$  subunit) on the functionally symmetrical PDE dimeric complex (6, 92) – giving rise to the measured “single- $G_T^* \cdot PDE^*$  effect”, or half of the PDE-dimer activity (93, 94). As such, the total number of effective  $G_T^*$ s produced by one  $Rho^*$  should also be 12-14 as derived above. In this picture, of course, two singly-bound  $G_T^* \cdot PDE^*$ s is functionally no different from one doubly-bound  $G_T^* \cdot PDE^*$ . Alternatively, the PDE-dimer has also been proposed to be functionally asymmetrical. One model posits that the singly-bound  $G_T^* \cdot PDE^*$  dimer has negligible activity, but reaches full dimeric activity when doubly bound by  $G_T^*$  [Refs. (58, 95, 96)]. Another posits the opposite scenario, with the singly-bound  $G_T^* \cdot PDE^*$  dimer already having literally full dimeric activity and the doubly-bound having negligible incremental activity (92). In either of these cases, the “single- $G_T^* \cdot PDE^*$  effect” we measured would correspond to the fully-activated PDE-dimer species. Accordingly, the total number of bound  $G_T^*$ s underlying the activated PDE activity could hypothetically be up to a factor of 2 higher than  $\sim 12-14$ . Because these alternative models are rather tentative, we shall not go further into them here. In any case, regardless of the exact physical entity underlying the “single- $G_T^* \cdot PDE^*$  effect”, our measurements suggest an effective gain of  $\sim 12-14$  at the receptor-to-effector step in phototransduction.

## 2.8 Discussion

Before the present work, the amplification factor at the  $Rho^*$ -to- $G_T^*$  step in rod phototransduction and related parameters have been studied extensively, but not reached

unanimous agreement. Early work (5) has publicized the concept of a high amplification consisting of hundreds of  $G_T^*$  per  $Rho^*$ . Over the years, many other estimates have been suggested, including some much lower numbers more recently (43) (see 2.1), but overall they still range from teens to hundreds of  $G_T^*$ s per  $Rho^*$ . The reasons for such diverse estimates may come variably from non-native preparations, uncertain temperature correction, differences in theoretical assumptions/parameters, or the downright uncertain nature of a monitored signal (2.1). Perhaps because of this continuing disagreement, the original notion of a very high gain has continued to take hold, and remains frequently quoted in textbooks and even generalized to other GPCR pathways (see Introduction). Our measurements reported here based on two independent methods have converged on a unitary single- $G_T^*$ ·PDE\* effect that is only a little over ten-fold smaller than the single-photon response. This estimate is the first derived solely from direct measurements on intact rods and focuses on the effective signaling unit (single- $G_T^*$ ·PDE effect), which is much more relevant than merely the total number of  $G_T^*$ s of unknown consequence produced per  $Rho^*$ . Hopefully we have finally settled the longstanding dispute about the amplification in this step of phototransduction.

Apart from phototransduction, little is known about the amplification at the GPCR\*-to- $G^*$  step in almost all other systems, which are very predominantly activated by ligands. The only ligand-triggered GPCR signaling pathway with related quantitative information available is vertebrate olfactory transduction. Surprisingly, the amplification factor in this case appears to be  $\ll 1$   $G_{\alpha_{olf}^*}$ ·ACIII\* per receptor-ligand binding event in native olfactory receptor neurons (30), where  $G_{\alpha_{olf}^*}$  is the active  $\alpha$ -subunit of  $G_{olf}$  and ACIII\* is an active adenylyl cyclase type III molecule mediating olfactory transduction.

This low gain is due at least in part to a brief dwell time of the odorant ligand on its receptor – perhaps no more than 1 msec or less at least for some receptor-odorant interactions (30) – versus the relatively much longer Rho\* lifetime. Thus, a much lower gain than rod phototransduction may be the norm in olfactory transduction.

The functional significance in this gain difference between phototransduction and olfactory transduction can be rationalized as follows. First, a low affinity between odorant and receptor in olfaction (which most likely explains the short active-receptor lifetime) may be desirable by allowing some odorant receptors to recognize a wide variety of chemicals. Second, the overall amplification in the olfactory signaling circuit is drastically enhanced by a substantial axonal convergence; namely, on average,  $\sim 10^4$  olfactory receptor neurons expressing the same receptor species converge on the same glomerulus in the olfactory bulb (97). In contrast, vision in an extremely dim environment demands not only exquisite sensitivity (down to single-photon detection) but also spatial acuity. The latter function would be greatly degraded by a highly convergent visual neural circuitry. Third, unlike an odorant molecule which upon dissociation can rebind to the same or another receptor, photons disappear instantly whether absorbed or not. Perhaps for these reasons, visual transduction requires a relatively high gain at the single-receptor-molecule level.

It is conceivable that ligand-driven signaling generally has a low GPCR-to-G protein/effector amplification because single-ligand-molecule detection or single-receptor-molecule signaling is not always essential (unless the availability of ligand is exceedingly low). A high gain may even be disadvantageous by causing rapid signal saturation and thus a low dynamic range. Moreover, additional amplification downstream of the G-protein is common, involving effector enzyme activity or ion-channel openings. Finally, overall

sensitivity of the cell can be readily scaled up by increasing the receptor density on the plasma membrane. Thus, there are multiple ways to enhance sensitivity and signal amplification besides the G-protein step. A number of early studies on isolated erythrocyte membranes and vesicle reconstitution systems have suggested that some (98–100), but not other (101) GPCRs could catalyze the activation of multiple G protein molecules per receptor molecule. However, these experiments may not be definitive because of their non-native settings and also ambiguities in what they exactly measured. In any case, it would be very useful to collect more information regarding the amplification question at the G-protein level in other GPCR pathways and see how specific values are correlated with functions. For example, one question is whether the “mere” gain of ~12-14 in phototransduction is already at the high end for GPCR signaling.

Our work here has also provided new biophysical information about the constitutive activity of WT-Opn. Psychophysical experiments demonstrated long ago that the human visual threshold does not increase linearly with the fraction of bleached pigment as would be expected from a simple loss of light-absorbing Rho, but much more steeply (102). The extra-desensitizing effect was eventually found to come from Opn’s constitutive ability to activate the phototransduction pathway, thus behaving as an “equivalent background light” (66). So far, however, nothing is known about the size of the associated electrical events and their frequency underlying this phenomenon. Given Opn\*’s exceedingly weak activity but nonetheless still acting through the same pathway as phototransduction, our speculation is therefore that the underlying unitary signal may be the same as the single-G<sub>T</sub>\*·PDE\* effect. This speculation turns out to be correct. Furthermore, we found the frequency of these events to be on average around one event per day per Opn. Because we can only



detect the successfully triggered unitary electrical events, we do not yet know about the underlying Opn's molecular kinetics. In other words, we do not know how frequently Opn actually transitions into the Opn\* state, how much time it stays in this active state, and the probability that a collision event between Opn\* and  $G_T$  will give a  $G_T^*$ . This probability may or may not be the same as the probability of success for producing  $G_T^*$  by Rho\*.

What is clear for the first time is that, by comparing the spontaneous isomerization rate of rhodopsin to the quantified constitutive activity of Opn (see Results), 11-*cis*-retinal acts as an extremely potent negative agonist of Opn by reducing WT-Opn's effective constitutive activity rate by  $\sim 4.5 \times 10^4$ -fold, apart from endowing photosensitivity to Opn. The remaining question is: does Opn's constitutive activity serve any purpose at all other than introducing noise to vision? The answer is that it probably does, by producing bleaching adaptation, without which vision will not be able to function beyond a very limited range of light intensities. This Opn property is especially crucial for cone vision, which functions in bright light and is therefore invariably associated with the steady presence of Opn. On the negative side, however, Opn will also aggravate retinal diseases that lead to 11-*cis*-retinal deficiency, in that loss of chromophore not only reduces photon capture, but the resulting abundant Opn also generates noise, thus degrading the signal-to-noise ratio further.

## 2. 9 Figures

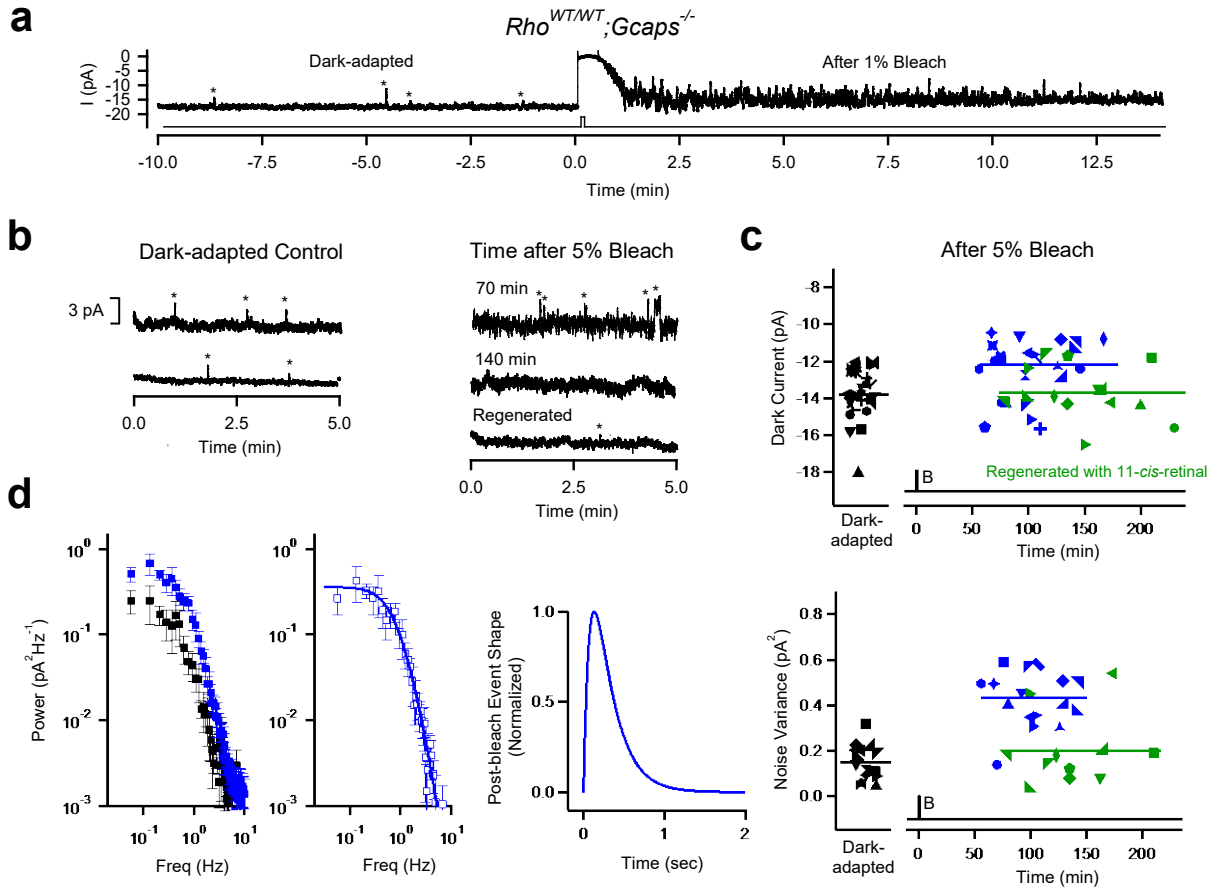


**Figure 2-1. Post-bleach noise from Opn in *Rho*<sup>WT/WT</sup>;*Gcaps*<sup>-/-</sup> rods.** **a**, Noise recording before and after bleaching ~1% of rhodopsin in a *WT* rod. **b**, Left, Recordings from two different rods stored in darkness for >1 hr, showing steady current fluctuations (continuous noise) and occasional discrete events (marked with stars). Right, Recordings from different rods after a 5% bleach and kept in darkness for 70 min, 140 min, or with similar bleach treatment, but subsequently incubated in 11-*cis*-retinal (Chapter 6). **c**, Steady dark current mean (Top) and continuous noise variance (Bottom) after a 5% bleach (blue), and after a 5% bleach followed by 11-*cis*-retinal incubation (green) for comparison with dark control rods (black). Each symbol represents a single cell. Solid lines show the cohort mean for each condition. From pairwise Student's t-tests, we found a significant difference in noise variance between dark control and post-5% bleach rods ( $p < 0.0001$ ) and between post-5% bleach rods and regenerated rods ( $p < 0.0001$ ), but not between dark control rods and regenerated rods ( $p = 0.26$ ). Correspondingly, there was a significant difference in dark current mean between dark control and post-5% bleach rods ( $0.0001 \leq p < 0.05$ ) and between post-5% bleach rods and regenerated rods ( $0.0001 \leq p < 0.05$ ), but not between dark control rods and regenerated rods ( $p = 0.82$ ). **d**, Left, Cohort-averaged continuous-noise power spectra from dark control rods (black) and from post-5% bleach rods (blue). Each frequency point indicates cohort mean  $\pm$  SEM ( $n = 5$  rods). Middle and Right, Difference spectrum and waveform of the unitary Opn\* effect (transient peak normalized to unity) extracted from the difference spectrum by fitting with the spectrum of a convolution of two single-exponential declines (blue curve,  $\tau_1 = 81 \pm 35$  msec,  $\tau_2 = 231 \pm 25$  msec,  $n = 5$  rods).

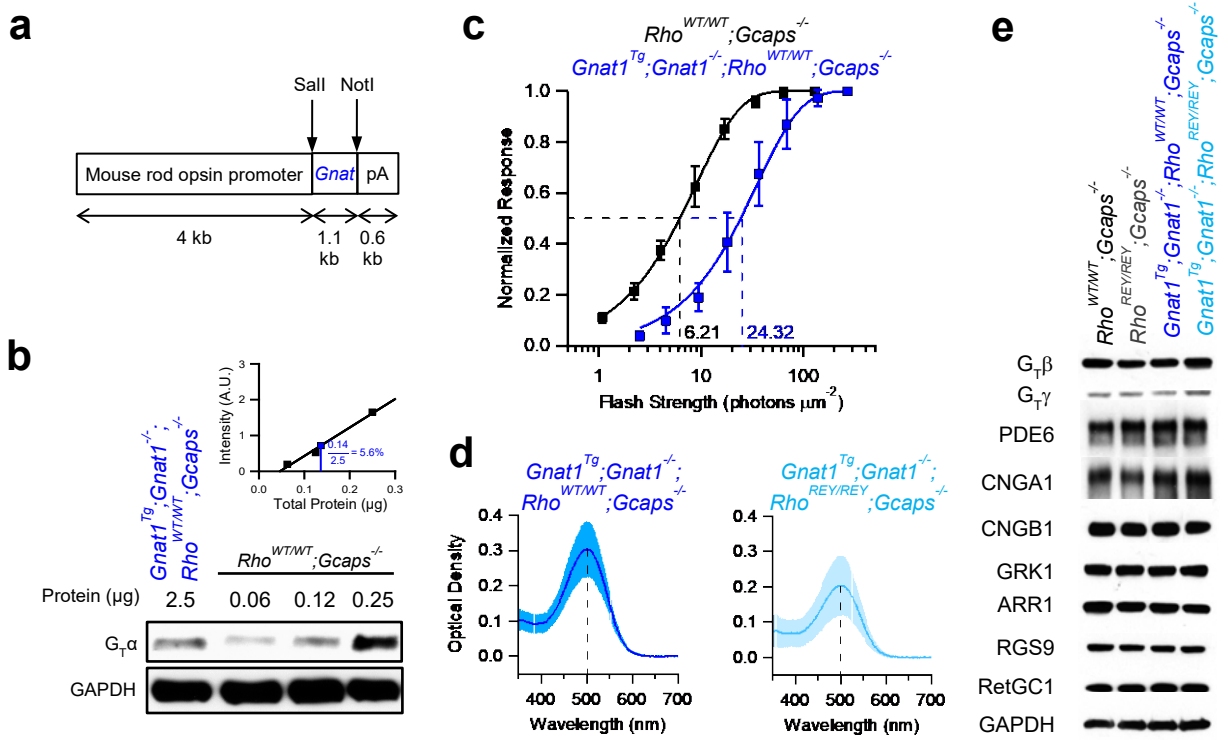


**Figure 2-2. Generation and characterization of *Gnat1<sup>Tg</sup>;Gnat1<sup>-/-</sup>* mice.** **a**, Construct design for the generation of *Gnat1<sup>Tg</sup>* mice. **b**, Absorption spectra of *Gnat1<sup>Tg</sup>;Gnat1<sup>-/-</sup>;Rho<sup>WT/WT</sup>;Gcaps<sup>-/-</sup>* (left) and *Gnat1<sup>Tg</sup>;Gnat1<sup>-/-</sup>;Rho<sup>REY/REY</sup>;Gcaps<sup>-/-</sup>* (right) rods measured by *in situ* microspectrophotometry, showing a normal absorption maximum of rhodopsin (cf. **Figure 2-4d**). Data from R. Frederiksen. **c**, Intensity-response relations of *WT* (black, n = 8) and *Gnat1<sup>Tg</sup>;Gnat1<sup>-/-</sup>;Rho<sup>WT/WT</sup>;Gcaps<sup>-/-</sup>* (blue, n = 12) rods. Fitting with a single saturating-exponential function gave half-saturating flash strengths ( $\rho$ ) of 6.21 and 24.32 (equivalent 500-nm) photons  $\mu\text{m}^{-2}$  for the two genotypes, respectively. Mean  $\pm$  SD (n = 8). Data from W. W. S. Yue. **d**, Western-blot quantification of G $\tau\alpha$  protein in *Gnat1<sup>Tg</sup>;Gnat1<sup>-/-</sup>;Rho<sup>WT/WT</sup>;Gcaps<sup>-/-</sup>* retinæ. Dilution of *WT* protein extracts produced a calibration curve for comparison in band intensities with *Gnat1<sup>Tg</sup>;Gnat1<sup>-/-</sup>;Rho<sup>WT/WT</sup>;Gcaps<sup>-/-</sup>*. G $\tau\alpha$  protein is expressed at ~6% of *WT* in *Gnat1<sup>Tg</sup>;Gnat1<sup>-/-</sup>;Rho<sup>WT/WT</sup>;Gcaps<sup>-/-</sup>* retinæ. Similar results were obtained in several other experiments. **e**, Western blots showing the expression levels of various phototransduction components in retinal extracts from the indicated genotypes. The data for *WT* and *REY* are reproduced here from **Figure 2-4e** for comparison. Data points are mean  $\pm$  SD. Data from X. Ren.

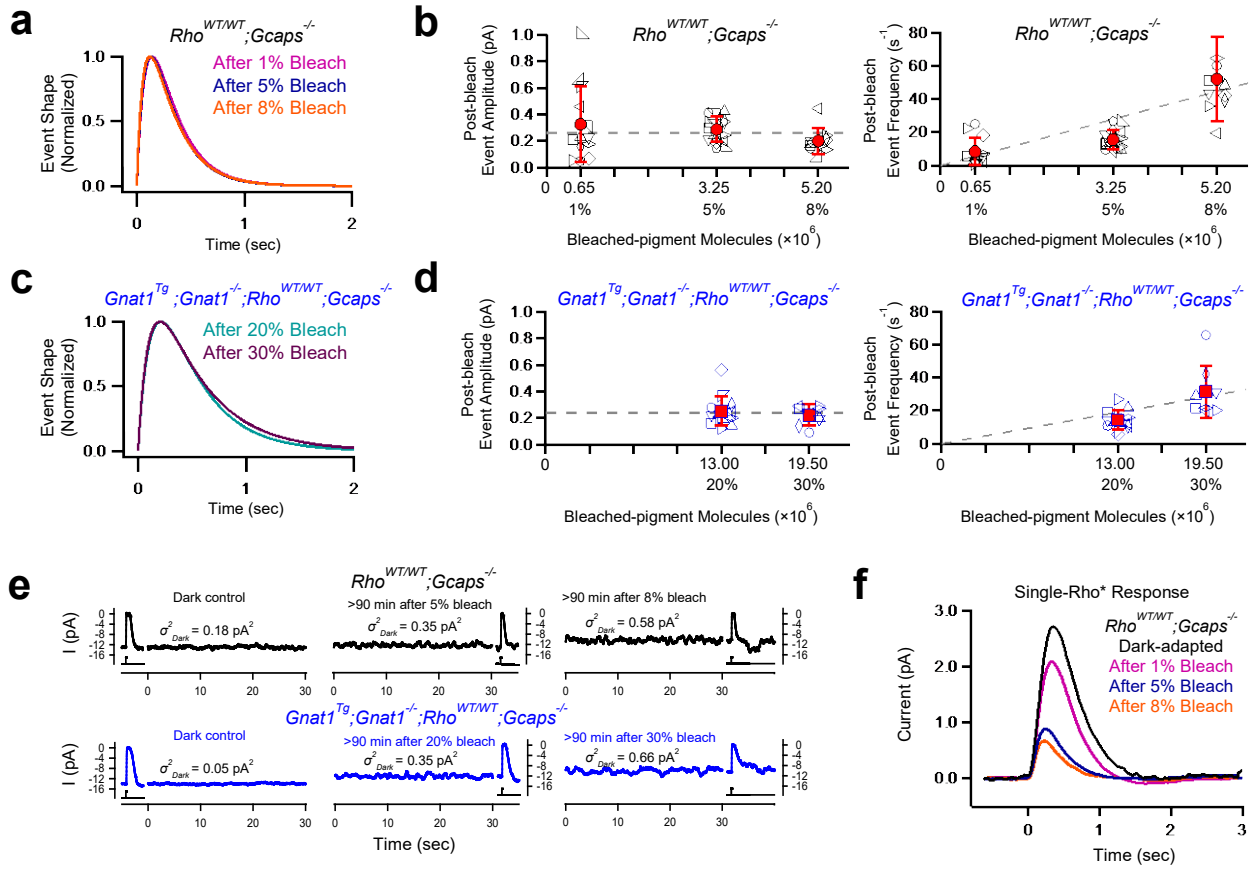


**Figure 2-3. Unitary events underlying constitutive Opn-triggered activity in *Rho<sup>WT/WT</sup>;Gcaps<sup>-/-</sup>* rods.** **a**, Waveform of unitary Opn\* effects after a 1%, 5% or 8% bleach (transient peak normalized to unity) extracted from difference spectra as in **Figure 2-1d** (time-constants in **Table 2-1**). **b**, Left, Unitary amplitudes of Opn-triggered events underlying post-bleach noise after different bleaches of *WT* rods, derived from noise analysis. There was not a significant difference in amplitude across all bleaching conditions ( $p = 0.27$ , one-way ANOVA). Dashed line is the population mean amplitude from all bleach levels (each symbol represents a single cell). Right, Cellular rate of events after different bleaches with percentage of total pigment content indicated below. Dashed line is a linear regression line passing through the origin ( $R^2 = 0.8$ ) with slope giving molecular rate constant of  $8.6 \times 10^{-6}$  events  $\text{sec}^{-1}$  Opn $^{-1}$ . **c**, Waveform of unitary Opn\* effects after a 20% or 30% bleach (transient peak normalized to unity) extracted from difference spectra as in **Figure 2-1d**, but with the *Gnat1<sup>Tg</sup>;Gnat1<sup>-/-</sup>;Rho<sup>WT/WT</sup>;Gcaps<sup>-/-</sup>* line (time-constants in Table S2). **d**, Top, Recordings from dark control (left), 5%- (middle) and 8%-bleached (right) rods from *Rho<sup>WT/WT</sup>;Gcaps<sup>-/-</sup>* mice. Bottom, Similar recordings from dark control (left), 20%- (middle) and 30%-bleached *Gnat1<sup>Tg</sup>;Gnat1<sup>-/-</sup>;Rho<sup>WT/WT</sup>;Gcaps<sup>-/-</sup>* rods with reduced G $\alpha$  expression. Zero-current axes are aligned to illustrate the approximate magnitude of the change in dark current after bleaching. **e**, Same analysis as **b** but with *Gnat1<sup>Tg</sup>;Gnat1<sup>-/-</sup>;Rho<sup>WT/WT</sup>;Gcaps<sup>-/-</sup>* rods after a 20% or 30% bleach. Left, Unitary amplitudes of Opn-triggered events were not significantly different from *WT* rods ( $p = 0.34$ , one-way ANOVA) and the event rate increased approximately in proportion to the amount of Opn formed ( $R^2 = 0.8$ , molecular rate constant =  $1.5 \times 10^{-6}$   $\text{sec}^{-1}$  Opn $^{-1}$ ). **f**, Averaged single-photon responses from WT-Rho\* in dark-adapted *WT* rods as well as after a 1%, 5%, and 8% bleach.

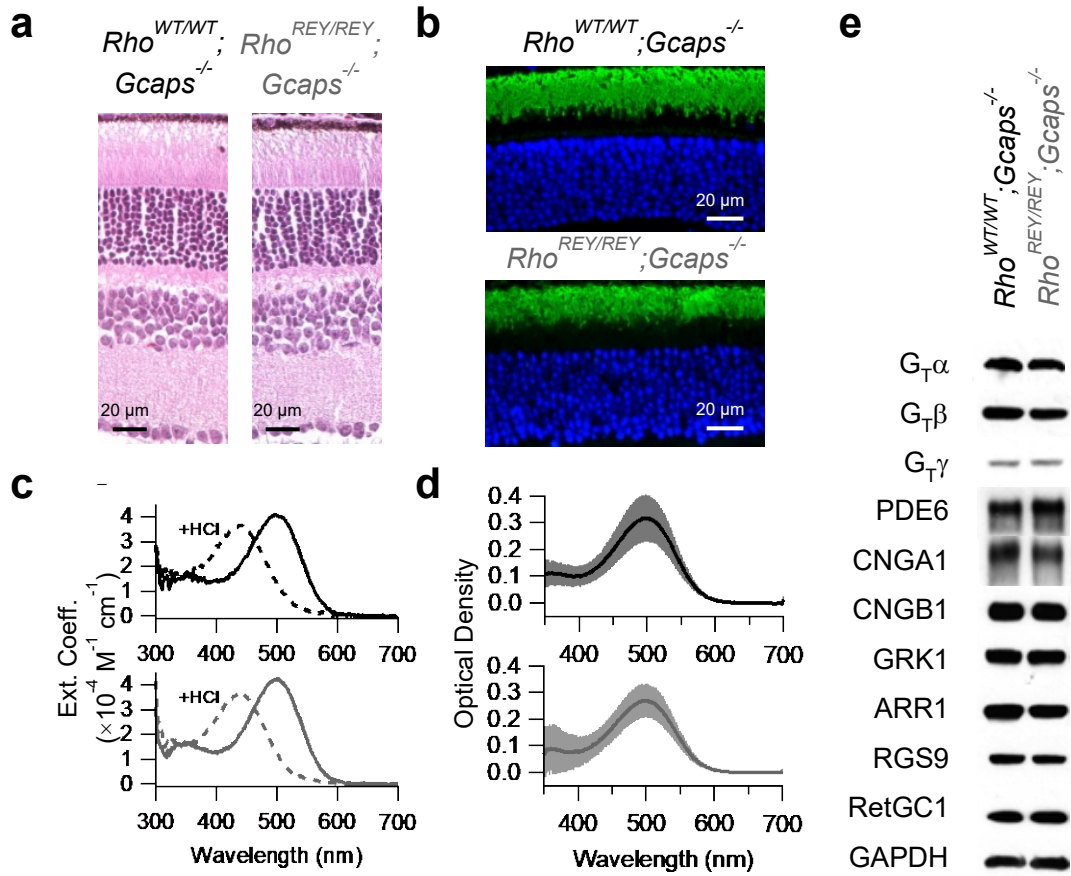




**Figure 2-4. Characterization of *Rho*<sup>REY/REY</sup>;*Gcaps*<sup>-/-</sup> retinae and heterologously expressed REY-Rho.** **a**, Paraffin sections of 2-month-old *WT* (left) and *REY* (right) retinas stained by haematoxylin and eosin. **b**, Paraffin sections of 2-month-old *WT* (top) and *REY* (bottom) retinas immunostained for rhodopsin. DAPI marks the outer nuclear layer. Data from W. W. S. Yue. **c**, Extinction coefficients of WT-Rho (solid black trace) and REY-Rho (solid gray trace) measured by *in vitro* spectrophotometry. Acid denaturation (dashed traces; **Chapter 6**) confirmed that both pigments were present at the same amount. Two other experiments gave similar measurements for REY-Rho. Data from K. Sakai. **d**, Absorption spectra of *WT* (top) and *REY* (bottom) rods measured by *in situ* microspectrophotometry (**Chapter 6**). Mean  $\pm$  SD (n = 8). Data from R. Frederiksen. **e**, Western blots showing the expression levels of various phototransduction components in extracts of *WT* (left) and *REY* (right) retinas. G<sub>T</sub> $\alpha$ , G<sub>T</sub> $\beta$  and G<sub>T</sub> $\gamma$ :  $\alpha$ ,  $\beta$  and  $\gamma$  subunit of G<sub>T</sub>, respectively; PDE6: rod phosphodiesterase isoform 6; CNGA1 and CNGB1: A1 and B1 subunit of the rod cyclic-nucleotide-gated (CNG) channel, respectively; GRK1: G protein receptor kinase isoform 1; ARR1: arrestin isoform 1; RGS9: regulator of G protein signaling isoform 9; RetGC1: retinal guanylate cyclase isoform 1; GAPDH: glyceraldehyde 3-phosphate dehydrogenase (as control for protein concentration in total extracts). Data from X. Ren.

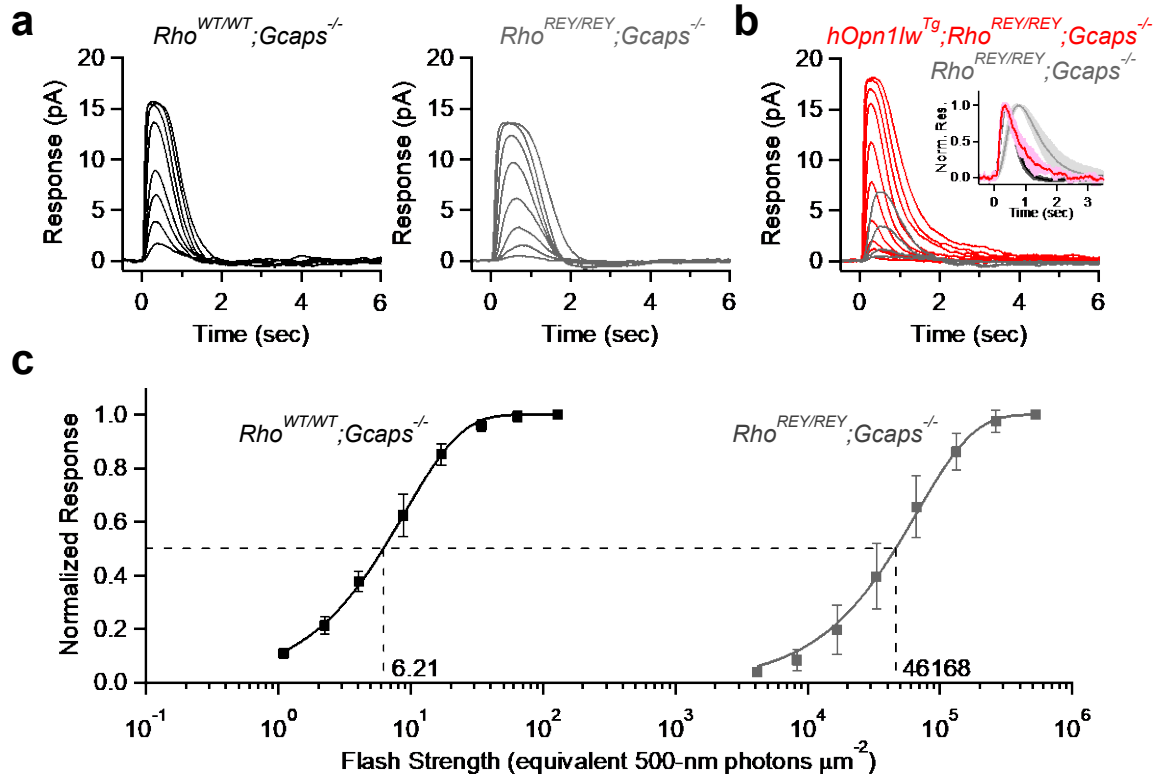


**Figure 2-5. Photoresponses of *REY* rods.** **a**, Response families of a *WT* rod (left) and a *REY* rod (right), both in *Gcaps<sup>-/-</sup>* background. *WT*: 500-nm light; *REY*: white light due to its weak sensitivity. Averaged responses, 10-ms flashes at time zero. **b**, Superimposed responses of a *hOpn1lw<sup>Tg</sup>;Rho<sup>REY/REY</sup>;Gcaps<sup>-/-</sup>* rod (red) and a *REY* rod (gray) to flashes of the same set of intensities at 560 nm ( $\lambda_{\text{max}}$  of transgenic red cone pigment). Averaged responses, 30-ms flashes at time zero. Inset: Small averaged responses (mean  $\pm$  SD) of *hOpn1lw<sup>Tg</sup>;Rho<sup>REY/REY</sup>;Gcaps<sup>-/-</sup>* (red, n = 6), *WT* (black, n = 15) and *REY* (gray, n = 11) rods, overlaid and normalized at peak for kinetics comparisons. Absolute amplitudes are 0.95 pA, 1.93 pA and 1.58 pA, respectively. **c**, Intensity-response relations of *WT* (black, n = 8) and *REY* (gray, n = 16) rods. Fitting with a single saturating-exponential function gave half-saturating flash strengths ( $\rho$ ) of 6.21 and 46,168 (equivalent 500-nm) photons  $\mu\text{m}^{-2}$  for *WT* and *REY* rods, respectively. Data points are mean  $\pm$  SD. Figure from W. S. Yue.

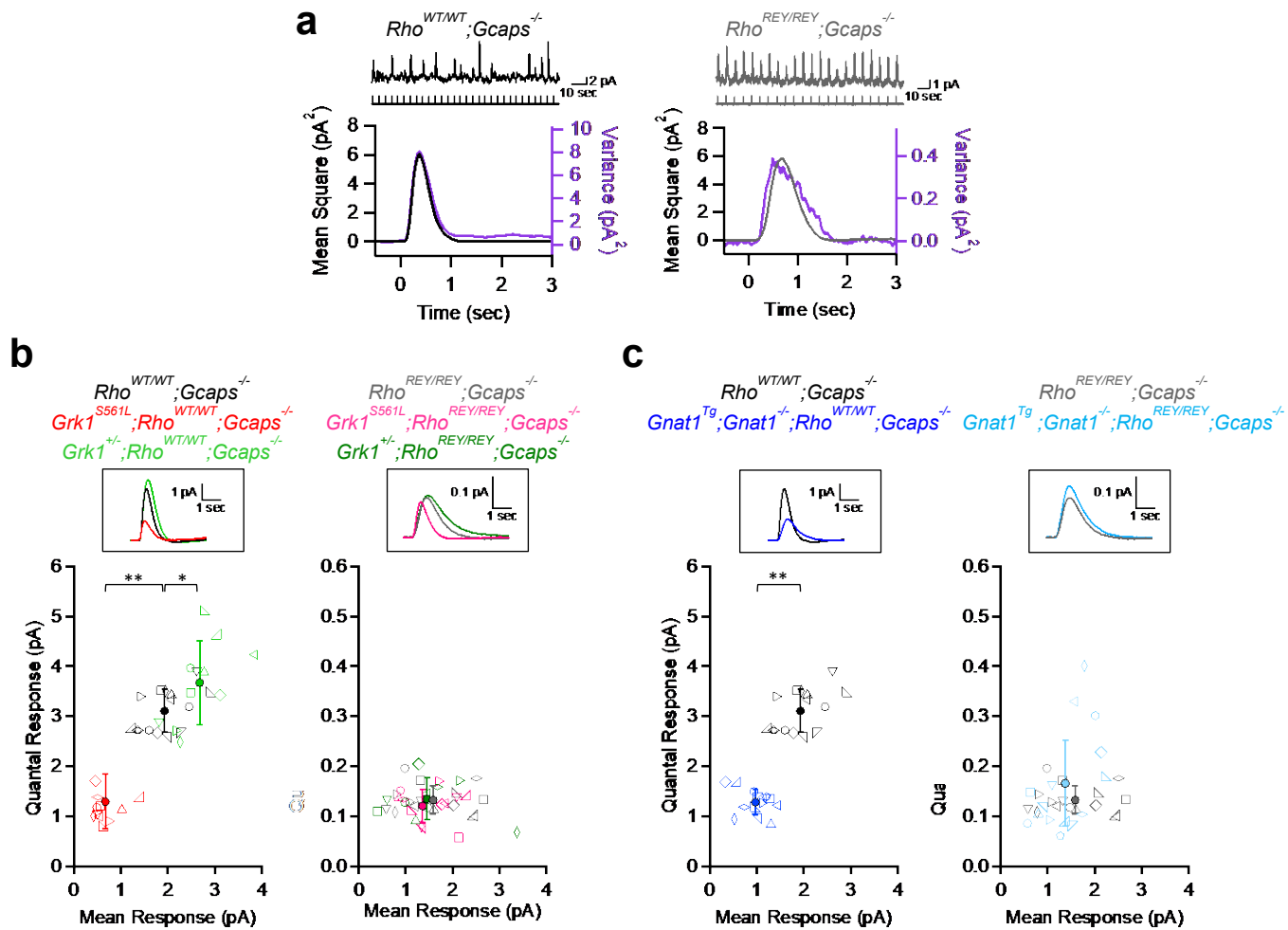


**Figure 2-6. Estimate of single-G<sub>T</sub>\* effect from REY-Rho\* responses.** **a**, Top, Responses of a *WT* rod (left) and a *REY* rod (right) to repetitive 10-ms, 500-nm flashes (vertical bars). For *REY* rods, multiple single-G\* effects were elicited at the chosen intensity, thus the probability of observing failures was low. Bottom, Square of the ensemble mean (black on left; gray on right) overlaid on the ensemble variance (purple) of the responses. Same cells as top. Ratio between ensemble variance and ensemble mean allows estimation of the unitary response amplitude (Methods). **b**, Bottom, Unitary responses of rods with *WT* (left) or *REY* (right) rhodopsin, plotted against the mean response. The *Grk1<sup>S561L</sup>* (red on left; pink on right) and *Grk1<sup>+/-</sup>* (green on left; dark green on right) mutations were used to shorten and lengthen Rho\* lifetime, respectively (see text). Each open symbol represents one cell, with identical symbols representing the same cell being stimulated at multiple intensities. Solid circles are mean  $\pm$  SD. Brackets denote pairwise Student's t-tests on quantal response amplitudes with  $0.0001 \leq p < 0.05$  and  $p < 0.0001$  marked by single and double stars, respectively. No statistically significant differences between genotypes on right ( $p = 0.35$  between *Grk1<sup>S561L</sup>;Rho<sup>REY/REY</sup>;Gcaps<sup>-/-</sup>* and *REY*,  $p = 0.91$  between *Grk1<sup>+/-</sup>;Rho<sup>REY/REY</sup>;Gcaps<sup>-/-</sup>* and *REY*). Top, Averaged single-photon-response profiles of rods of the corresponding genotypes (see Supplementary Table 1 for kinetics measurements). **c**, Similar to **b** but with genetic manipulation on G<sub>T</sub> $\alpha$ . The genotype *Gnat1<sup>Tg</sup>;Gnat1<sup>-/-</sup>* reduces G<sub>T</sub> $\alpha$  expression to  $\sim 6\%$  of *WT* (see **Fig. 2-2**). Difference between genotypes on right is not statistically significant ( $p = 0.20$ ). Figure from W. W. S. Yue.

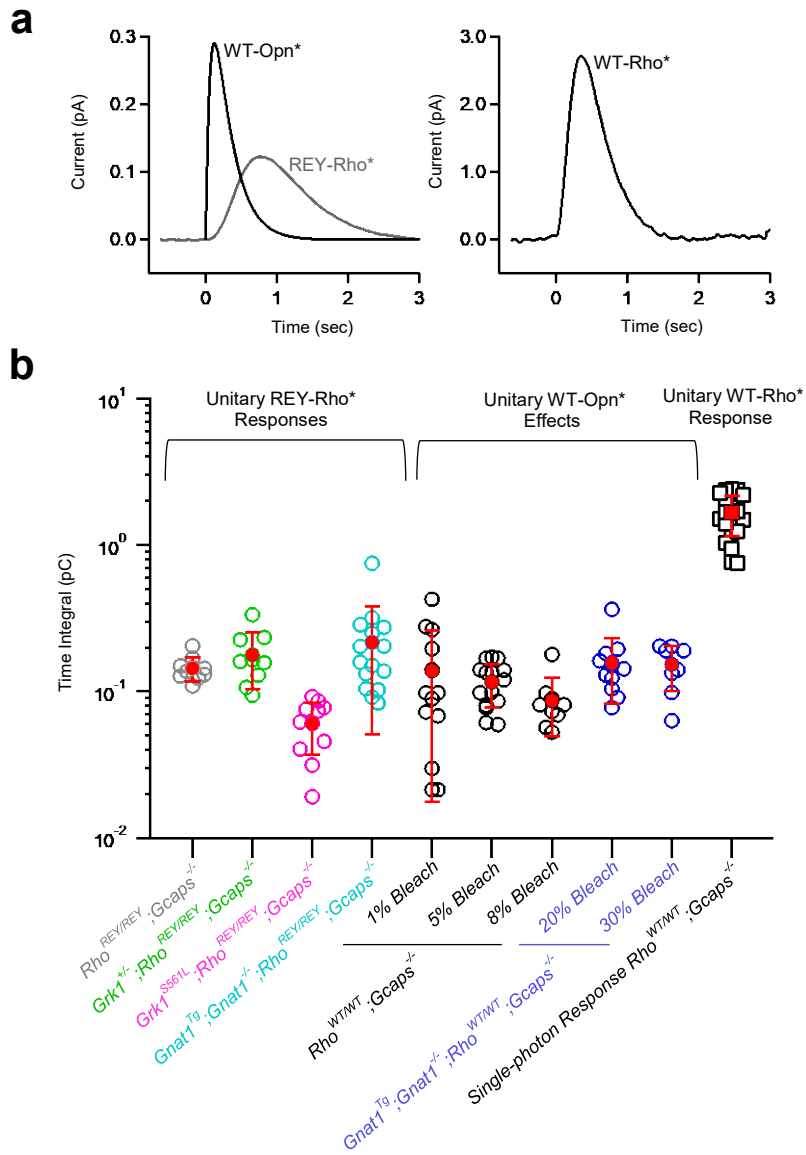


**Figure 2-7. Comparison of individual  $G_T^*$  effects with the unitary WT-Rho\* response.** **a**, Left, Ensemble averages of single- $G_T^*$  effect profiles produced by WT-Opn\* (n = 15) after a 5% bleach and by REY-Rho\* in *REY* rods (n = 10). Right, Ensemble average of the unitary WT-Rho\* response in dark-adapted *WT* rods (n = 23). All measured in the *Gcaps*<sup>-/-</sup> background for facilitating measurements of small responses. **b**, Time-integrated profiles of single- $G_T^*$  effects and the single-WT-Rho\* response. Each open symbol represents a single cell. Closed symbols are mean  $\pm$  SD. The time-integrated single- $G_T^*$  effects from all conditions were all within a range roughly an order of magnitude lower than that of the single-photon response from WT-Rho\*. There was not a significant difference in values when comparing time-integrated profiles of single- $G_T^*$  effects from REY-Rho\* with those from WT-Opn ( $p = 0.21$ , Student's t-test).

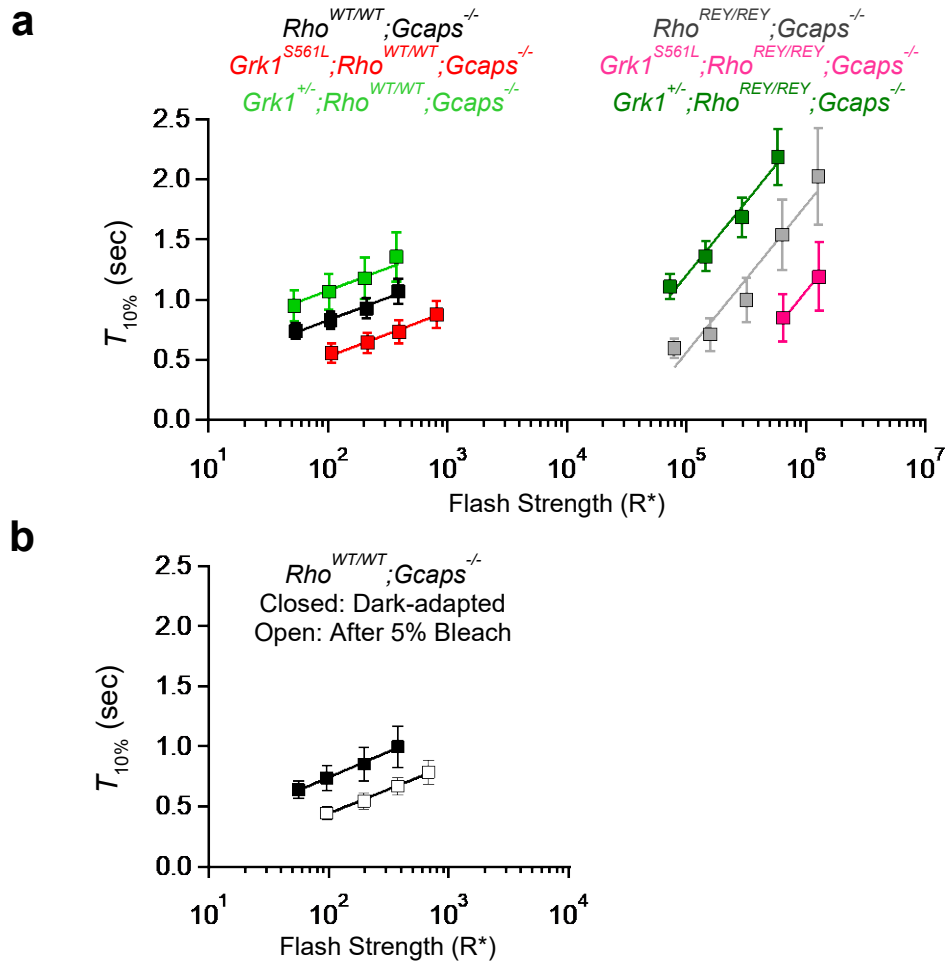


**Figure 2-8. Dominant time constants in various genotypes and cell conditions.** **a**, Plot of time-to-10%-recovery ( $T_{10\%}$ ) against number of  $Rho^*$ 's triggered by flashes (**Chapter 6**) eliciting saturated responses from mouse rods of various genotypes. For  $Rho^{WT/WT}; Gcaps^{-/-}$  (*WT*, black,  $n = 8$ ) and  $Rho^{REY/REY}; Gcaps^{-/-}$  (*REY*, gray,  $n = 18$ ), lines are linear fits to the data without constraints. For other genotypes, linear fits are constrained to have the same slope as that for *WT* or *REY* rods. In all cases, the dominant time constant ( $\tau_D$ ) is given by the slope of the linear fit;  $\tau_D$  is  $163 \pm 16$  ms for rods with *WT*-*Rho* and  $467 \pm 57$  ms with *REY*-*Rho*. Consistent with previous work (103), manipulations on *GRK1*

expression level by  $Grkl^{S561L}$  (WT-Rho: red, n = 12; REY-Rho: pink, n = 8) and  $Grkl^{+/-}$  (WT-Rho: green, n = 11; REY-Rho: dark green, n = 9) genotypes produced vertical downward or upward offsets in  $T_{10\%}$ , apparently reflecting altered Rho\*'s lifetimes. Data from W. W. S. Yue. **b**, Analysis as described in **a** of saturated responses from dark control *WT* rods (black, n = 10) for comparison with rods >60 min after a 5% bleach (white, n = 10);  $\tau_D$  is  $187 \pm 4$  ms providing a fit for both cell states. Similar to  $Grkl^{S561L}$  rods, the vertical downward offset in  $T_{10\%}$  in post-5% bleach rods may reflect a shortening of Rho\*'s active lifetime. Data are mean  $\pm$  SD.



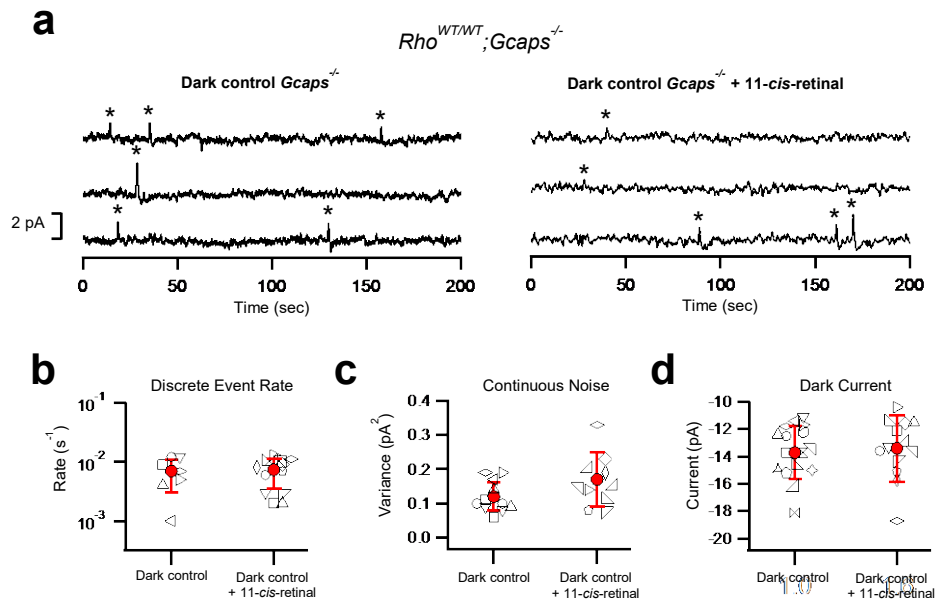


**Figure 2-9. Evaluation of Opn noise in dark-adapted rods.** **a**, Dark noise from a dark control rod versus one after incubation with 11-*cis*-retinal. Recordings were low-pass filtered at 3 Hz to facilitate the identification of discrete events, but the variance analysis of continuous noise was carried out with a 20 Hz low-pass filter. **b**, Cellular rate of discrete events measured by counting individual events. **c**, Continuous noise variance evaluated in 30 sec epochs that did not include discrete events. **d**, Dark current amplitude evaluated from the plateau of the saturated response.

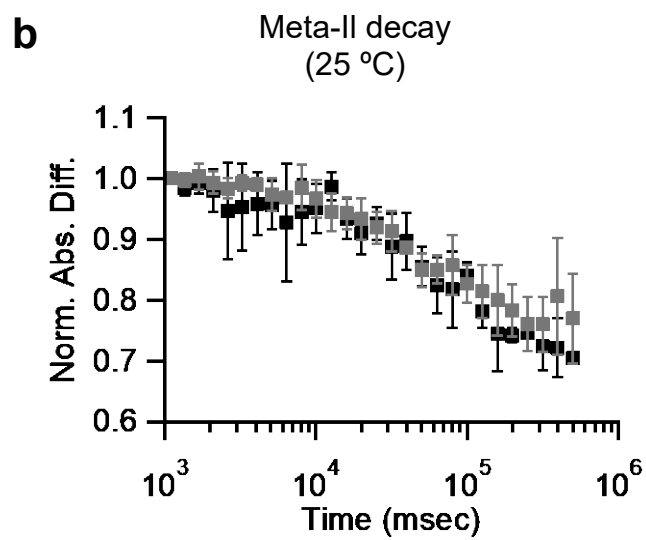
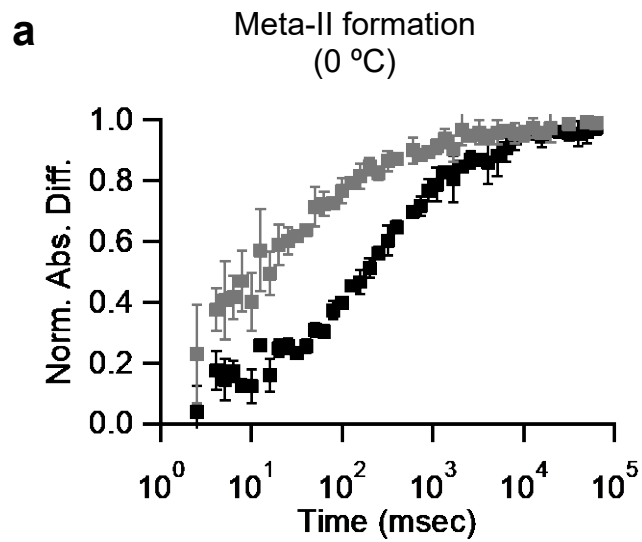


**Figure 2-10. Kinetics of Meta-II formation and decay for WT- and REY-Rho.** **a**, Time course of Meta-II formation for WT- (black) and REY-Rho (gray) at 0 °C. Absorbance at 380 nm (reflecting Meta-II species) was measured by *in vitro* spectrophotometry at different time points after a flash stimulus at time zero (**Chapter 6**). The difference in absorbance between the illuminated and dark-adapted samples was plotted on the y-axis, normalized to the data point at time  $\sim 10^5$  msec. The formation of REY-Meta-II follows a broadly similar transition kinetics as WT-Meta-II, but begins earlier. This difference could not explain the slower kinetics of the light response from REY-rhodopsin. Data points are mean  $\pm$  SD (n = 3 experiments). **b**, Time course of Meta-II decay for WT- (black) and REY-Rho (gray) at 25 °C. Similar procedures as in **a** but with data points normalized to that at time  $\sim 1100$  msec. The decay is very similar for both, regarding both the time of initiation and transition kinetics. Data points are mean  $\pm$  SD (n = 3 experiments). All data from K. Sakai.

**Table 2-1. Parameters from noise analysis of mouse rods of various bleaching levels.**

Genotype	Cell State	$\sigma^2_{Dark}$ (pA <sup>2</sup> )	$I_{Dark}$ (pA)	$\tau_1$ (ms)	$\tau_2$ (ms)	Shape Factor	$a'$ (pA)	$\nu$ (s <sup>-1</sup> cell <sup>-1</sup> )
(1) <i>Rho</i> <sup>WT/WT</sup> ; <i>Gcaps</i> <sup>-/-</sup>	Dark-adapted	0.15 ± 0.07 (n = 18)	13.8 ± 1.31 (n = 28)	-	-	-	-	-
	After 1% Bleach	0.26 ± 0.10 (n = 13)	13.3 ± 1.38 (n = 18)	93 ± 6 (n = 3)	230 ± 1 (n = 3)	1.52 ± 0.01 (n = 3)	0.32 ± 0.28 (n = 13)	8.3 ± 8.1 (n = 13)
	After 5% Bleach	0.43 ± 0.12 (n = 16)	12.2 ± 1.72 (n = 28)	81 ± 35 (n = 5)	231 ± 25 (n = 5)	1.54 ± 0.03 (n = 5)	0.29 ± 0.10 (n = 15)	15.5 ± 5.8 (n = 15)
	After 8% Bleach	0.60 ± 0.22 (n = 10)	10.3 ± 2.40 (n = 10)	82 ± 4 (n = 2)	230 ± 1 (n = 2)	1.54 ± 0.01 (n = 2)	0.20 ± 0.10 (n = 10)	52.0 ± 25.6 (n = 10)
(4) <i>Gnat1</i> <sup>Tg</sup> ; <i>Gnat1</i> <sup>-/-</sup> ; <i>Rho</i> <sup>WT/WT</sup> ; <i>Gcaps</i> <sup>-/-</sup>	Dark-adapted	0.08 ± 0.05 (n = 13)	14.4 ± 1.77 (n = 13)	-	-	-	-	-
	After 20% Bleach	0.41 ± 0.15 (n = 13)	12.4 ± 1.75 (n = 13)	133 ± 56 (n = 6)	363 ± 72 (n = 6)	1.55 ± 0.07 (n = 6)	0.25 ± 0.11 (n = 13)	14.4 ± 5.7 (n = 13)
	After 30% Bleach	0.64 ± 0.20 (n = 8)	10.3 ± 1.59 (n = 8)	108 ± 4 (n = 5)	448 ± 27 (n = 5)	1.58 ± 0.01 (n = 5)	0.22 ± 0.08 (n = 8)	31.4 ± 15.8 (n = 8)

Values are mean ± SD, with the number of cells (n) in parentheses.  $\sigma^2_{Dark}$  is dark noise variance calculated by subtracting Johnson Noise variance (typically 0.01 to 0.03 pA<sup>2</sup>) from the measured continuous noise variance;  $I_{Dark}$  is the saturated response amplitude representing the dark current;  $\tau_1$  and  $\tau_2$  are the time-constants used to best fit the Opn\* effect waveform. *Shape Factor* is dependent on the Opn\*-effect waveform and was calculated as described in Chapter 6;  $a'$  is the post-bleach quantal effect underlying continuous dark noise >1 hr after bleaching (derived from post-bleach noise analysis, Materials and Methods);  $\nu$  is the frequency of unitary events producing the increase in continuous dark noise after bleaching (derived from post-bleach noise analysis, **Chapter 6**).

**Table 2-2a. Parameters of flash responses of mouse rods of various genotypes.**

Genotype	ROS length	$R_{max}$ (pA)	$S_F$ (pA photon <sup>-1</sup> μm <sup>2</sup> )	$a$ (pA)	$t_{int}$ (ms)	$t_{peak}$ (ms)	$t_{rec}$ (ms)
(1) <i>Rho</i> <sup>WT/WT</sup> ; <i>Gcaps</i> <sup>-/-</sup>	17.97 ± 1.23 (n = 29)	15.07 ± 1.98 (n = 15)	1.77 ± 0.45 (n = 15)	3.11 ± 0.43 (n = 15)	567 ± 54 (n = 15)	393 ± 32 (n = 15)	231 ± 51 (n = 15)
(2) <i>Grkl</i> <sup>+/-</sup> ; <i>Rho</i> <sup>WT/WT</sup> ; <i>Gcaps</i> <sup>-/-</sup>	17.41 ± 1.39 (n = 44)	15.95 ± 2.70 (n = 10)	2.17 ± 0.47 (n = 10)	3.68 ± 0.84 (n = 10)	605 ± 109 (n = 10)	480 ± 59 (n = 10)	246 ± 60 (n = 10)
(3) <i>Grkl</i> <sup>S66L</sup> ; <i>Rho</i> <sup>WT/WT</sup> ; <i>Gcaps</i> <sup>-/-</sup>	18.33 ± 2.12 (n = 33)	14.09 ± 2.52 (n = 10)	0.20 ± 0.06 (n = 12)	1.29 ± 0.55 (n = 12)	531 ± 71 (n = 10)	312 ± 27 (n = 10)	216 ± 54 (n = 10)
(4) <i>Gnat1</i> <sup>Tg</sup> ; <i>Gnat1</i> <sup>-/-</sup> ; <i>Rho</i> <sup>WT/WT</sup> ; <i>Gcaps</i> <sup>-/-</sup>	18.50 ± 1.76 (n = 29)	14.75 ± 2.39 (n = 14)	0.23 ± 0.08 (n = 14)	1.28 ± 0.26 (n = 14)	880 ± 191 (n = 14)	557 ± 52 (n = 14)	426 ± 115 (n = 14)
(5) <i>Rho</i> <sup>REY/REY</sup> ; <i>Gcaps</i> <sup>-/-</sup>	18.26 ± 1.29 (n = 37)	14.26 ± 2.39 (n = 11)	(2.95 ± 1.56) × 10 <sup>-4</sup> (n = 15)	0.131 ± 0.039 (n = 12)	1304 ± 330 (n = 11)	787 ± 94 (n = 11)	531 ± 179 (n = 10)
(6) <i>Grkl</i> <sup>+/-</sup> ; <i>Rho</i> <sup>REY/REY</sup> ; <i>Gcaps</i> <sup>-/-</sup>	16.76 ± 1.95 (n = 22)	14.25 ± 3.12 (n = 9)	(2.96 ± 1.74) × 10 <sup>-4</sup> (n = 9)	0.134 ± 0.042 (n = 9)	1516 ± 157 (n = 9)	836 ± 101 (n = 9)	711 ± 158 (n = 9)
(7) <i>Grkl</i> <sup>S66L</sup> ; <i>Rho</i> <sup>REY/REY</sup> ; <i>Gcaps</i> <sup>-/-</sup>	18.56 ± 1.33 (n = 26)	13.91 ± 2.43 (n = 11)	(5.10 ± 2.77) × 10 <sup>-5</sup> (n = 12)	0.120 ± 0.033 (n = 12)	672 ± 99 (n = 11)	452 ± 68 (n = 11)	282 ± 54 (n = 11)
(8) <i>Gnat1</i> <sup>Tg</sup> ; <i>Gnat1</i> <sup>-/-</sup> ; <i>Rho</i> <sup>REY/REY</sup> ; <i>Gcaps</i> <sup>-/-</sup>	18.35 ± 1.98 (n = 34)	13.27 ± 1.90 (n = 15)	(3.09 ± 1.13) × 10 <sup>-5</sup> (n = 15)	0.166 ± 0.086 (n = 15)	1340 ± 402 (n = 15)	752 ± 130 (n = 15)	533 ± 182 (n = 15)

**Table 2-2b. Parameters of flash responses of mouse rods after various bleaching levels.**

Genotype	Cell State	$R_{max}$ (pA)	$S_F$ (pA photon <sup>-1</sup> μm <sup>2</sup> )	$a$ (pA)	$t_{int}$ (ms)	$t_{peak}$ (ms)	$t_{rec}$ (ms)
(1) <i>Rho</i> <sup>WT/WT</sup> ; <i>Gcaps</i> <sup>-/-</sup>	Dark-adapted	14.83 ± 1.61 (n = 10)	1.19 ± 0.30 (n = 10)	2.78 ± 0.54 (n = 10)	613 ± 118 (n = 10)	(n 365 ± 69 (n = 10)	233 ± 36 (n = 10)
	After 1% Bleach	13.52 ± 1.90 (n = 8)	0.80 ± 0.15 (n = 8)	2.11 ± 0.47 (n = 8)	559 ± 61 (n = 8)	322 ± 31 (n = 8)	220 ± 71 (n = 8)
	After 5% Bleach	12.91 ± 1.83 (n = 5)	0.43 ± 0.23 (n = 5)	0.90 ± 0.34 (n = 5)	482 ± 67 (n = 5)	240 ± 29 (n = 5)	222 ± 17 (n = 5)
	After 8% Bleach	9.89 ± 1.34 (n = 5)	0.23 ± 0.01 (n = 5)	0.73 ± 0.26 (n = 5)	438 ± 43 (n = 5)	210 ± 9 (n = 5)	218 ± 95 (n = 5)

Values are mean ± SD, with the number of cells analyzed (n) in parentheses. ROS length is the length of live rod outer segments measured with light microscopy. Flash responses were obtained with 500-nm or white light, with white-light intensity converted to equivalent 500-nm intensity (**Chapter 6**).  $R_{max}$  is the maximum response amplitude representing the dark current;  $S_F$  is the flash sensitivity;  $a$  is the quantal response amplitude;  $t_{int}$  and  $t_{peak}$  are the integration time and time-to-peak of small responses, respectively;  $t_{rec}$  is the recovery time constant obtained from exponential fits to the final decay of small responses (**Chapter 6**). Table 2-1b from W.W.S. Yue.

## Chapter 3. Dark noise and visual impairment from a rhodopsin mutant

### 3.1 Past work on pigment noise theory

Psychophysical experiments on dark-adapted human subjects first demonstrated that our visual system has an extremely low threshold for perceiving light, requiring the absorption of perhaps only ~5 to 8 photons spread over an area of ~500 rods in the retina (10), suggesting that each rod could signal the absorption of a single photon. Suction-pipette recordings (Chapter 6) have shown that individual rods are indeed capable of signaling the absorption of a single photon (59), and that dark isomerization of rhodopsin, driven by thermal energy, produces noise that the nervous system confuses with real light (11, 15). The issue of overcoming dark noise is perhaps even more burdensome in red-sensitive cones where the human red cone pigment is ~500-fold noisier than rhodopsin (18). Recent work led to the development of a quantitative relation between the thermal isomerization rate of a visual pigment as a function of i) its peak-absorption wavelength ( $\lambda_{max}$ ) and ii) the accessibility of its chromophore-binding pocket (1, 104). Briefly, the activation-energy barrier for isomerization of a pigment ( $E_a$ ) is inversely proportional to  $\lambda_{max}$ , such that  $E_a = 0.84 \times h \times c / \lambda_{max}$  where  $h$  is Planck's constant,  $c$  is the speed of light, and 0.84 is a fundamental constant (1) derived from suction-pipette recording experiments (discussed below, 3.6). The rate constant for thermal isomerization can then be predicted using a probability distribution from statistical mechanics (105) for complex molecules with  $m = 45$  vibrational modes:

$$f_{\geq E_a} = e^{\frac{-E_a}{RT}} \sum_1^m \frac{1}{(m-1)!} \left(\frac{E_a}{RT}\right)^{m-1}$$

giving the probability ( $f_{\geq E_a}$ ) that a pigment will absorb enough thermal energy to overcome its energy barrier for isomerization, where  $R$  is the universal gas constant and  $T$  is absolute temperature. Finally, the predicted isomerization rate constant is  $k = A \times f_{\geq E_a}$  where  $A$  represents the approximate frequency of trials to overcome the energy barrier (known as the pre-exponential factor). Measurements from various rod and cone pigments showed empirically that  $A$  is apparently ~26-fold higher for cone pigments as compared to rod pigments (1). The higher pre-exponential factor of cone pigments is proposed to be associated with a more accessible chromophore-binding pocket, which might allow more frequent attempts to overcome the isomerization-energy barrier (104). While these predictions have so far matched well with experimental measurements with wild type pigments, the theory has not yet been applied to study supposedly “noisy” mutant pigments.

### 3.2 Introduction

Rhodopsin (WT-Rho) is among the most abundant proteins in the retina and is largely responsible for our high visual sensitivity under dim light (discussed above). This extreme sensitivity depends not only on relatively high signal amplification (Chapter 2) and a large quantity of Rho packed into each cell, but also on Rho’s incredible stability, although, false activation events in darkness occur in macaque rods on average once every ~2.7 minutes (106), and similarly in mouse rods (1, 18, 80) these events occur on average once every ~1.4 minutes. Taking the WT-Rho content to be  $6.5 \times 10^7$  molecules per mouse rod (1), it takes on average ~160 years for a single WT-Rho to isomerize in darkness at 37°C. After studying several rod and cone pigments (1, 104), we still do not know whether this thermal noise plays a role in visual impairment associated with Rho mutants and how

pigment noise theory (3.1) might help to understand any excess signaling from such mutants.

Many Rho mutants have been implicated in disorders of vision involving rod dysfunction and/or retinal degeneration (12), but the exact role of these mutants in visual impairment is unclear. While diminished visual sensitivity is a common symptom in humans with Rho mutations, it is not known if certain mutants actually produce excessive dark noise from, for example, a higher rate of thermal isomerizations, or instead if the loss of sensitivity arises simply from a loss of Rho content in the outer segment. Additionally, it is unclear if retinal degeneration results from any excess signaling to transducin (107). Animal models expressing Rho mutants have not been able to nail down answers to these questions (108). The crux of the problem is that it has not been easy to isolate light responses and dark noise mediated by Rho mutants due to the high expression of endogenous WT-Rho. Any mutant-Rho responses or thermal isomerizations would be difficult to distinguish from the dominant endogenous population. Endogenous WT-Rho cannot easily be removed because *Rho*<sup>-/-</sup> mice produce only short outer segments that disappear by adulthood [WT-Rho constitutes a major structural support for maintaining the outer segment (109)]. Here we have taken a different approach to remove Rho signaling by utilizing a mouse line where the endogenous Rho has been largely silenced by a targeted mutation of the G-protein binding site (*Rho*<sup>REY/REY</sup>; Chapter 2). This mouse line preserves outer segment structure and does not show any sizeable light responses to flashes up to ~4,000 photons- $\mu\text{m}^{-2}$ . For the first time, we could unambiguously study light responses and dark noise from a particular disease-causing mutant (D190N-Rho expressed in *Rho*<sup>D190N/REY</sup>



rods) to directly measure its thermal isomerization rate and perhaps to pinpoint its role in visual impairment.

Of the >100 Rho mutants identified in patients with stationary night blindness or retinitis pigmentosa, relatively few have been studied in animal models (108, 110–112), in part for the obstacles discussed above. Heterologous expression of Rho mutants in cell culture allowed for screening many of these mutants to evaluate their ability to fold properly and to measure their absorption spectra (2, 3, 113). Despite the fact that D190N-Rho was found to have a possible misfolding problem (113), this mutant was later reexamined in light of the first crystallographic WT-Rho structures that showed D190 and R177 form an ionic bond sitting directly above the chromophore-binding pocket and both residues are highly conserved in rod and cone pigments (13). Given, that D190N-Rho was a known human mutation implicated in retinal disease, biochemical studies were conducted to study its thermal stability in vitro (13, 14, 114). D190N-Rho appeared to decay from its dark state faster than WT-Rho in biochemical assays (done at 55°C to facilitate measurements). This led to speculation that D190N-Rho has a higher rate of thermal isomerization (14, 115), thus the mutant would produce excess dark noise in rods leading to lower visual sensitivity in *Rho*<sup>D190N/WT</sup> patients (115). Later a *Rho*<sup>D190N/WT</sup> mouse was generated to look further into the causes of visual impairment (108). In both *Rho*<sup>D190N/WT</sup> humans and mice, the electroretinogram (ERG) a-wave has a diminished maximal amplitude (108), which was suggested to confirm desensitization due to elevated dark noise mediated by D190N-Rho. Unfortunately, the observed effects could also be explained by shortened outer segments and thus smaller dark current amplitudes on average across all rods examined as a population in the ERG a-wave. We decided to more carefully examine

dark noise from D190N-Rho in mouse rods to better understand its role in visual impairment.

### 3.3 Measuring mutant-Rho activity in mouse rods

To silence endogenous Rho, we made use of a mouse line with a mutated G-protein-binding site (REY-Rho, Chapter 2), substantially lowering the probability of triggering a response after photon absorption. To facilitate measurements of single-photon responses and dark isomerization events, we used a genetic background that boosts single-Rho responses by ~5-fold by removing a negative feedback in the downstream cascade [(Guanylate cyclase activating protein 1 and 2 knockout, *Gcaps*<sup>-/-</sup>) (71)]. For example, in wild type rods (*Rho*<sup>WT/WT</sup>;*Gcaps*<sup>-/-</sup>), flashes of ~14 photons per square micron evoked responses in nearly every trial, while in *Rho*<sup>REY/REY</sup>;*Gcaps*<sup>-/-</sup> rods, the same flash strength did not produce any noticeable responses (Fig. 3-1a). When one copy of the WT-Rho allele is expressed together with REY-Rho (*Rho*<sup>WT/REY</sup>;*Gcaps*<sup>-/-</sup>), WT-Rho responses were observed frequently to the same flash strength as above with a measurable probability of failure used to calculate the approximate WT-Rho content in *Rho*<sup>WT/REY</sup> rods (see 3.4). Likewise, in *Rho*<sup>D190N/REY</sup> rods, distinct D190N-Rho responses were observed, but with a relatively high probability of failure ( $p_f = 0.65 \pm 0.10$ ,  $n = 12$  rods) allowing for direct estimation of the effective D190N-Rho content in the outer segment. Being able to measure D190N-Rho responses also allowed us to unequivocally evaluate the unitary D190N-Rho\* response, which we found to be very similar to WT-Rho\* in amplitude and kinetics (Fig 3-1b). Notably, unitary responses were evaluated within the linear foot of their respective intensity-response relations (mean response < 20% of the saturated

response), which differed because  $Rho^{D190N/REY};Gcaps^{-/-}$  were 3.8-fold less sensitive than  $Rho^{WT/REY};Gcaps^{-/-}$  (Table 3-1). We sought to figure out if this difference in sensitivity was due to any steady background noise contributed by thermal isomerization of D190N-Rho or simply due to a loss of photon capture from fewer D190N-Rho molecules reaching the outer segment.

### 3.4 Estimating mutant-Rho content from the probability of failure

Following the Poisson distribution, the probability of failure (i.e. of a photon passing through the outer segment without being absorbed by Rho) is given by  $p_f = \exp(-A_C \times I_F)$ , where  $A_C$  is the effective collecting area of an outer segment (in photoisomerizations photons<sup>-1</sup> μm<sup>2</sup>) and  $I_F$  is flash strength (in photons μm<sup>-2</sup>). The effective collecting area ( $A_C$ ) is a function of Rho content in the outer segment and Rho's light-absorption characteristics,  $A_C = V \times \delta \times \alpha_\lambda \times f \times Q$ , where  $V$  is the outer segment's volume,  $\delta$  is the unknown Rho concentration (known to be  $\sim 2.11 \times 10^6$  Rho molecules μm<sup>-3</sup> in  $Rho^{WT/WT}$  rods),  $\alpha_\lambda$  is the molecular extinction coefficient of Rho (116) oriented in an outer segment disk membrane ( $\sim 1.76 \times 10^8$  μm<sup>2</sup> for 500 nm light),  $Q$  is the probability that an absorbed photon leads to isomerization [0.67, (116)], and  $f$  is a polarization factor due to the orientation of rhodopsin approximately perpendicular to the outer segment long axis [0.5 for transverse illumination with unpolarized light, (59)]. Given that the effective gain downstream of Rho\* is  $\sim 12-14$  G<sub>T</sub>\*-PDE\* on average (Chapter 2), we suspect that nearly all photoisomerizations will produce a measurable electrical response. Thus, the probability of failure ( $p_f$ ) can be used to estimate the number of effective Rho molecules ( $V \times \delta$ ) in a rod.

Estimating Rho content from the measured probability of failure in *Rho*<sup>D190N/REY</sup>;*Gcaps*<sup>-/-</sup> and *Rho*<sup>WT/REY</sup>;*Gcaps*<sup>-/-</sup> rods (Fig 3-1c), the number of effective D190N-Rho in the outer segment is ~2-fold lower than that of WT-Rho in *Rho*<sup>WT/REY</sup> rods. We are in the process of quantifying D190N-Rho mRNA by comparing *Rho*<sup>D190N/REY</sup> with *Rho*<sup>WT/REY</sup> and *Rho*<sup>REY/REY</sup> retinæ using qRT-PCR. The decrease in sensitivity of *Rho*<sup>D190N/REY</sup>;*Gcaps*<sup>-/-</sup> rods appeared to be slightly lower than would be predicted from the reduced number of effective Rho molecules (D190N-Rho). However, it was still uncertain if the thermal isomerization rate of D190N-Rho was any higher than WT-Rho in situ.

### 3.5 Dark noise and the thermal isomerization rate of mutant Rho in mouse rods

Endogenous Rho also poses a challenge for measuring thermal isomerization events from any mutant Rho species expressed in mouse rods, particularly for D190N-Rho, which produces unitary responses indistinguishable from WT-Rho\* (see above). While each WT-Rho is extremely stable (see introduction), the total endogenous population ( $6.5 \times 10^7$  WT-Rho per *Rho*<sup>WT/WT</sup>;*Gcaps*<sup>-/-</sup> rod) gives rise to one thermal isomerization every ~80 sec at 37°C [Fig. 3-2a, left and (1, 80)]. We demonstrated the uncertainty created by endogenous Rho with dark noise recorded from *Rho*<sup>D190N/WT</sup>;*Gcaps*<sup>-/-</sup> rods (data not shown). Without knowing the effective Rho content from each Rho allele in these rods, it was impossible to tell which events were coming from WT-Rho and which were coming from D190N-Rho. To circumvent this issue, dark noise from endogenous Rho was silenced in *Rho*<sup>REY/REY</sup>;*Gcaps*<sup>-/-</sup> rods (Fig. 3-2a, right). It was then possible to count D190N-Rho-mediated isomerization events with *Rho*<sup>D190N/REY</sup>;*Gcaps*<sup>-/-</sup> rods (Fig. 3-2b, right). The total cellular event rate in this genotype was  $0.007 \pm 0.003$  D190N-Rho isomerizations sec<sup>-1</sup> (n

= 12 rods), which is somewhat higher (data still being collected) than the cellular rate of WT-Rho events from one allele of endogenous Rho (in *Rho*<sup>WT/REY</sup>; *Gcaps*<sup>-/-</sup> rods, Fig 3-2b, left). After taking into consideration the effective Rho content in each genotype (see above), we found that a molecule of D190N-Rho isomerizes ~4.5-fold more frequently than WT-Rho at 37°C in mouse rods. This is a somewhat intriguing finding in that D190N-Rho's  $\lambda_{max}$  is identical to WT-Rho (14), and according to pigment noise theory (3.1), would suggest that either the isomerization-energy barrier of D190N-Rho shifted without affecting  $\lambda_{max}$  or perhaps that the chromophore-binding pocket has become more open to the external environment allowing for more frequent molecular attempts to overcome the energy barrier (3.1).

### 3.6 Activation-energy barrier for isomerization

According to the recently-developed pigment noise theory (3.1), the activation-energy barrier for isomerization is given by:  $E_a = hc / \lambda_c$  where the critical wavelength ( $\lambda_c$ ) marks the lower limit for thermal enhancement of photosensitivity,  $h$  is Planck's constant, and  $c$  is the speed of light (1). From rods and cones of various species,  $\lambda_c / \lambda_{max}$  was found previously to be a fundamental constant equal to  $\sim 0.84 \pm 0.01$  [ $n = 7$  pigments, (1)] for wild-type pigments, but no mutant pigments have yet been evaluated. We indeed found this parameter to be 0.829 for WT-Rho in *Rho*<sup>WT/WT</sup> rods, and to be unchanged for D190N-Rho ( $\lambda_c / \lambda_{max} = 0.833$ ) in *Rho*<sup>D190N/REY</sup> rods with  $E_a$  calculated to be 47.4 kcal mol<sup>-1</sup> for WT-Rho and 47.7 kcal mol<sup>-1</sup> for D190N-Rho. In other words, the higher thermal isomerization rate observed for a D190N-Rho molecule could not be explained by any change in the activation-energy barrier.

### 3.7 Accessibility of the chromophore-binding pocket

Another major factor affecting the thermal noise of visual pigments is the accessibility or “openness” of the chromophore-binding pocket (104). We shall assess the openness of the chromophore-binding pocket by measuring the rate of chromophore exchange in situ when replacing endogenous 11-*cis*-retinal with 9-*cis*-retinal, observed with microspectrophotometry as a gradual blueshift in  $\lambda_{max}$  from 500 nm to ~480 nm. The rate of chromophore exchange in wild type rhodopsin is extremely slow (not detectable within 6 hours) due to a well-protected chromophore-binding pocket, whereas exchange occurs within 3 hours in wild type cone pigments (104). We are currently evaluating the rate of chromophore exchange of D190N-Rho in collaboration with Rikard Frederiksen, UCLA. The prediction from pigment noise theory (3.1) is that the chromophore-binding pocket may be more open and accessible in D190N-Rho allowing more attempts of the chromophore to overcome the isomerization energy barrier, thus contributing to a higher rate of thermal isomerization.

### 3.8 Degeneration caused by D190N-Rho and its relationship to transducin signaling

Even with D190N-Rho’s ~4.5-fold higher molecular rate constant for thermal isomerization, the measured cellular rate of thermal isomerization events was actually unchanged in  $Rho^{D190N/WT};Gcaps^{-/-}$  (data not shown) and lower in  $Rho^{D190N/REY};Gcaps^{-/-}$  (Fig. 3-2b, right) comparing each to  $Rho^{WT/WT};Gcaps^{-/-}$  rods, presumably because of a low D190N-Rho content in both genotypes (Fig. 3-1 and Table 3-2). Yet  $Rho^{D190N/D190N}$  retinae show clear signs of degeneration (photoreceptor cell death observed as a loss of nuclei in

the outer nuclear layer) at eye opening (P12), which is more rapid than the degeneration seen in *Rho*<sup>-/-</sup> mice with healthy outer-nuclear-layer cell bodies until at least P30 (109). The degeneration also occurs in *Rho*<sup>D190N/WT</sup> retinæ, albeit at a slower rate (not obvious at P18, but becoming clear by P100). These observations suggest that lower D190N-Rho content in the outer segment is not the sole cause for retinal degeneration.

Despite our lack of finding any higher dark noise in the outer segment of *Rho*<sup>D190N/WT</sup> rods, we investigated the possibility that D190N-Rho signaling to G<sub>T</sub> was involved in degeneration [as speculated previously by others, (14, 108)]. Light-induced rod cell death, in certain cases, has been rescued by abolishing G<sub>T</sub>α (in *Gnat1*<sup>-/-</sup> mice). For example, when WT-Rho signaling is prolonged by deletion of rod arrestin (*Arr1*<sup>-/-</sup>), extended bright light exposure (e.g. 5,000 lux for 12 to 36 hrs) causes rapid rod cell death that is rescued in *Arr1*<sup>-/-</sup>;*Gnat1*<sup>-/-</sup> animals (107, 117) suggesting that persistent signaling from WT-Rho to G<sub>T</sub> contributes to degeneration. Contrastingly, we found that retinal degeneration in *Rho*<sup>D190N/D190N</sup>;*Gnat1*<sup>-/-</sup> animals was just as severe as in *Rho*<sup>D190N/D190N</sup>;*Gnat*<sup>+/+</sup> at age P15 (Fig. 3-4a,b). In *Rho*<sup>D190N/WT</sup>;*Gnat1*<sup>+/+</sup> and *Rho*<sup>D190N/WT</sup>;*Gnat1*<sup>-/-</sup> retinal degeneration was slower, with healthy morphology up to at least P18 (Fig. 3-4c). As one might have expected from the modest change in thermal isomerization of D190N-Rho, it appears that persistent signaling to G<sub>T</sub> is not a major cause for degeneration in these animals.

We next considered the possibility that some misfolded D190N-Rho leads to cell death through stress on the endoplasmic reticulum (107, 118, 119). In an initial screen of Rho mutants from patients with retinitis pigmentosa (113), human D190N-Rho expressed in HEK293 cells was classified as a mutant that could not effectively expressed and

reconstituted with 11-*cis*-retinal. This suggested that D190N-Rho may have folding and/or trafficking issues. A separate screen (120) effectively expressed human D190N-Rho in COS-1 cells leading to some ambiguity about the structural effects of D190N. In mouse rods, we found that at least a small population of D190N-Rho molecules can fold properly and traffic to the outer segment. To look for any sign of endoplasmic reticulum stress, Jeannie Chen's laboratory is evaluating the level of proteins involved in the so-called unfolded protein response by Western blot.

### 3.9 Discussion

Interestingly, all Rho mutants implicated in visual impairment and many other single- or double-substitution mutants do not show a substantially shifted  $\lambda_{max}$  ( $494 \pm 14$  nm, Mean  $\pm$  SD from 88 mutants), and yet several Rho mutants (including D190N-Rho) are suspected to have higher rates of thermal isomerization. In testing the pigment noise theory with D190N-Rho, it appears that D190N-Rho does in fact have a  $\sim 4.5$ -fold higher molecular rate constant of thermal isomerization despite an unchanged  $\lambda_{max}$ . The critical wavelength of D190N-Rho and thus its isomerization energy barrier were unchanged, suggesting that its chromophore binding pocket may be more accessible than in WT-Rho. While this possibility is still being investigated, it would be consistent with the known structural position of D190 directly above the chromophore binding pocket. Because of a lower effective D190N-Rho content in the outer segment, it seems that  $Rho^{D190N/WT}$  rods do not experience a higher amount of dark isomerization noise. As such, the slow degeneration seen in  $Rho^{D190N/WT}$  rods may be caused by something other than excessive dark noise such as cell death induced by misfolded or mislocalized D190N-Rho.



### 3.10 Figures

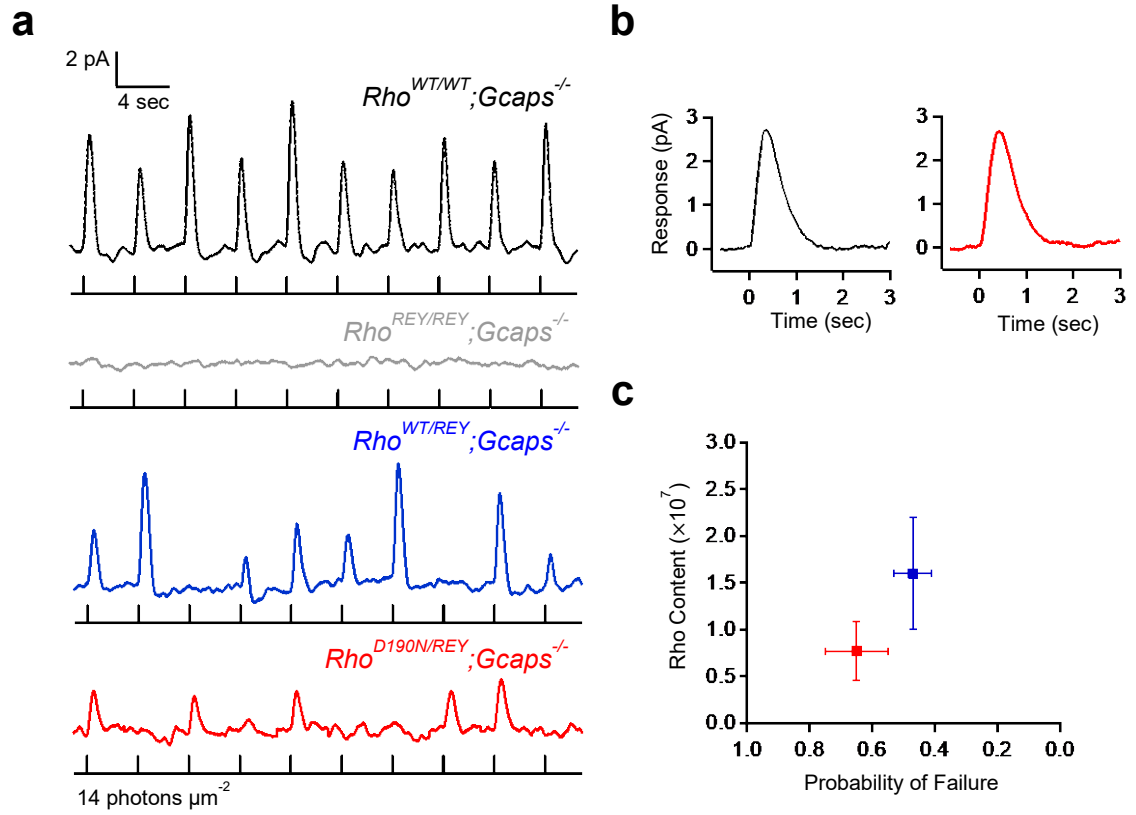


**Figure 3-1. D190N-Rho responses can be isolated and quantified by largely silencing G-protein signaling from endogenous Rho.** **a**, Dim-flash responses to the same flash strength (14 photons  $\mu\text{m}^{-2}$ ) in various genotypes. In black, a  $Rho^{WT/WT};Gcaps^{-/-}$  rod shows multiple events per flash with a very low probability of failure. In gray, a  $Rho^{REY/REY};Gcaps^{-/-}$  rod shows no discernible response. In red,  $Rho^{D190N/REY};Gcaps^{-/-}$  shows a high probability of failure with 5 out of 10 flashes giving presumably single-photon responses. In blue,  $Rho^{WT/REY};Gcaps^{-/-}$  shows a relatively low probability of failure because of the higher effective pigment content as compared to  $Rho^{D190N/REY};Gcaps^{-/-}$  rods (Data provided by Z. Chai). **b**, Single-photon responses obtained from quantal fluctuation analysis in  $Rho^{WT/WT};Gcaps^{-/-}$  rods (black) and  $Rho^{D190N/REY};Gcaps^{-/-}$  rods (red). **c**, Effective Rho content in the outer segment estimated from the measured probability of failure (3.4).

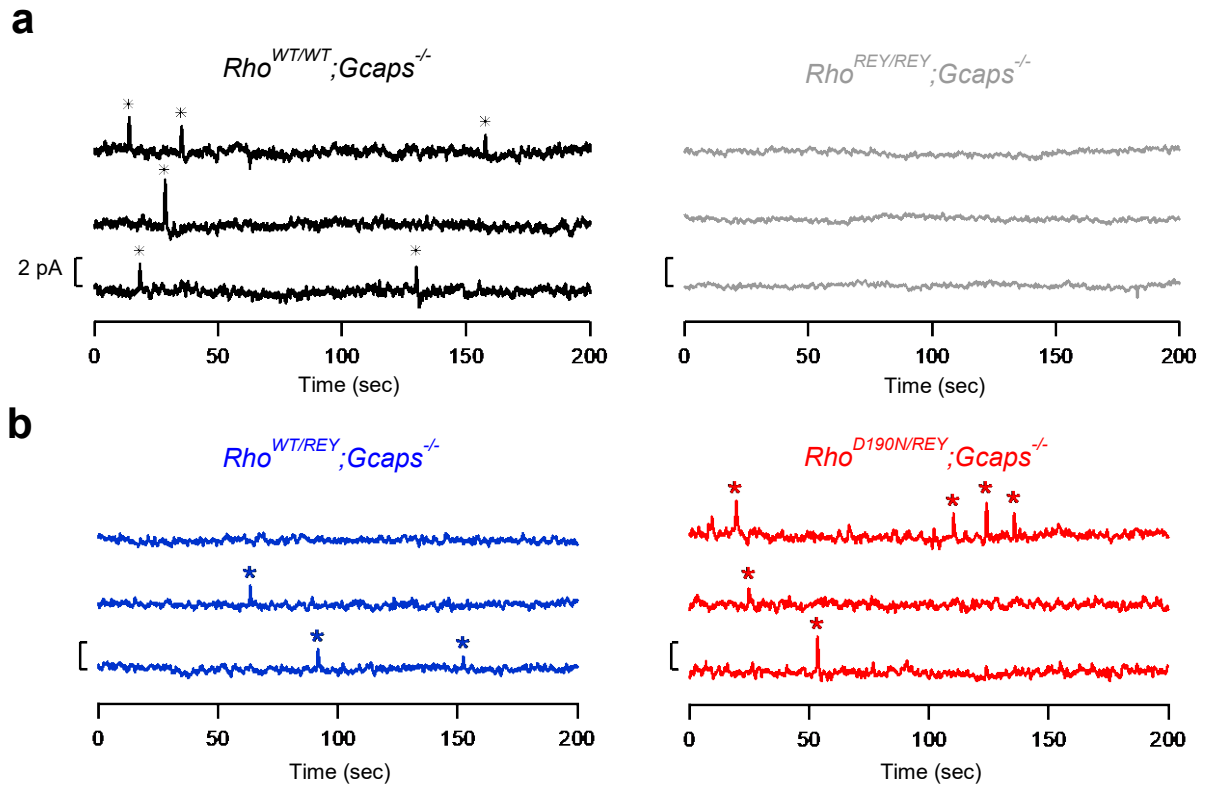


**Figure 3-2. Dark noise from D190N-Rho and WT-Rho.** **a**, Thermal isomerizations of WT-Rho seen as discrete events in dark noise from  $Rho^{WT/WT};Gcaps^{-/-}$  rods (black) were silenced by replacing WT-Rho with the the G-protein-binding-site mutant REY-Rho in  $Rho^{REY/REY};Gcaps^{-/-}$  rods (gray). **b**, Thermal isomerizations from D190N-Rho expressed from one allele could be isolated in  $Rho^{D190N/REY};Gcaps^{-/-}$  rods (red) and compared with rods expressing WT-Rho from one allele,  $Rho^{WT/REY};Gcaps^{-/-}$  rods (blue).

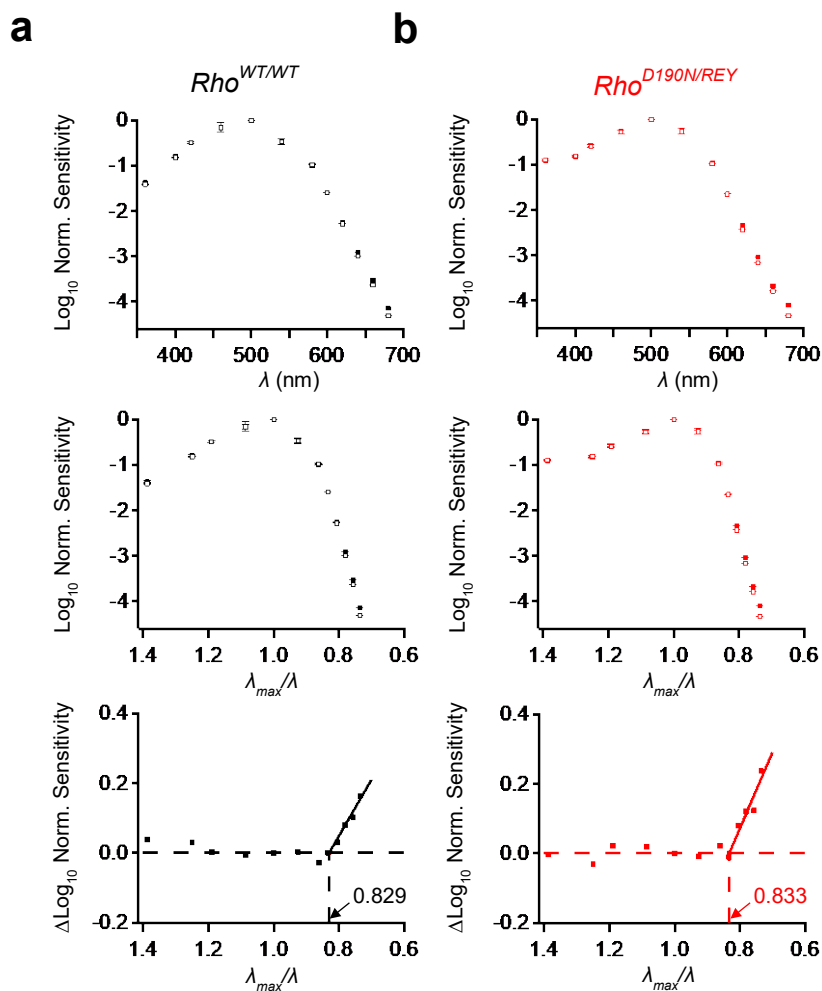


**Figure 3-3. The activation-energy barrier for isomerization is unchanged in D190N-Rho.** **a**, Control experiment with  $Rho^{WT/WT}$  (C57BL/6J) rods showing the effect of temperature on normalized action spectra (Top) at 25°C (open symbols) and at 37°C (closed symbols). Plotting normalized sensitivity against  $\lambda_{max}/\lambda$  (Middle) and subtracting the 25°C spectrum from the 37°C spectrum (Bottom) shows enhancement of photosensitivity by heat at longer wavelengths (i.e. in the lower energy region). The point where  $\lambda_{max}/\lambda$  marked a transition to temperature enhancement was 0.829, similar to the previously reported value from mouse rods. **b**, Similar analysis to **a**, but with  $Rho^{D190N/WT}$  rods (transition point = 0.833).

**Table 3-1. Parameters of flash responses of mouse rods for evaluating effects of D190N-Rho**

Genotype	$S_F$ (pA photon <sup>-1</sup> μm <sup>2</sup> )	$a$ (pA)	$t_{peak}$ (ms)	$N_{Rho}$ (molecules)
(1)* $Rho^{WT/WT};Gcaps^{-/-}$	1.19 ± 0.30 (n = 10)	2.8 ± 0.5 (n = 10)	365 ± 69 (n = 10)	6.5 × 10 <sup>7</sup>
(2) <sup>#</sup> $Rho^{D190N/WT};Gcaps^{-/-}$	0.43 ± 0.21 (n = 16)	2.3 ± 0.6 (n = 16)	304 ± 52 (n = 16)	(5.6 ± 1.6) × 10 <sup>7</sup> (n = 16)
(3) <sup>§</sup> $Rho^{WT/REY};Gcaps^{-/-}$	0.19 ± 0.09 (n = 12)	3.2 ± 1.2 (n = 12)	419 ± 77 (n = 12)	(1.6 ± 0.6) × 10 <sup>7</sup> (n = 12)
(4) $Rho^{D190N/REY};Gcaps^{-/-}$	0.05 ± 0.02 (n = 12)	2.8 ± 0.8 (n = 12)	414 ± 40 (n = 11)	(8.4 ± 3.2) × 10 <sup>6</sup> (n = 12)

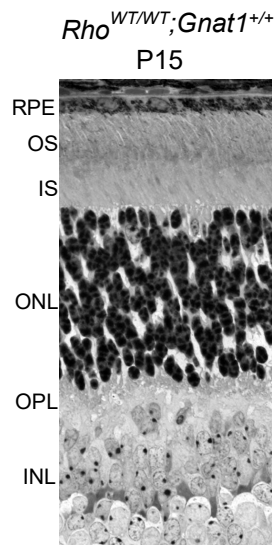
Values are mean ± SD, with the number of cells analyzed (n) in parentheses.  $S_F$  is the flash sensitivity;  $a$  is the quantal response amplitude;  $t_{peak}$  is the time-to-peak of dim-flash responses;  $N_{Rho}$  is the effective Rho content in the outer segment determined from the probability of failure from a dim-flash series (the established value is used for  $Rho^{WT/WT};Gcaps^{-/-}$ ). \*Data from Chapter 2. # Data provided by W. W. S. Yue. §Data from Z. Chai.

**Table 3-2. Parameters of dark noise for evaluating effects of D190N-Rho**

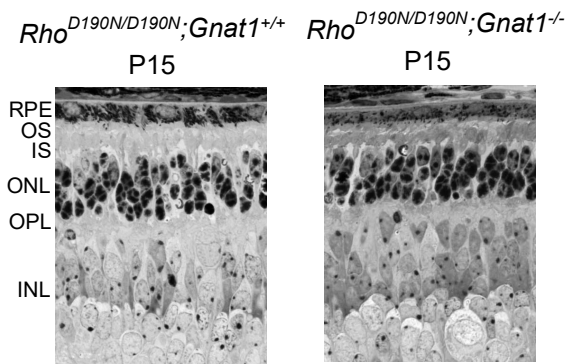
Genotype	Cellular Event Rate (s <sup>-1</sup> cell <sup>-1</sup> )	Molecular Event Rate (s <sup>-1</sup> )	$E_A$ (kcal mol <sup>-1</sup> )
(4) $Rho^{D190N/REY};Gcaps^{-/-}$	0.007 ± 0.003 (n = 12)	(8.6 ± 4.6) × 10 <sup>-10</sup> (n = 12)	47.7 kcal mol <sup>-1</sup> (n = 12)

Values are mean ± SD, with the number of cells analyzed (n) in parentheses. **Cellular event rate** was measured from dark noise filtered at 3 Hz to facilitate event identification. A discrete event was defined as an elevation in current >30% of the amplitude and with a duration between 50 to 200% of the integration time of the single-photon response measured in the same cell. **Molecular event rate** was calculated by dividing the cellular event rate by the effective Rho content (Table 3-1).  $E_A$  was calculated according to pigment noise theory (3.1).

**a**



**b**



**c**

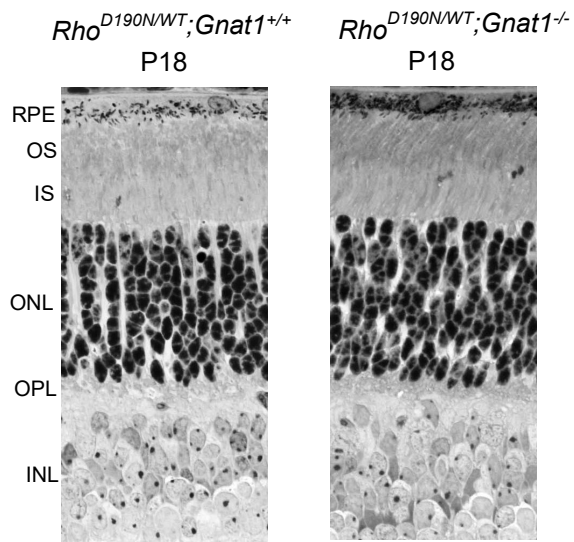


**Figure 3-4. Retinal degeneration caused by D190N-Rho is not rescued by removing G<sub>T</sub>α.** **a**, Histological cross-section showing the morphology of a healthy P15 retina ( $Rho^{WT/WT};Gnat1^{+/+}$ ). **b**, Severe degeneration in a P15 retina with both alleles expressing D190N-Rho ( $Rho^{D190N/D190N};Gnat1^{+/+}$ ) was not rescued by removing G<sub>T</sub>α ( $Rho^{D190N/D190N};Gnat1^{-/-}$ ). Note the substantially thinner outer nuclear layer as compared to panel **a**. **c**, Retinal degeneration is slower in  $Rho^{D190N/WT};Gnat1^{+/+}$  and  $Rho^{D190N/WT};Gnat1^{-/-}$  animals with healthy morphology at least up to P15. Histology from J. Chen's laboratory.

## Chapter 4. Dark noise and the apo-opsin effect in cones

### 4.1 Introduction

Rhodopsin's amplification and exceptional thermal stability (see Chapters 2 and 3) are both crucial for retinal rods to mediate scotopic (dim light) vision. Links between pigment properties and cone-mediated photopic (bright light) vision are much less understood. The  $\lambda_{max}$  of cone pigments from various species is much more variable than that of rhodopsin (Fig. 1-5), ranging from ultraviolet to red (360 to 620 nm). Largely from expressing cone pigments in rods, it has been found that the thermal isomerization rate of cone pigments increases substantially as  $\lambda_{max}$  increases due to a corresponding reduction in the isomerization-energy barrier (3.1). Much less is known about how this varying pigment property, and varying amounts of steady dark noise, affect cone signaling. In mammals, the absolute sensitivities and response kinetics of different cone subtypes are quite similar to each other, despite having different cone pigments with distinct thermal-noise properties (121, 122). In some lower vertebrates, such as salamander, however, red cones are, several-fold less sensitive and faster in response kinetics than blue cones (19, 123). The red cone pigment's high frequency of thermal-isomerization events (1, 19) as well as constitutive apo-cone-opsin activity in darkness (21) apparently act as a steady background signal ("equivalent" to real light) to desensitize salamander red cones ( $\lambda_{max} = 610$  nm). Salamander blue cones, on the other hand, are more than 10-fold as sensitive as red cones, perhaps in part due to their more stable pigment ( $\lambda_{max} = 444$  nm). It is still not known how different mammalian cone subtypes achieve similar sensitivity and kinetics despite having cone pigments with  $\lambda_{max}$  ranging from 425 nm (human blue-sensitive cones) to 530 nm



(human green-sensitive cones) or 560 nm (human red-sensitive cones). On a fundamental level, it has not been easy to measure exactly how much thermal noise is produced in situ by cone pigments or their respective apo-opsins and if there are other major sources of constitutive activity in the downstream cascade (e.g. transducin or phosphodiesterase (PDE) noise).

To approach quantifying dark noise in cones, the goldfish retina provides a unique opportunity because it has a relatively high proportion of cones [~25% of photoreceptors, (Balkema and Bunt-Milam, 1982)] with a diversity of subtypes: red-, green-, blue- and a minor population of UV-sensitive cones (not studied here), with  $\lambda_{max} = \sim 620, 540, 450,$  and 360 nm, respectively (124). Goldfish cones are also robust enough for dissociated single-cell physiology (Chapter 6, Fig. 6-5a) and truncated-cell recordings (Fig 4-2), which allows direct measurement of dark PDE activity driven by pigment noise or the constitutive signaling of apo-opsin, transducin, or spontaneous PDE events (19, 125).

Measurements from Prof. Dong-Gen Luo (now at Peking University) in our laboratory have shown that goldfish red cones had the lowest sensitivity and fastest response kinetics, followed by green and then blue cones. Using truncated-cone recordings, Prof. Luo verified that red cones indeed had the highest constitutive GTP-dependent activity in darkness, green cones had lower activity, and blue cones had non-measurable activity – in part reflecting their respective pigment stabilities. With intact red- and green-sensitive cones, I observed an increase in sensitivity following exposure to 11-*cis*-retinal, supporting the notion of constitutive apo-opsin signaling in goldfish cones. Downstream of opsin, Prof. Luo's truncated cone experiments also demonstrated a GTP-*independent* PDE activity in darkness that was similar across cone types. Thus, a goldfish

cone's specific pigment not only determines its  $\lambda_{max}$  for photoresponses, but also establishes the amount of constitutive dark signaling and resulting sensitivity shift in different cone types.

#### **4.2 Sensitivity and Response Kinetics of Goldfish Red-, Green- and Blue-Sensitive Cones.**

The flash responses of isolated goldfish cones were studied to evaluate their absolute sensitivity (defined as average response amplitude from each P\*) and response kinetics (Fig. 4-1a,b). Red-sensitive cones were the least sensitive producing  $4.2 \pm 0.3$  fA photons<sup>-1</sup>  $\mu\text{m}^{-2}$  or  $2.2 \pm 0.2$  fA photoisomerization<sup>-1</sup> on average after conversion for the estimated number of photoisomerizations per flash. The sensitivity of green-sensitive cones was higher being  $\sim 11$  fA per photoisomerization. Blue sensitive cones were most sensitive producing  $\sim 22$  fA per photoisomerization. It is important to note here that these tiny average response amplitudes do not necessarily indicate that every P\* produces the same small response. That is, some P\*s may not produce any response, thus lowering the population average, while other P\*s may produce a small number of G\*·PDE\*s. Taking absolute sensitivity as a rough approximation of transduction gain, Prof. Luo obtained a gain ratio of 1:5:10 for goldfish red, green and blue cones (Fig 4-1b). The dark current indicating the maximal available transduction current (measured from the saturated-response amplitude) also varied across cone types, which appeared to follow their respective outer-segment surface areas (Data not shown). Comparing dim-flash-response integration time ( $t_i$ , Methods), as an indication of the overall kinetics of the response. This parameter was fastest for red-sensitive cones ( $148 \pm 10$  msec, n=13), followed by green-

sensitive cones ( $232 \pm 32$  msec,  $n=8$ ), and slowest for blue-sensitive cones ( $354 \pm 38$  msec,  $n=8$ ).

The correlation between low sensitivity and fast response-kinetics is a hallmark of light-adaptation in rods and cones (126–128), suggesting that different dark-adapted goldfish cone types behave as if they experienced different degrees of “light” adaptation. This varying effect may be due to varying amounts of spontaneous pigment isomerization or constitutive activity downstream in the phototransduction cascade (19, 72). In comparison, goldfish rods, expressing the exceptionally stable rhodopsin, had a substantially larger absolute sensitivity ( $1.00 \pm 0.15$  pA photoisomerization<sup>-1</sup> ( $n=4$ )), and their dim-flash response's  $t_i$  was much longer ( $789 \pm 10$  msec ( $n=4$ )). While some of the differences between sensitivity and kinetics in rods and cones may be due to functional differences in rod-specific versus cone-specific isoforms of transduction proteins or in their expression levels, rods are known for exceptionally low dark noise in their transduction cascade (Chapter 3), whereas the dark noise in different cone types has not been thoroughly quantified.

#### **4.3 GTP-Dependent PDE Activity in Darkness.**

To directly quantify dark noise from the various cone types, Prof. Luo used a truncated cone preparation (19, 125), which allows direct measurement of PDE activity in darkness either driven by spontaneous pigment isomerization, opsin activity, transducin activity, or PDE noise. PDE does not require GTP for its spontaneous activity. However, GTP is believed to be crucial for activation of PDE by transducin (either from spontaneous

GTP-GDP exchange on the transducin alpha subunit or from spontaneous pigment isomerization leading to transducin activation).

To qualitatively evaluate GTP-dependent PDE activity, a cone was drawn outer-segment-first into the recording suction-pipette, and it was truncated with a glass microprobe to remove the proximal part of the inner segment together with the rest of the cell outside the pipette, leaving the intact outer segment (OS) and an open-ended, partial inner segment for dialysis by the bath solution (Fig. 4-2). The recording pipette was filled with a modified fish Ringer's solution containing low free  $\text{Ca}^{2+}$  concentration ( $\sim 0.1$  nM, buffered; Chapter 6), while the bath solution (Chapter 6) contained  $\sim 390$  nM free  $\text{Ca}^{2+}$ , chosen somewhat arbitrarily to match the free  $\text{Ca}^{2+}$  concentration measured optically in the intact salamander cone OS in darkness (129). One noteworthy limitation of the truncated cone prep is that the "intracellular" free  $\text{Ca}^{2+}$  (controlled by bath perfusion) is held approximately constant, preventing any  $\text{Ca}^{2+}$ -dependent feedback on pigment activity or downstream steps. The low  $\text{Ca}^{2+}$  concentration in the pipette was intended for minimizing any  $\text{Ca}^{2+}$  influx through the CNG channels to further prevent negative feedback that could introduce complexity in the relationship between PDE activity and CNG current.

Fig. 4-3a shows an experiment on a truncated red cone. There was initially no dark current at the OS without any source of cGMP in the bath solution (exposed to the intracellular space). Exposure to  $500 \mu\text{M}$  cGMP evoked a large inward current through the cGMP-gated channels in the outer segment membrane. When the cGMP-gated current reached a steady level, the bath solution was switched into one that contained, in addition,  $15 \mu\text{M}$  GTP [in order to permit transducin activation while minimizing cGMP synthesis by the endogenous guanylate cyclase; (125, 130)]. GTP induced a reduction in cGMP-gated

current that was restored shortly after its removal (5 red-sensitive cones gave the same results). Similar experiments with green cones showed a smaller reduction in the cGMP-induced current (Fig. 4-3b, n=6) and with blue cones there was no GTP-dependent current reduction (Fig. 4-3c, n=4). Thus, qualitatively, the dark GTP-dependent PDE activity was highest in truncated red cones, less in truncated green cones, and below detection in truncated blue cones. Because all cone types express the same transducin isoform (131), the lack of GTP-dependent PDE activity in blue-sensitive cones suggested that there is very little spontaneous transducin activity in red- and green-sensitive cones as well. The descending order of PDE activity with shorter  $\lambda_{max}$  also matches that of the spontaneous cone-pigment activities according to pigment noise theory (3.1). To assess the contribution of spontaneous pigment isomerization, Prof. Luo examined the effect of ATP on the GTP-induced PDE activity, because ATP is required for kinase activity leading to phosphorylation/arrestin-binding and ultimately silencing of pigment signaling. Exposure to 1-mM ATP reduced GTP-dependent PDE activity in a red-sensitive cone, confirming some contribution from pigment activity (Fig. 4-3d).

#### **4.4 Quantitative Measurement of PDE Activity in Darkness.**

For a more quantitative understanding of the dark noise in cones, cGMP is first applied to the outer segment (as above) and following its rapid removal, dark PDE activity can be quantified from the rate of cGMP dissipation by following the final single-exponential decline of the cGMP-gated current [(125) and Chapter 6]. Fig. Fig. 4-4 shows data from one such experiment on a red cone, plotted linearly (Fig. 4-4a) and semi-logarithmically (Fig. 4-4b) demonstrating the final single-exponential decline of cGMP-

gated current. This single-exponential decline is dictated by both the diffusion coefficient of cGMP in the cone outer segment and the dark PDE activity (Methods). The dark PDE activity can in turn be determined by repeating the above procedure in the presence of a PDE inhibitor, IBMX (1-mM). Without going deeply into the quantification here, Prof. Luo found that the GTP-independent dark PDE activity was similar across cone types.

With a GTP co-application step included in the above protocol, PDE activity driven by spontaneous pigment isomerization and constitutive apo-opsin signaling could be quantified. For example, by subtracting the decline rate constant of trace 1 from trace 2 in Fig. 4-4b, Prof. Luo estimated a GTP-dependent PDE activation rate-constant (Chapter 6),  $\beta = 0.042 \text{ s}^{-1}$ . The average  $\beta$  value was  $0.039 \pm 0.006 \text{ s}^{-1}$  for red-sensitive (n=10),  $0.004 \pm 0.001 \text{ s}^{-1}$  (n=7) for green-sensitive, and below resolution for blue-sensitive cones (n=3).

#### **4.5 Dark GTP-dependent PDE activity and the “equivalent” background light.**

As discussed above, the GTP-dependent PDE activity likely arises from thermal isomerization events and constitutive apo-opsin signaling to transducin. The GTP-dependent PDE activity could be further quantified by determining the steady light intensity required to produce the same amount of PDE activity. This required one more step to be added to the protocol shown in Fig. 4-5. Specifically, a steady light (at  $\lambda_{max}$ ) was applied producing a light-induced GTP-dependent PDE activity (Trace 3 - Trace 2) and repeated with another light intensity (Trace 4 in Fig. 4-5a). Plotting GTP-dependent PDE activity against light intensity (Fig. 4-5b), and extrapolating to the abscissa provided an “equivalent” light present in darkness of  $439 \text{ photons } \mu\text{m}^{-2} \text{ sec}^{-1}$  for this cell. Overall, the

estimated “equivalent” light in dark-adapted red-sensitive cones was  $615 \pm 107$  photons  $\mu\text{m}^{-2} \text{sec}^{-1}$  ( $n=10$  red cones; Fig. 4-6a). Similar experiments on dark-adapted green-sensitive cones gave an “equivalent” light of  $35 \pm 8$  photons  $\mu\text{m}^{-2} \text{s}^{-1}$  ( $n=7$ ; Fig. 4-6b). For dark-adapted blue-sensitive cones, the “equivalent” light was undetectable (Fig. 4-6c) as it was in the qualitative experiments above.

When I joined the laboratory, the primary goal was to figure out how much of the above “equivalent” light in dark-adapted cones was actually driven by constitutive cone-apo-opsin signaling for comparison with the amount driven by thermal isomerization events. In fully dark-adapted salamander red-sensitive cones, an estimated  $\sim 10\%$  of the total opsin content was found to exist without chromophore (21), believed to result from the red-cone pigment’s considerable rate of spontaneous chromophore release without isomerization as well as the high rate of thermal isomerization. In an ideal scenario, to isolate contributions from thermal isomerizations in the above experiments, 11-*cis*-retinal would be continuously perfused into the truncated cone to remove any contribution from apo-opsin to the measured GTP-dependent PDE activity. However, due to the high reactivity/toxicity of 11-*cis*-retinal (132) and its ability to block cyclic-nucleotide-gated channels (133), continuous perfusion would likely have other effects in addition to silencing apo-opsin signaling. Nonetheless, brief exposure of 11-*cis*-retinal to the outer segment or inner segment/cell body of salamander cones has been shown to enhance sensitivity by inhibiting apo-opsin in addition to restoring photon capture (21).

To probe for any apo-opsin signaling in goldfish cones, goldfish were dark-adapted overnight, individual cones were isolated from dissected retinae, and sensitivity was measured before and after exposure to 11-*cis*-retinal (Chapter 6). Representative results

are shown in Fig. 4-7, where the sensitivities of red-sensitive cones (with outer segments drawn into the pipette) were assessed from dim-flash responses over time. In Fig. 4-7a, a ~7-min exposure to 11-*cis*-retinal A1 resulted in a gradual increase in dim-flash sensitivity reaching a steady level (~1.5-fold higher than pre-treatment sensitivity) within ~5 min. Similarly, in Fig. 4-7b, after a brief (~4 min) exposure to the native goldfish chromophore, 11-*cis*-retinal A2, dim-flash sensitivity was ~1.4-fold higher than before exposure. Longer exposures did not further enhance sensitivity and, in many cases, prolonged exposure to 11-*cis*-retinal led to a substantial reduction in dark current (up to 50% of pre-treatment values) and a slowing of response kinetics (Fig. 4-11), perhaps due to the potential side-effects of 11-*cis*-retinal mentioned above. From the collected data, goldfish red-sensitive cones showed a sensitivity increase of  $(1.38 \pm 0.26)$ -fold when exposed to 11-*cis*-retinal A1 ( $n = 5$ ) and a sensitivity increase of  $(1.19 \pm 0.01)$ -fold when exposed to 11-*cis*-retinal A2 ( $n = 2$ ). The larger effect of A1- in comparison to A2-exposure may result from the stronger light-absorption of A1 versus A2 [1.4-fold higher extinction coefficient, (21, 134)]. Likewise, in a single green-sensitive goldfish cone that maintained stable dark current, the sensitivity increased by ~1.4 fold when exposed to 11-*cis*-retinal A1. These results confirmed the presence of apo-opsin signaling in goldfish red-sensitive and green-sensitive cones, even after overnight dark adaptation.

For the purpose of determining how much apo-opsin signaling was involved in the GTP-dependent PDE activity described above, we measured the amount of “equivalent” background light that would match apo-opsin’s desensitizing effects (i.e. the effects removed by 11-*cis*-retinal exposure). In Fig. 4-8a, after the sensitivity increase from 11-*cis*-retinal A2 treatment, a red-sensitive cone was exposed to incremental steps of light



until the sensitivity was brought back to its pre-treatment level, achieved with 10,352 photons  $\mu\text{m}^{-2} \text{sec}^{-1}$  ( $\lambda = 620 \text{ nm}$ ) for this cell. From two different red cones treated in the same way, the “equivalent” light was 10,181 and 8,738 photons  $\mu\text{m}^{-2} \text{sec}^{-1}$ . From another red-sensitive cone treated with 11-*cis*-retinal A1, the “equivalent” light was 6,494 photons  $\mu\text{m}^{-2} \text{sec}^{-1}$ . From one green-sensitive cone treated with 11-*cis*-retinal A1, the “equivalent” light ( $\lambda = 540 \text{ nm}$ ) was 750 photons  $\mu\text{m}^{-2} \text{sec}^{-1}$ .

With both red- and green-sensitive cones, the collected results show that the light “equivalent” to constitutive apo-opsin signaling in intact cones was 10- to 20-fold higher than the light “equivalent” to GTP-dependent PDE activity measured by Prof. Luo in truncated cones. Taking effective collecting area into consideration (Table 4-1) could not explain the apparent discrepancy. One major confounding factor was that we could not determine how much of the sensitivity increase from 11-*cis*-retinal treatment came simply from an increase in photon capture. The sensitivity increase from photon capture should not be included in the “equivalent” light because it would not contribute to GTP-dependent PDE activity. Ultimately, we were not able to make use of the measurements because they could not be directly subtracted from the “equivalent” light of GTP-dependent PDE activity.

It turns out that the “equivalent” light of GTP-dependent PDE activity in red-sensitive cones ( $615 \pm 107$  photons  $\mu\text{m}^{-2} \text{sec}^{-1}$ ) has almost no effect on their sensitivity because this intensity lies in an extremely flat region of the Weber-Fechner relation (Fig 4-9). Thus, with apo-opsin signaling being only some fraction of GTP-dependent of PDE activity, one might not expect the silencing of apo-opsin to have a noticeable effect on sensitivity. We did not find the Weber-Fechner relation to be significantly altered by 11-

*cis*-retinal exposure (comparing Fig. 4-8b with Fig. 4-9b, left). From this reasoning, it is conceivable that the observed effects of 11-*cis*-retinal could largely be due to an increase in photon capture (augmented with 11-*cis*-retinal A1 due to its 1.4-fold higher extinction coefficient). The same reasoning applies for green-sensitive cones because their “equivalent” light of GTP-dependent PDE activity would be expected to have a negligible effect on their sensitivity according to their Weber-Fechner relation (Fig. 4-9b, center).

Without being able to separate pigment isomerization from constitutive apo-opsin signaling in the measured “equivalent” light of GTP-dependent PDE activity, we were unable to get an accurate estimate of the cone-pigment-isomerization rate or cone-apo-opsin signaling in situ. It was, however, possible to make comparisons of the total dark spontaneous activity occurring in the various cone types and to ask what would be the effects on sensitivity and kinetics if green or blue cones were exposed to the same amount of dark activity as found in red cones.

#### **4.6 Background-Light Adaptation**

To assess the contribution of the total dark spontaneous activity to sensitivity in different cone types, Prof. Luo carried out the incremental-flash-on-background experiment (Fig. 4-9a). In each cone type, flash sensitivity decreases with background light intensity according to the Weber-Fechner relation (Chapter 6). Collected results gave an  $I_0$  (intensity that cuts sensitivity in half) of  $21,739 \pm 2829$  (n=8),  $1,049 \pm 142$  (n=6) and  $791 \pm 169$  (n=4) photons  $\mu\text{m}^{-2} \text{s}^{-1}$  for red, green, and blue cones, respectively.

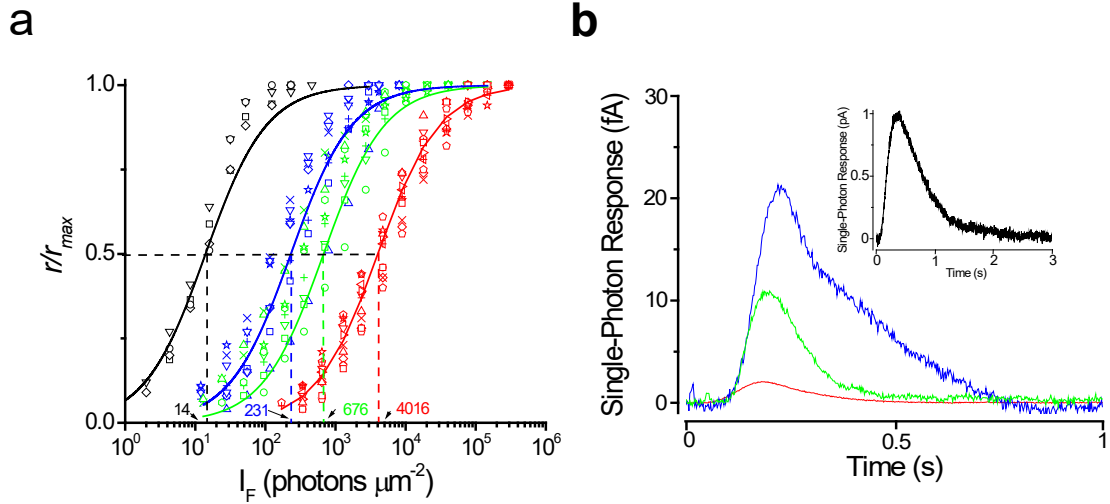
When subjected to a background light of  $1162$  photons  $\mu\text{m}^{-2} \text{s}^{-1}$  (similar to the “equivalent” light of GTP-dependent PDE activity in dark-adapted red cones), green cones

were adapted, lowering their flash sensitivity by 2.1-fold. Similarly, a step of 997 photons  $\mu\text{m}^{-2} \text{s}^{-1}$  adapts blue cones, lowering their flash sensitivity by 2.3-fold. Another hallmark of adaptation to background light is a speeding of response kinetics. When subjecting green and blue cones to the same amount of “equivalent” light measured in red cones, all cone types had similar response kinetics (Fig. 4-10).

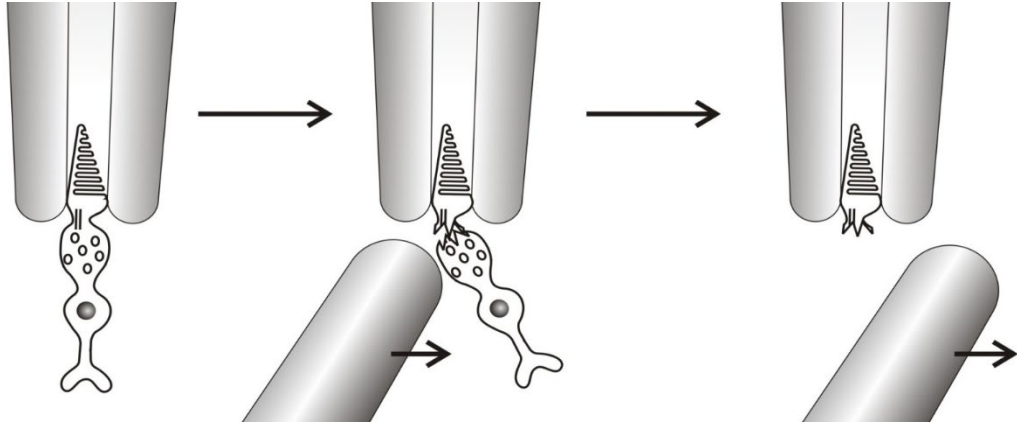
#### **4.7 Discussion**

Rod phototransduction has been studied at a quantitative level for several decades (135–138). By contrast, our quantitative understanding of cone phototransduction has lagged significantly. The peak-absorption wavelength varies much more widely for cone pigments than for rod pigments (Fig 1-5). Each cone type expresses an opsin with a unique absorbance maximum, but shares other key transduction proteins such as transducin, PDE, and cyclic nucleotide-gated (CNG) channel. Functionally, cones differ in not only spectral sensitivity but also light response properties (19, 123). Here we found that cone pigments, with their unique thermal stability and spontaneous chromophore dissociation dictate the amount of dark GTP-dependent PDE activity as well as the dark-adapted sensitivity of different cone types.

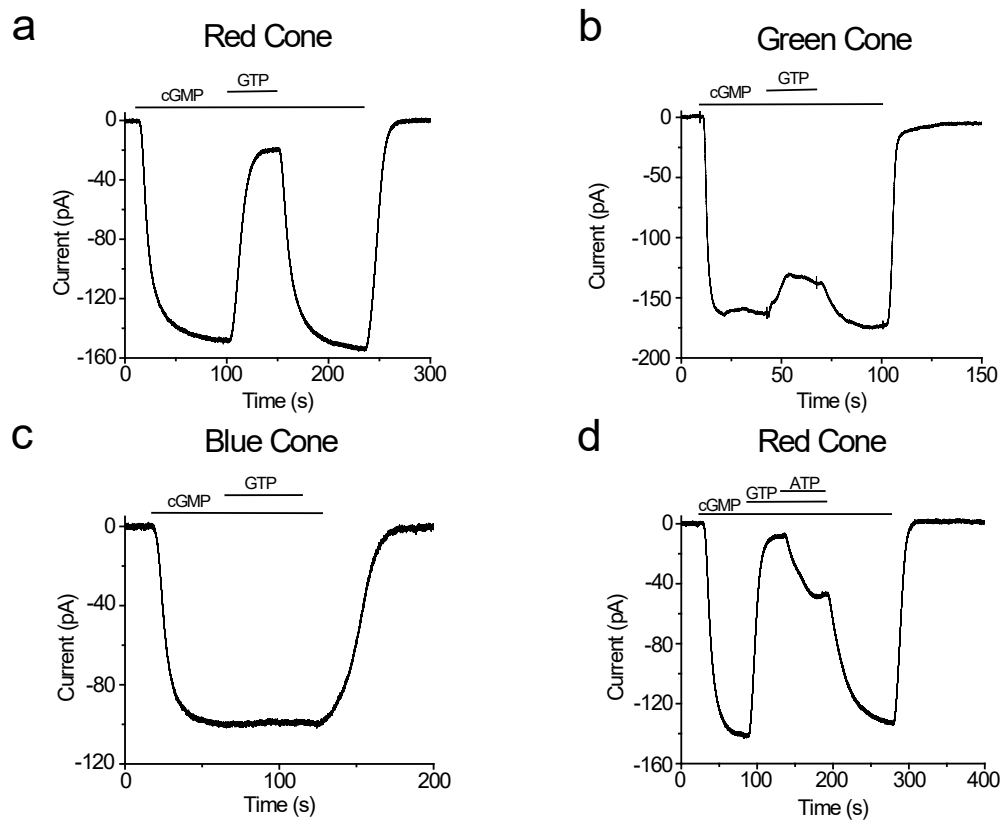
## 4.8 Figures



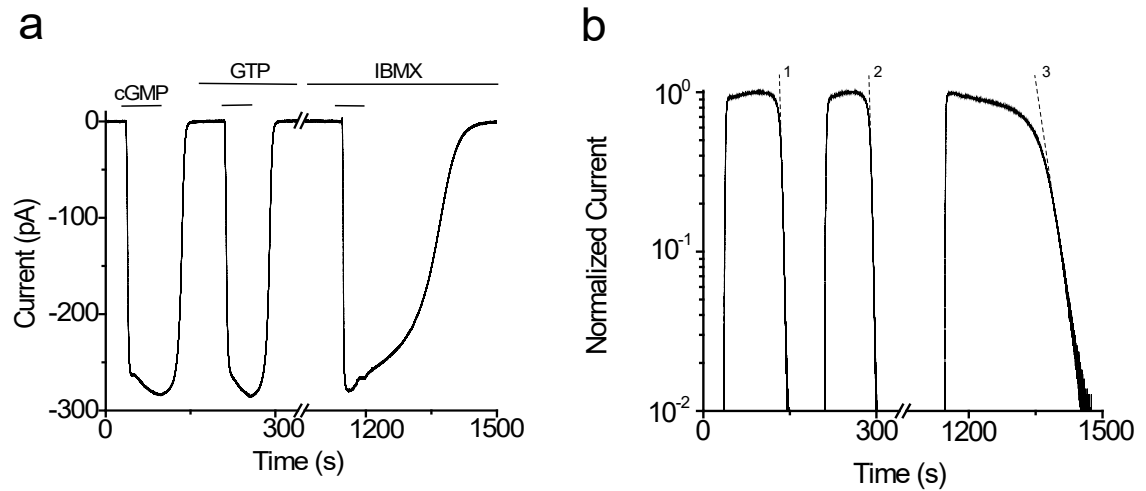
**Figure 4-1. Flash-response properties of goldfish photoreceptors.** **a**, Intensity-response relationship of red-, green-, blue-cones, and rods, represented by red, green, blue, and black symbols, respectively. The half-saturating intensities (in photons  $\mu\text{m}^{-2}$ ) were 4016, 676, 231, and 14 for red, green blue cones and rods. **b**, Average unitary responses of each cone type plotted as the mean dim-flash response divided by the estimated number of photoisomerizations per flash. Red, blue, and green traces are from red-, green-, and blue-sensitive cones respectively. The inset is the single-photon response of rods. Figure from D-G. Luo.



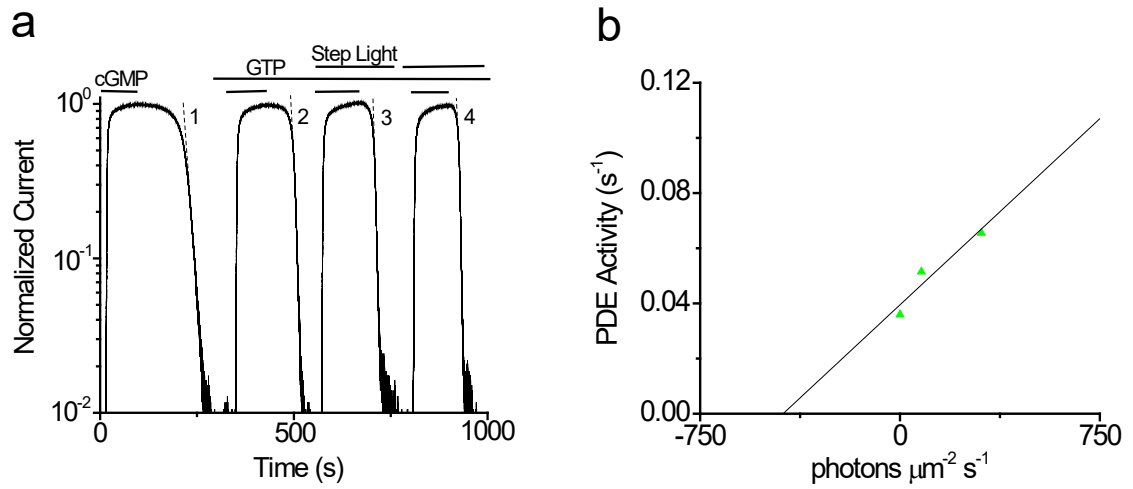
**Figure 4-2. Truncated cone preparation.** A conventional suction-pipette recording is first taken from a freshly-isolated goldfish cone. A probe with a blunt tip is used to truncate the cone parts outside of the recording pipette. After truncation, an open-ended cone outer segment is obtained. Figure from D-G. Luo.



**Figure 4-3. GTP-dependent PDE dark activities in cones.** **a-c**, Membrane current recorded from a truncated red, green and blue cone. Application of 500- $\mu$ M cGMP induced an inward current by opening CNG channels. Subsequent exposure to 15- $\mu$ M GTP elicited a sizeable reduction of CNG current in red cones, a smaller reduction in green cones, and no detectable change in blue cones. **d**, Addition of 1-mM ATP silenced some of the GTP-dependent current reduction in a red cone, perhaps by quenching pigment activity via ATP-dependent pigment phosphorylation by a cone pigment kinase. Figure from D-G. Luo.

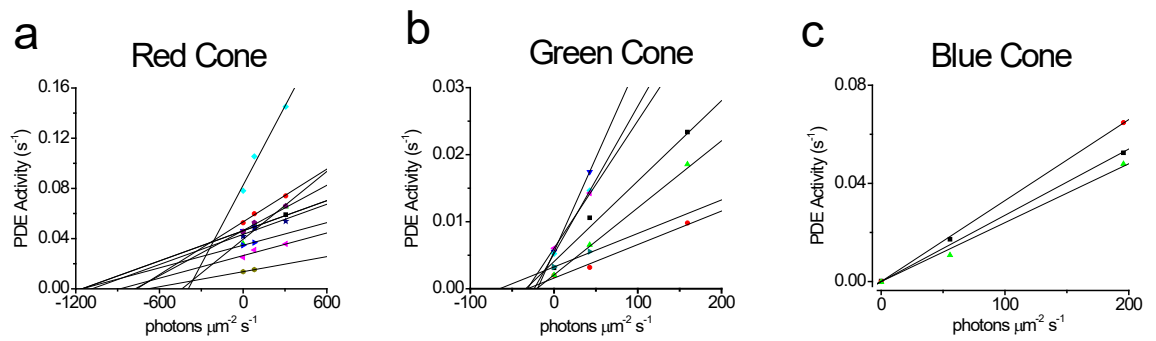


**Figure 4-4. Quantification of PDE dark activities.** **a**, Membrane current from a truncated red cone. The current decay was faster in the presence of 15- $\mu$ M GTP, but substantially slowed down by addition of 1 mM IBMX. **b**, Semi-log plot of data from **a**. The slope of the linear decay gives rate constants of 0.211, 0.311, and 0.039  $s^{-1}$  for trace 1, 2, and 3, respectively. Therefore, the rate constants of GTP-dependent (subtracting rate 2 by rate 1) and GTP-independent (subtracting rate 1 by rate 3) PDE activities are 0.042 and 0.072  $s^{-1}$ , respectively, after dividing by the Hill coefficient of CNG channels ( $n_H = 2.4$ ). Figure from D-G. Luo.

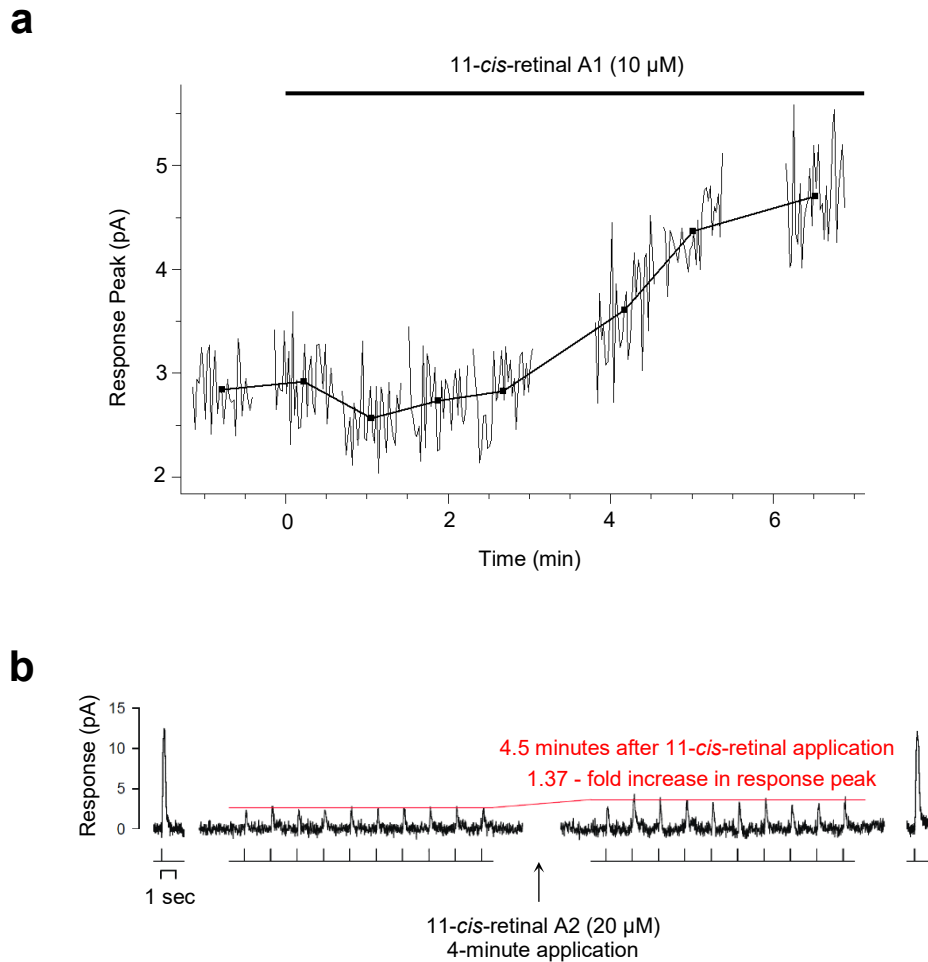


**Figure 4-5. “Equivalent” dark light for PDE dark activities.** **a**, GTP-independent and GTP-dependent current decay was first measured in the dark. GTP-dependent current decay was then measured under a steady light of 80, 305 photons  $\mu m^{-2} s^{-1}$  at 620 nm. **b**, GTP-dependent PDE activity (3-mM cGMP; 15- $\mu$ M GTP) versus steady background light intensity. A linear fit gives an x-intercept of -439 photons  $\mu m^{-2} s^{-1}$ , corresponding to the “equivalent” background light of GTP-dependent PDE activity in a dark-adapted red cone. Figure from D-G. Luo.



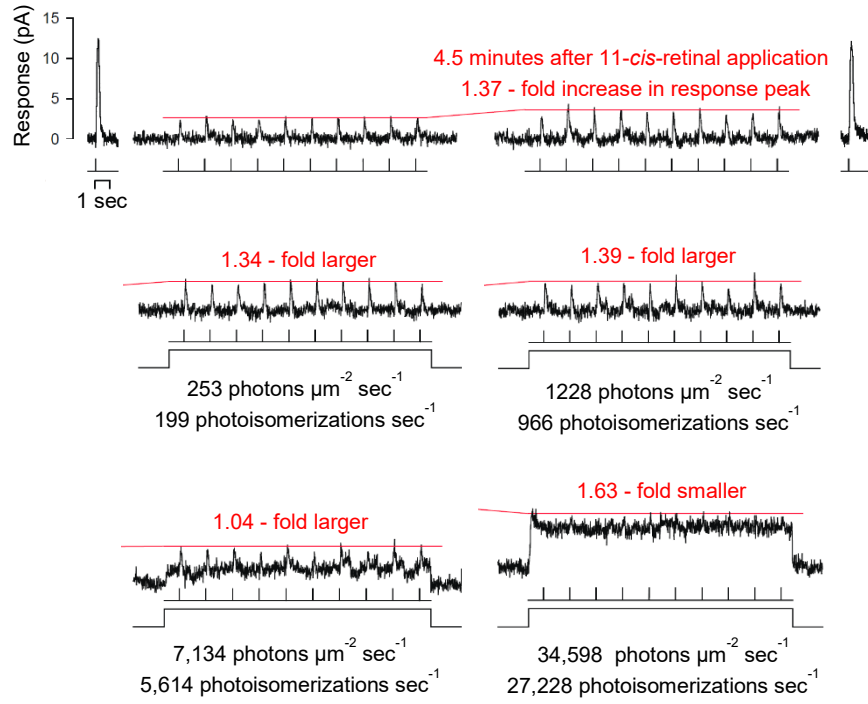
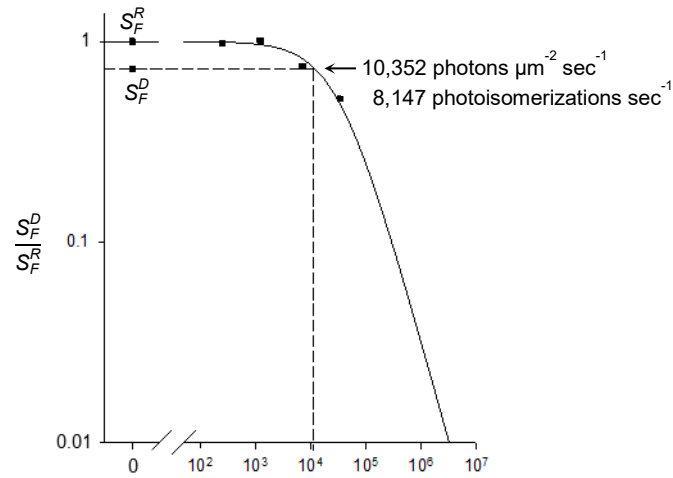


**Figure 4-6. Collected data of “equivalent” dark light.** **a**, Collected data from truncated red cones. **b**, and **c**, are results from truncated green and blue cones, respectively. Each color represents a set of measurements from a single cell. Figure from D-G. Luo.



**Figure 4-7. Effect of 11-*cis*-retinal exposure on the sensitivity of goldfish red cones.**

**a**, Dim-flash response peaks measured from a red-sensitive cone before and during application of 11-*cis*-retinal A1. Closed squares are the mean of each set of 30 dim-flash trials. 11-*cis*-retinal A1 (10  $\mu$ M) was applied for 7 min beginning at time zero. **b**, Dim-flash responses before and after a 4-min application of the endogenous chromophore, 11-*cis*-retinal A2 (20  $\mu$ M). The mean dim-flash response peak (indicated by the red line) increased to a steady level 4.5 min after chromophore application ended. Saturated responses were measured at the beginning and end of the experiment to verify that the dark current and response kinetics had not been altered during the experiment.

**a****b**

**Figure 4-8. “Equivalent” background light of apo-opsin in red cones.** **a**, The same cell as in Fig. 4-7b, but also showing a series of background light intensities applied to evaluate the amount of light that would restore the sensitivity back to the pre-chromophore-treatment level. **b**, Fold-change in sensitivity plotted against steady background light intensity in the red cone shown in **a**.  $S_F^D$  is the dark-adapted pre-chromophore-treatment sensitivity (in pA photons<sup>-1</sup> μm<sup>2</sup>).  $S_F^R$  is the post-chromophore-treatment sensitivity (in pA photons<sup>-1</sup> μm<sup>2</sup>). The solid curve is the fit by the Weber-Fechner relation (**Chapter 6**), where  $I_o$  is the light intensity that reduces sensitivity by half. For this cell,  $I_o$  was 32,557 photons μm<sup>-2</sup> sec<sup>-1</sup>.

**Table 4-1. Comparison of red cone dimensions, dark current, and sensitivity**

Parameters	Measurements from D. Silverman (n = 8)	Measurements from D-G. Luo (n = 19)
Outer Segment Height ( $\mu\text{m}$ )	$13.0 \pm 2.6$	$16.1 \pm 0.4$
Outer Segment Base ( $\mu\text{m}$ )	$4.0 \pm 0.5$	$5.1 \pm 0.2$
Outer Segment Tip ( $\mu\text{m}$ )	$2.2 \pm 0.4$	$2.7 \pm 0.1$
Outer Segment Volume ( $\mu\text{m}^3$ )	$103 \pm 32$	$202 \pm 13$
Dark Current (pA)	$15.0 \pm 3.4$	$16.7 \pm 1.3$
Collecting Area ( $\mu\text{m}^2$ )	$0.99 \pm 0.31$	$1.93 \pm 0.12$
$S_F$ (pA/photons- $\mu\text{m}^{-2}$ )	$(1.91 \times 10^{-3}) \pm (6.53 \times 10^{-4})$	$(4.15 \times 10^{-3}) \pm (3.24 \times 10^{-4})$
$S_F$ (pA/photoisomerization)	$(1.93 \times 10^{-3}) \pm (6.61 \times 10^{-4})$	$(2.15 \times 10^{-3}) \pm (1.68 \times 10^{-4})$
Fraction of Dark Current/Photoisomerization	$(1.25 \times 10^{-4}) \pm (0.43 \times 10^{-4})$	$(1.29 \times 10^{-4}) \pm (1.29 \times 10^{-4})$

**Table 4-2. Effects of 11-*cis*-retinal on goldfish cones and the “equivalent” background light of apo-opsin activity**

Cone Type	$S_F^D / S_F^R$	“Equivalent” background (photons $\mu\text{m}^{-2} \text{sec}^{-1}$ )	“Equivalent” background (photoisomerizations $\text{sec}^{-1}$ )
Red cone + 11- <i>cis</i> -retinal A1	$1.38 \pm 0.26$ (n = 5)	6494 (n = 1)	8299 (n = 1)
Red cone + 11- <i>cis</i> -retinal A2	$1.25 \pm 0.11$ (n = 3)	$9757 \pm 887$ (n = 3)	$9294 \pm 2574$ (n = 3)
Green cone + 11- <i>cis</i> -retinal A1	1.57 (n = 1)	750 (n = 1)	696 (n = 1)

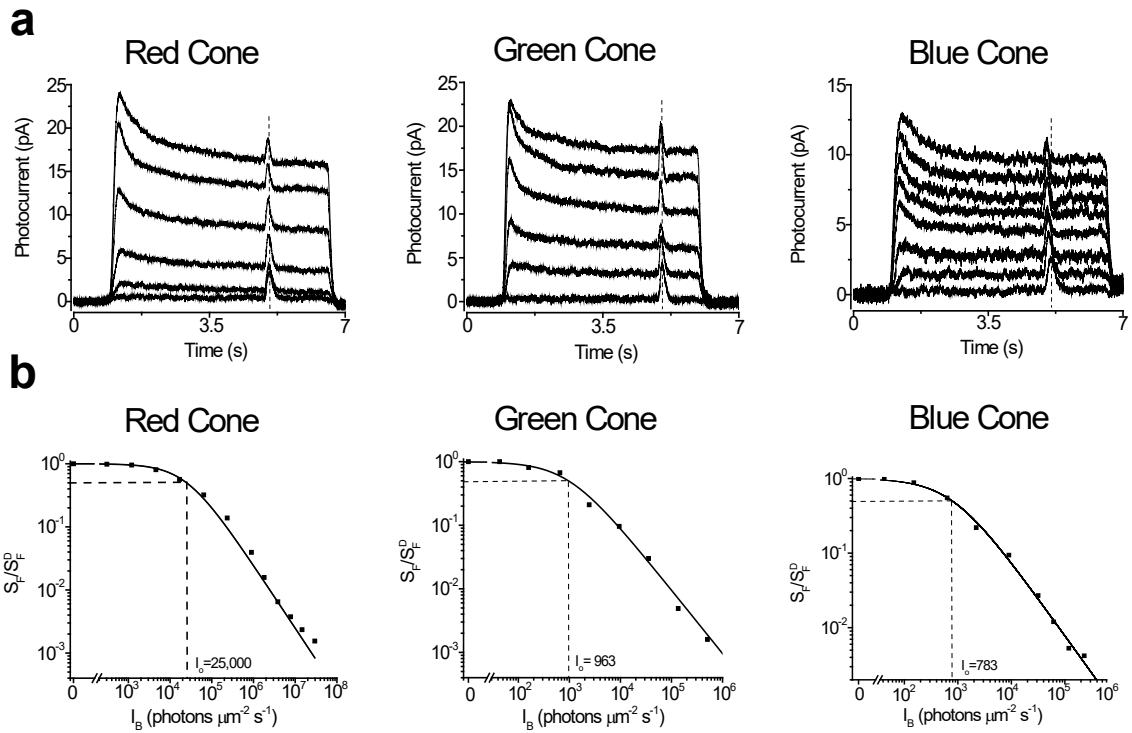


**Figure 4-9. Cone adaptation by steady light.** **a**, A single isolated cone was recorded with conventional suction-pipette recording technique. Flashes were used to probe the photosensitivity at response steady state of 5-s light of different intensities. Left, middle, and right panels represent a red, green, and blue cone, respectively. **b**, Incremental sensitivity as a function of background light. The normalized fold-change in sensitivity due to light adaptation is plotted against steady background light intensity. Curves are fits by the Weber-Fechner relation (**Chapter 6**), where  $I_0$  (in photons  $\mu\text{m}^{-2} \text{s}^{-1}$ ) was 25,000 (red cones), 963 (green cones), and 783 (blue cones). Figure from D-G. Luo.

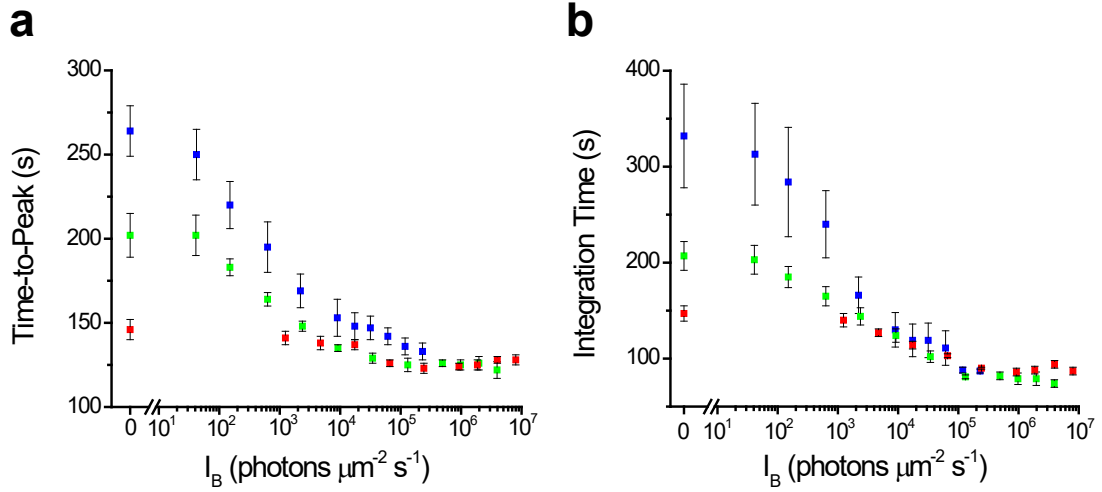
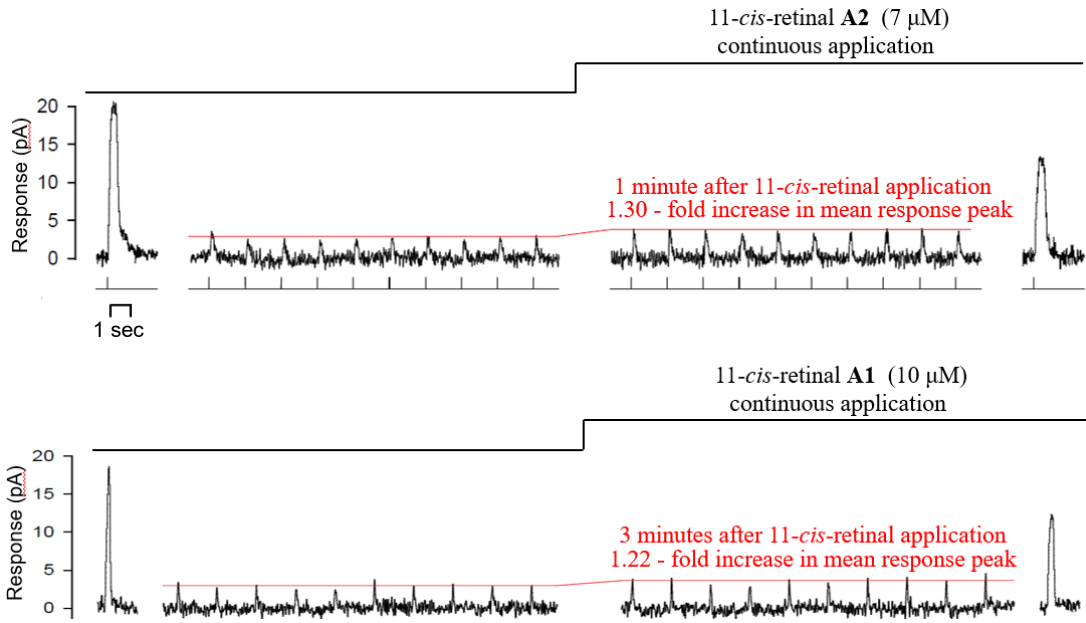


**Figure 4-10. The effect of background light on response kinetics. a,** Dependence of time-to-peak on background lights. **b,** Dependence of integration time on background lights. Red, green and blue symbols represent red, green and blue cones, respectively.

**a**



**b**

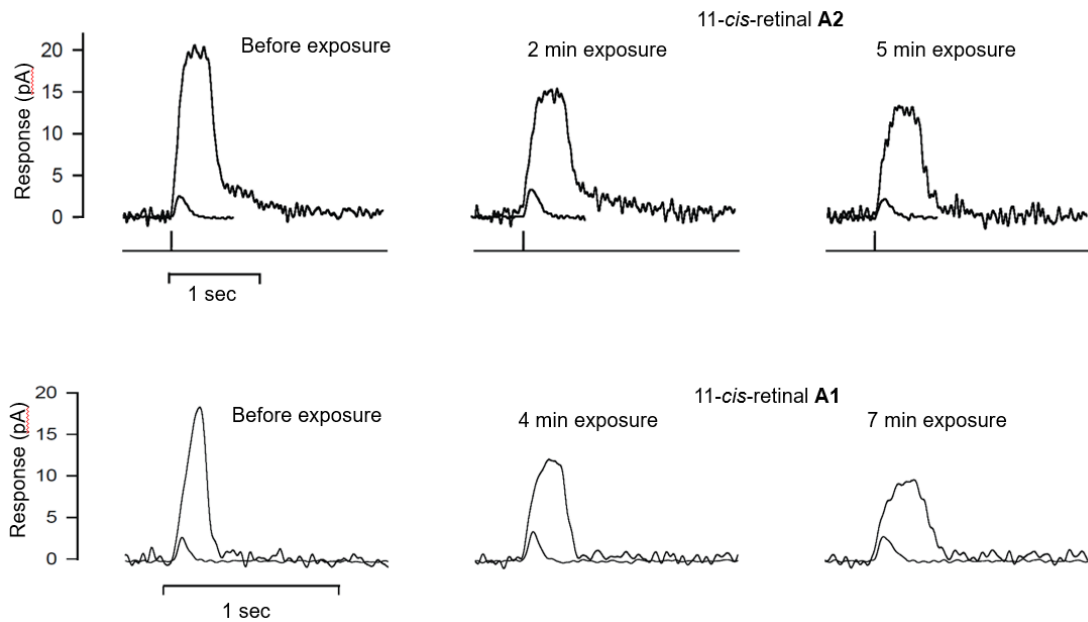




**Figure 4-11. Deleterious effects of prolonged 11-*cis*-retinal exposure.** a, Dim-flash responses measured from red-sensitive cones before and during prolonged exposure to 11-*cis*-retinal A2 (top) and A1 (bottom). Dim-flash sensitivity did not increase more than when cones were exposed to chromophore for less than 4 min. However, with continuous chromophore exposure, the saturated-response amplitude progressively decreased (down to ~50-75% of pre-treatment value) and response kinetics became substantially slower. These deleterious effects were seen often during continuous application of chromophore and were not seen during application of a “mock” control solution lacking chromophore. The exact cause for the adverse effects of prolonged chromophore exposure could have been from CNG-channel block or some form of retinal toxicity. Brief (< 4 min) application of chromophore typically induced an increase in sensitivity while maintaining the saturated-response amplitude throughout the experiment (Fig. 4-8).

## Chapter 5. Hybrid rod/cone pigments

### 5.1 Introduction

Even from the first studies of photoreceptor morphology in many diverse animals (40), it was clear that nocturnal and crepuscular species typically have rod-dominated retinæ specialized for vision in dim light, whereas diurnal species often have more cones and in some cases cone-dominant retinæ for vision in bright light. Rods from a variety of species mediate dim-light vision because of their relatively high signal amplification and low dark noise (Chapters 2 and 3). Cones are less sensitive than rods, even in darkness, in part, due to relatively high dark noise (at least in red- and green-sensitive cones) and low signal amplification (single-photon responses  $\ll 1$  pA; see Chapter 4). In bright light, cone pigments regenerate substantially faster than rods (139, 140).

In many cases, pigment properties directly influence dark noise and regeneration kinetics in photoreceptors. For example, mammalian rhodopsin is exceptionally stable, limiting discrete dark noise in rods, and has slow photointermediate decay and chromophore regeneration (138). Likewise, human red cone pigment is  $\sim 500$ -fold less stable than rhodopsin (18), producing higher dark noise, and has a  $\sim 10$ -fold faster decay of active photointermediates in situ, contributing to fast cone recovery (18, 140). To further test pigment noise theory (3.1) in relation to how pigments influence photoreceptor function, more measurements are needed from a diversity of pigments and photoreceptors.

## 5.2 Alligator rhodopsin

In certain reptiles, the rod-cone distinction is not as clear. The American alligator (*Alligator mississippiensis*) retina is separated into a superior rod-dominant region, expressing a single rhodopsin ( $\lambda_{max} = 501\text{-}503$  nm) in rods, and an inferior cone-rich region with four different cone types ( $\lambda_{max} = 443, 503, 535,$  and  $566$  nm), and speculation that one of the cone types expresses rhodopsin (141). Additionally, alligator rhodopsin extracted from alligator rods showed pigment regeneration comparable to the long-wavelength sensitive ( $\lambda_{max} = 562$ ) chicken cone pigment, being ~20- to 30-fold faster than that of frog, bovine, or chicken rhodopsin (25, 142). It is still not known if other aspects of alligator rhodopsin are also cone-like, such as its thermal stability and susceptibility to chromophore exchange and thus the amount of dark noise it generates in alligator rods. To compare light responses and dark noise of alligator rods with rods and cones of other vertebrates, I conducted experiments with acutely-isolated alligator retinæ.

Fig. 5-1a shows preliminary suction-pipette recordings where a series of dim-flash responses were first measured to demonstrate response kinetics and quantal response size (roughly from the smallest response amplitude). After a bright flash to evaluate saturated-response amplitude, several minutes of dark noise were recorded to quantify the discrete event rate. The amount of dark noise did not appear to be very high, with discrete events occurring less than once per minute in this cell and similarly low dark noise in other rods. From estimating pigment content based on outer segment dimensions (59), the cellular rate of discrete events was predicted to be  $\sim 0.6 \text{ min}^{-1}$  if alligator rhodopsin has thermal stability similar to a rod pigment and  $\sim 16.5 \text{ min}^{-1}$  if similar to a cone pigment. The preliminary results suggest alligator rhodopsin exhibits rod-like thermal noise, as well as high

sensitivity and slow response kinetics (Fig. 5-1b and Table 5-1). Furthermore, alligator rhodopsin is not susceptible to chromophore exchange over a 6-hour incubation with 9-*cis*-retinal (Fig. 5-2a), and can be regenerated with 9-*cis*-retinal after bleaching (Fig. 5-2b), suggesting a closed/inaccessible chromophore-binding pocket similar to typical vertebrate rhodopsins (21, 104).

### 5.3 Tokay gecko pigments

The Tokay gecko (*Gekko gekko*) is nocturnal with a rod-only retina where most rods express a green-sensitive pigment with  $\lambda_{max} = 521$  nm (known as P521) and a minority of rods express a blue-sensitive pigment with  $\lambda_{max} = 467$  nm (P467) (27, 143). P521 shares ~77% amino acid identity with human red cone pigment and ~44% identity with human rhodopsin (27). The rate of photointermediate decay and regeneration of P521 are cone-like (144). Also similar to typical cone pigments, P521 readily undergoes chromophore exchange when exposed to exogenous retinal (145), suggesting a more “open” chromophore-binding pocket and a higher rate of thermal isomerization events and higher dark noise perhaps interfering with dim-light vision according to pigment noise theory (3.1).

P467, on the other hand, shares ~82% identity with chicken green cone pigment and ~72% identity with human rhodopsin. Less is known about P467's photointermediate decay, regeneration rate, and susceptibility to chromophore exchange because of its rare occurrence [expressed in only ~20% of gecko photoreceptors, (143)]. Thus, it is still puzzling how P521 and P467, with some similarities to cone pigments, can mediate dim-

light vision in rods. Notably, downstream components in the Gecko phototransduction cascade are also cone-like (146).

It may be possible to isolate and quantify the thermal isomerization rates of P521 and P467 by expressing them in *Rho*<sup>REY/REY</sup>;*Gcaps*<sup>-/-</sup> rods (similar to our strategy for studying D190N-Rho in Chapter 3). One challenge will be to achieve trafficking sufficient amounts of P521 or P467 to the outer segment for dark noise measurements. This could possibly be achieved by replacing important trafficking residues from mouse rhodopsin (32, 147, 148) to the gecko pigments (Fig. 5-3). If every mouse rhodopsin molecule was replaced by P521, the predicted cellular rate of discrete events at 37°C is 2.3 min<sup>-1</sup> if the pigment's thermal stability is rod-like and 59 min<sup>-1</sup> if cone-like.

## 5.4 Discussion

We found that alligator rods show light response kinetics and sensitivity similar to rods from other species (e.g. toad) at room temperature despite having a rhodopsin with rapid pigment regeneration. Additionally, in terms of thermal isomerization, alligator rhodopsin appears to share properties with other known rod pigments. More work is needed to better understand how alligator rhodopsin may affect the physiology of alligator rods. Similarly, it is unclear how “cone-like” gecko pigments support scotopic vision in a nocturnal animal. Measuring the thermal isomerization rates of alligator and gecko pigments may provide insight into the physiology of these unique photoreceptors as well as help to further test pigment noise theory.

## 5.5 Figures

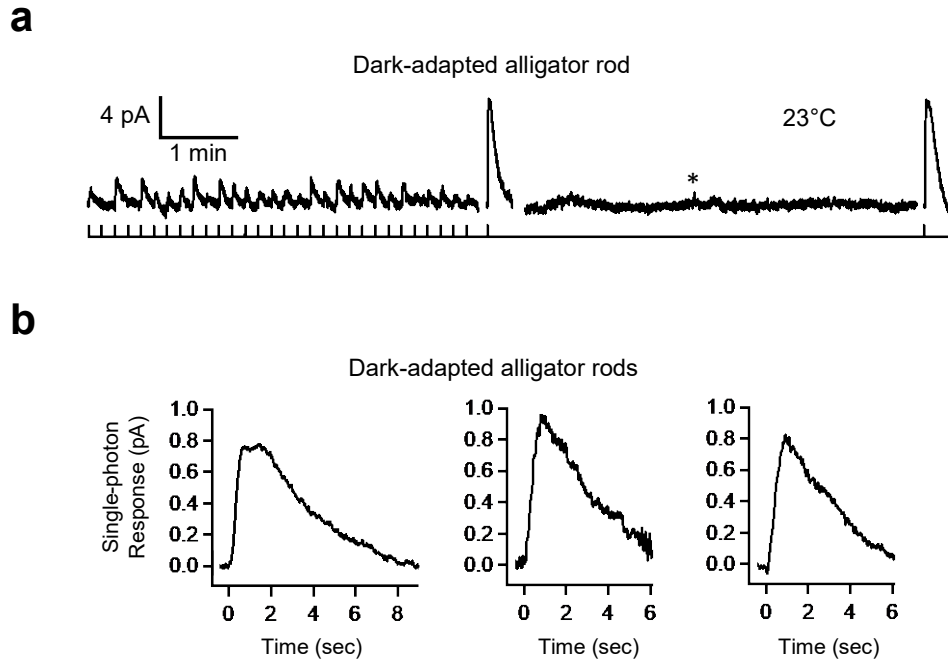


**Figure 5-1. Rod-like dark noise, sensitivity, and response kinetics measured from dark-adapted alligator rods.** **a**, Dim-flash response series to demonstrate the size and shape of small responses for comparison with dark noise recorded in the same cell. After a bright flash to measure the total dark current in this cell, several minutes of dark noise were recorded to determine if alligator rhodopsin produced isomerization events at the rate predicted for a cone pigment with  $\lambda_{\text{max}} = 503 \text{ nm}$  ( $\sim 16 \text{ min}^{-1}$  at  $23^\circ\text{C}$ ) or that of a rod pigment ( $\sim 0.6 \text{ min}^{-1}$  at  $23^\circ\text{C}$ ). **b**, Single-photon responses recorded from the same dark-adapted alligator rod as in **a** as well as those recorded from two other rods from the same alligator. Note the slow kinetics and relatively large response amplitude (c.f. goldfish cone responses in Chapter 4).

**Table 5-1. Comparison of rod outer segment dimensions, sensitivity and kinetics**

Parameters	Alligator Rods <sup>1</sup>	Toad Rods <sup>2</sup>	Salamander Red Cones <sup>3</sup>
Outer segment volume ( $\mu\text{m}^3$ )	46 to 154	900	79
$S_F$ (pA/photons- $\mu\text{m}^{-2}$ )	$5.5 \pm 0.2$ (n = 3)	$14.2 \pm 10.3$ (n = 9)	$0.02 \pm 0.02$ (n = 38)
$a$ (pA/Rho*)	$0.9 \pm 0.1$ (n = 3)	$1.0 \pm 0.3$ (n = 9)	$0.03 \pm 0.02$ (n = 38)
$t_{peak}$ (sec)	$0.9 \pm 0.2$ (n = 3)	$1.3 \pm 0.5$ (n = 13)	$0.1 \pm 0.03$ (n = 40)

<sup>1</sup>Alligator outer segment volume from (141). Outer segment length varies from 8 to 27  $\mu\text{m}$  at different retinal locations (e.g. rods in the superior region near the tapetum are longer than rods in the inferior region). Dim-flash response parameters are from my suction-pipette recordings. <sup>2</sup>Toad outer segment volume and dim-flash response parameters from (59, 149). <sup>3</sup>Salamander red cone outer segment volumes and dim-flash response parameters from (123). Dim-flash response parameters are mean  $\pm$  SD.

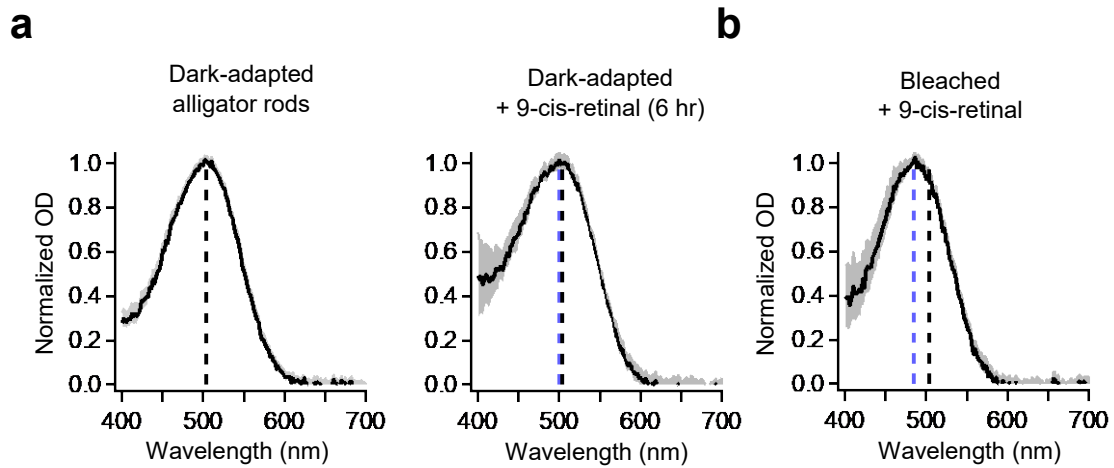


**Figure 5-2. Minimal chromophore-exchange of rhodopsin in alligator rods measured by microspectrophotometry.** **a**, Absorption spectra normalized to peak values from dark-adapted alligator rods acutely isolated from an alligator eye kept in darkness and either stored in physiological solutions ( $n = 28$  rods, left) or incubated in *9-cis*-retinal for 6 hrs before measurements ( $n = 34$  rods, right). Note that  $\lambda_{max}$  was 503 nm (black dashed line) on left and 500 nm (blue dashed line) on right indicating minimal chromophore-exchange over 6 hrs. **b**, Absorption spectrum after >99% bleach of alligator rhodopsin followed by regeneration with *9-cis*-retinal ( $n = 43$  rods) instead of the native *11-cis*-retinal revealing a more substantial shift to ( $\lambda_{max} = 485$  nm, blue dashed line). Solid black curves in all spectra are ensemble means from individual cells. Gray traces are ensemble means  $\pm$  SD. Raw data from R. Frederiksen.



Opn1SW ( <i>H. sapiens</i> )	KQFQACIMKMVCGKAM----TDESDTCSQKTEVSTVSSTQVGEN
Opn1SW ( <i>M. musculus</i> )	KQFRACILEMVCRKPM----ADESDVSGSQKTEVSTVSSSKVGEH
Opn1LW ( <i>H. sapiens</i> )	RQFRNCILQLFGKKV----DDGSELSASKTEVSSVSS--VSEPA
Opn1MW ( <i>H. sapiens</i> )	RQFRNCILQLFGKKV----DDGSELSASKTEVSSVSS--VSEPA
P467 ( <i>G. gecko</i> )	KQFRNCMVTTCGKNPFGDEDVSSVSQSKTEVSSVSSSQVAPA
Opn2 ( <i>B. taurus</i> )	KQFRNCMVTTLCCGKNPLGDDAESTTVSKTEF-----SQVAPA
Opn2 ( <i>M. musculus</i> )	KQFRNCMLTTLCCGKNPLGDDASATASKTEF-----SQVAPA

**Figure 5-3. Amino acid sequence alignment of C-termini from various visual pigments.** The C-terminal trafficking sequence VAPA is recognized by Arf4, a small GTPase important for rhodopsin trafficking (147). However, other sequences have been identified that participate in trafficking (32, 147, 148). To attempt to increase outer segment pigment content from heterologous expression of gecko pigments or human cone pigments in mouse rods, it may be beneficial to switch a foreign pigment's C-terminus with that of mouse rhodopsin.

## **Chapter 6. Methods**

### **6.1 Physiology (Chapters 2, 3, 4, 5)**

Electrical recordings of photoreceptor membrane current help to elucidate fundamental details of phototransduction. Single-cell recording from the outer segment, OS, is the standard method (150) for studying light responses and dark noise with various mouse lines and other animal species. The method is illustrated in Fig 6-1a, with an outer segment gently pulled into a tightly-fitting glass electrode where OS membrane current is recorded using a patch-clamp amplifier and membrane voltage is free to vary—considered a “pseudo” cell-attached loose patch configuration (151) in the more common patch-clamp terminology. The photomicrograph in Fig 6-1b shows a mouse rod illuminated with infrared light and imaged with an infrared image converter during a suction-pipette recording experiment.

### **6.2 Suction-pipette recording from mouse rods (Chapters 2, 3)**

Mice of 1- to 3-month-old were used for experiments. Under dim red light, an eye was removed from an acutely-euthanized mouse, with the retina isolated under infrared illumination into Locke’s solution (112.5-mM NaCl, 3.6-mM KCl, 2.4-mM MgCl<sub>2</sub>, 1.2-mM CaCl<sub>2</sub>, 3 mM Na<sub>2</sub>-succinate, 0.5-mM Na-glutamate, 0.02-mM EDTA, 10-mM glucose, 0.1% MEM vitamins (M6895, Sigma-Aldrich), 0.1% MEM amino-acid supplement (M5550, Sigma-Aldrich), 10-mM HEPES, pH 7.4 and 20-mM NaHCO<sub>3</sub>). The retina was divided into 3 pieces, one used immediately for recording while the others stored

in Locke's solution bubbled with 95% O<sub>2</sub>/5% CO<sub>2</sub> at room temperature until use for no more than 6 hrs.

For recording, a piece of retina was chopped into small fragments on a Sylgard plate with a razor blade. The tissues were then transferred to a recording chamber and perfused with Locke's solution at  $37.5 \pm 0.5^\circ\text{C}$ . Temperature was monitored by a thermistor situated adjacent (within 3 mm) of the recording pipette tip. Single-cell recordings involved drawing a rod's outer segment into a glass pipette containing physiological solution (140-mM NaCl, 3.6-mM KCl, 2.4-mM MgCl<sub>2</sub>, 1.2-mM CaCl<sub>2</sub>, 0.02-mM EDTA, 10-mM glucose and 3-mM HEPES, pH 7.4).

The light stimulus was typically a 10-ms flash of monochromatic light. Signals were sampled at 2 kHz through an Axopatch 200B amplifier and low-pass filtered through two separate channels at 1 kHz and 20 Hz (RC filter, Krohn-Hite Model 3343). The 1 kHz and 20 Hz channels were compared to measure the time delay (~58 ms) caused by filtering. This delay was corrected to define time zero when plotting responses. Unless otherwise specified, recording traces presented in figures are 20-Hz filtered. Filtering at 3 Hz was in some cases used to count discrete events during dark noise recordings or to display a series of dim-flash responses.

### **6.3 Photobleaching (Chapter 2)**

For bleaching experiments (Fig. 6-2), a retina was peeled away from the retinal pigment epithelium while immersed in pre-bubbled (95% O<sub>2</sub>/5% CO<sub>2</sub>) Locke's solution, with the addition of lipid-free BSA (1 mg/ml, A6003, Sigma-Aldrich) to facilitate clearance of all-*trans*-retinoids after bleaching (70). Under infrared illumination, the retina

was flat-mounted in solution on a piece of black filter paper (HABP02500, Merck Millipore Ltd) with photoreceptors facing upward. A petri dish containing the flat-mounted retina was placed on a platform centered vertically under a LED light source ( $\lambda_{\text{max}} = 470$  nm) equipped with an aspherical collimating lens (M470L2, Thor Labs) and a 10-nm bandpass filter centered at 480-nm. Light intensity was calibrated before each experiment. The flat-mounted retina was exposed to a light step calculated to bleach a targeted number of rhodopsin molecules (see below). Immediately following bleaching,  $\sim 1$  to  $2 \text{ mm}^2$  of tissue was cut from the central retina to ensure their vertical orientation for approximately uniform bleaching, with light traveling down the long axis of the outer segment.

Bleached retinal tissue was transferred to a storage chamber consisting of a silane-coated glass slide at the bottom of a plastic-walled chamber. A gentle stream of  $\text{O}_2/\text{CO}_2$  was blown across the surface of the solution, not far ( $\sim 4 \text{ mm}$ ) from the tissue sitting at the bottom of the chamber. The volume of storage solution was kept roughly constant (changing by  $<5\%$  over 30 minutes) with a syringe of distilled water dripping through a 33-gauge needle at a rate approximately equal to the evaporation rate (verified before each experiment). This method allowed storage with good  $\text{O}_2/\text{CO}_2$  supply but without foaming of the BSA-Locke's solution. After 30 minutes of storage, the tissue was finely chopped in Locke's solution without BSA on a Sylgard plate and transferred to the recording chamber. Photoisomerized rhodopsin transitions through several intermediate states (meta-I, II, and III) before releasing all-*trans*-retinal to become Opn. In mouse rods, meta-II decays with a biexponential time course (time constants of  $\sim 4$  and  $16 \text{ min}$  at  $37^\circ\text{C}$ ) with  $\sim 5\%$  of meta-II signal remaining at 30 min after light onset (70). Meta-III decay is slower, with  $>10\%$  meta-III signal remaining also at 30 min after light onset (70, 152). Although meta-III

cannot activate  $G_T$ , it can occasionally convert back to meta II (153). In order to record exclusively from noise originating from Opn molecules, bleached rods were recorded in 1-3 hours after bleaching in order to allow photointermediates to decay to Opn.

#### 6.4 Bleaching calculations (Chapter 2)

To calculate the number of photoisomerizations from a light stimulus, we used:

$$\frac{dn(t)}{dt} = I_i \times A \times Q \quad (1)$$

where  $n(t)$  is the number of rhodopsin molecules bleached in a rod at time,  $t$ , after light onset,  $I_i$  is light intensity (in incident photons  $\mu\text{m}^{-2} \text{sec}^{-1}$ ),  $A$  is the photon-collecting area ( $\sim 0.6 \mu\text{m}^2$  if light propagates transversely), and  $Q$  is the quantum efficiency of isomerization (0.67 isomerizations per absorbed photon (116)).  $A$  is given by the product of the molecular extinction coefficient,  $\alpha_\lambda$ , of rhodopsin (116) oriented in the disk membrane ( $\alpha_{500 \text{ nm}}$  is  $1.76 \times 10^{-8} \mu\text{m}^2$  and  $\alpha_{480 \text{ nm}}$  is  $1.54 \times 10^{-8} \mu\text{m}^2$ ), the rhodopsin content in a dark-adapted rod,  $n_o$  [ $6.5 \times 10^7$  molecules for a typical mouse rod (1)], and a polarization factor due to the orientation of rhodopsin approximately perpendicular to the outer segment long axis [0.5 for transverse illumination with unpolarized light (59)].

When light propagates down the long axis of an outer segment in our bleaching experiments, photons are absorbed by rhodopsin near the distal face before they can propagate to rhodopsin near the proximal face—causing light intensity to fall exponentially along the length of the outer segment, (known as “self-screening” (154)). This effect dissipates during large bleaches as rhodopsin density decreases. Hence, the photon-collecting area changes with time and when accounting for self-screening, Eqn. 1 becomes:

$$\frac{dn(t)}{dt} = I_i \times C \times (1 - \exp(-\alpha_\lambda \times \frac{n_o - n(t)}{V} \times L)) \times Q \quad (2)$$

where  $C$  is the cross-sectional area of a disk membrane ( $1.5 \mu\text{m}^2$ ),  $V$  is the outer segment's volume and  $L$  is its length. Eqn 2, was solved for our bleaching experiments. Light stimuli of 480 nm and  $150,000 \text{ photons } \mu\text{m}^{-2} \text{ sec}^{-1}$  were delivered with the following durations: 8.8 sec for a 1% bleach, 45 sec for a 5% bleach, 72 sec for an 8% bleach, 91 sec for a 10% bleach, 190 sec for a 20% bleach, 299 sec for a 30% bleach. The solution to Eqn 2. is:

$$\frac{(-(\log_e(\text{ABS}(((1/\exp(-\alpha_\lambda * ((n_o - n(t))/V)*L)-1))+1))))/((\alpha_\lambda * L/V))+(\log_e(\text{ABS}(((1/(\exp(-\alpha_\lambda * (n_o /V)*L)-1))+1))))/((\alpha_\lambda * L/V)))/(-Q*I_i)}$$

To validate the above calculations, we did 10% and 20% bleaches calculated as above on flat-mounted WT C57BL/6J mouse retinae and measured the resulting rod desensitization with suction-pipette recordings (Fig. 6-3). We found a degree of desensitization ( $k \approx 35$ , see legend) similar to published values based on transverse bleaching verified by microspectrophotometry (70).

## 6.5 Analysis of post-bleach noise (Chapter 2)

For events with waveform  $f(t)$  and occurring randomly at a mean rate of  $\nu \text{ s}^{-1}$ , the mean and variance of the steady signal resulting from such events are, according to Campbell's Theorem, given by (79):

$$\text{Steady Noise Mean} = \nu \int f(t) dt \quad (3)$$

$$\text{and Steady Noise Variance} = \nu \int [f(t)]^2 dt \quad (4)$$

Substituting  $f(t) = a' \hat{f}(t)$ , where  $\hat{f}(t)$  is normalized  $f(t)$  at transient peak (i.e., of unity height) and  $a'$  is the peak amplitude of  $f(t)$ , we have:

$$\text{Steady Noise Mean} = a' v \int \hat{f}(t) dt \quad (5)$$

$$\text{and Steady Noise Variance} = [a']^2 v \int [\hat{f}(t)]^2 dt \quad (6)$$

$$a' = [\text{Steady Noise Variance} / \text{Steady Noise Mean}] \times \left\{ \int \hat{f}(t) dt / \int [\hat{f}(t)]^2 dt \right\} \quad (7)$$

We obtained the steady noise mean as the difference between the cell-cohort-averaged dark current without bleaching and that long after a bleach, and likewise for the steady noise variance (in both cases with recording segments containing discrete noise excluded). The expression  $\left\{ \int \hat{f}(t) dt / \int [\hat{f}(t)]^2 dt \right\}$ , called the shape factor (see Appendix for sample calculations), is not very sensitive to the exact shape of  $\hat{f}(t)$  and is between 1 and 2 for typical physiological responses (79). The  $\hat{f}(t)$  deduced from the post-bleach continuous-noise power spectrum (see 6.7) gave a shape factor of  $1.54 \pm 0.03$  (n = 5 cells after a 5% bleach) and similar values for other bleaching conditions and the  $G_{T\alpha}$ -underexpressor. As such, the amplitude ( $a'$ ) and waveform  $[\hat{f}(t)]$  of the unitary event can be derived.

## 6.6 Validation of Campbell's theorem (Chapter 2)

While Campbell's theorem has been used to study the underlying unitary events involved in many phenomena (78, 79), it is often assumed without scrutiny that Campbell's theorem can accurately extract the amplitude and event frequency of a Poisson process. This assumption can be tested with a computer simulation (Appendix). Briefly, if one sets the amplitude, waveform, and event frequency of randomly-occurring events in a computer-simulated Poisson process, then the calculations from Campbell's theorem (described in 6.5) can be used to extract the unitary amplitude and event frequency for

comparison with the known input values. Fig. 6-4 shows a simulation where unitary event amplitude,  $A$ , is 0.05 pA, the waveform is a single-exponential decline (Fig. 6-4a). The simulation (Fig. 6-4b) is a random process beginning at time zero with inter-event intervals following an exponential probability distribution with average rate parameter of 10 events  $\text{sec}^{-1}$ . Calculations from Campbell's theorem (Fig. 6-4c,d) gave an estimated unitary amplitude of 0.044 pA and event frequency of 11.4  $\text{sec}^{-1}$ , both within 15% of the actual values.

## 6.7 Power Spectral Analysis (Chapter 2)

Power spectra (155) for continuous dark noise in post-bleach and dark-adapted control rods were calculated from recording segments not containing discrete events (11) using Clampfit 10.5.2.6 (Molecular Devices; San Jose, CA). Spectral resolution was chosen to resolve the low-frequency plateau of each power spectrum:  $\sim 0.04$  Hz for  $Rho^{WT/WT};Gcaps^{-/-}$  (requiring  $\sim 26$ -sec epochs) and  $\sim 0.02$  Hz for  $Gnat1^{Tg};Gnat1^{-/-};Rho^{WT/WT};Gcaps^{-/-}$  (requiring  $\sim 52$ -sec epochs). In displayed spectra (Figure 2-1d), data between 0.02 and 0.3 Hz represent averages of two adjacent frequency points, data from 0.32 to 2.4 Hz represent averages of four adjacent frequency points, and data  $>2.4$  Hz represent averages of five adjacent frequency points. Averaging reduced scatter across all frequencies without changing the shape of the power spectrum. To determine the shape of the single-Opn\* effect underlying post-bleach noise, we subtracted the cohort-averaged dark control spectra from post-bleach spectra for each genotype and bleaching condition. This difference spectrum was then best-fit with the power spectrum of a function, typically the convolution of 2 single-exponential-decline functions (time constants in legends of



Figures 2-1, 2-2 and Table 2-2, and see Appendix for the convolution of 2, 3, and 4 exponential declines).

### **6.8 Incubation with 11-*cis*-retinal (Chapter 2)**

For application of chromophore to mouse rods, 10 minutes after light exposure, bleached tissue was transferred to a glass vial containing 11-*cis*-retinal (30  $\mu\text{M}$ ) in 2 mL of BSA-Locke's (pre-bubbled with  $\text{O}_2/\text{CO}_2$ ). The glass vial was inverted gently 5 times during a 10-minute incubation and then the tissue was stored without 11-*cis*-retinal for 10 minutes before chopping and transferring to the recording chamber.

### **6.9 Quantal analysis (Chapters 2, 3, 5)**

Within the linear foot of a rod's intensity-response relation, dim flashes evoke quantized responses interspersed with failures, which result from photons passing through the outer segment without being effectively absorbed. Photon absorption is stochastic and dim-flash response amplitudes follow a Poisson distribution (59), with time-dependent mean,  $\mu = n \times A$ , and variance,  $\sigma^2 = n \times A^2$ , where  $n$  is the mean number of responses per flash and  $A$  is the single-photon response amplitude. Thus,  $A$  can be determined from the transient peak of  $\sigma^2/\mu$ . In situations where some dim-flash responses exceed the linear range (such as when a negative feedback is removed with the *Gcaps*<sup>-/-</sup>), the peak  $\sigma^2/\mu$  may not accurately reflect  $A$ . Instead, the initial rising phase of the response can be analyzed by comparing  $\sigma^2$  and  $\mu^2$  where  $\sigma^2 = \frac{1}{n} \times \mu^2$  and  $\frac{1}{n}$  indicates the mean number of events per flash, which can be used to calculate  $A$  from either the  $\sigma^2$  or  $\mu$  waveforms.

## 6.10 Measurement of thermal isomerization noise (Chapters 2, 3, 5)

Measuring thermal isomerization events from mouse rods over minutes requires exceptional recording stability and low instrumental noise. Recordings were optimized using pipettes with a tip opening of  $\sim 1$  to  $1.5 \mu\text{m}$  and a resistance of 8 to 7 MOhm in recording solutions at room temperature. Slow electronic drift was minimized by using a vacuum-free chamber constructed to use a long exit port with a wick to draw solution out at the same rate that it entered the chamber. The ground electrode consisted of a capillary holder (World Precision Instruments; Sarasota, FL, MEH900S) filled with pipette solution, an embedded Ag/AgCl pellet, and connected to the bath by a glass capillary filled with 1M KCl in a 3% agar gel. Dark noise was recorded in 10-min epochs, filtered by two separate channels at  $f_c = 3$  Hz for counting discrete events and 20 Hz for calculating dark noise variance. Discrete events were counted using the criteria of peak amplitude  $>30\%$  of the single-photon response measured from the same cell and duration of 50 to 200% of the single-photon response's integration time. These criteria were enforced using MATLAB to count discrete events and routinely validated by eye.

## 6.11 Western blot (Chapter 2)

Retinas were dissected from acutely-euthanized mice into RIPA lysis buffer (140-mM NaCl, 0.1% Na-deoxycholate, 10-mM Tris-HCl, pH 8.0, 1-mM EDTA, 0.5-mM EGTA, 1% Triton X-100 and 0.1% SDS). The tissues were grinded with polypropylene pestles (Sigma-Aldrich) and vortexed every 5 min over a 30-min incubation on ice to release proteins from cells. We measured total protein concentrations with the bicinchoninic acid (BCA) Protein Assay Kit (Pierce) and loaded 20  $\mu\text{g}$  of protein extracts

for each sample onto 4%-20% continuous SDS-Polyacrylamide gels (Bio-Rad), where proteins were separated by electrophoresis and transferred to polyvinylidene difluoride (PVDF) membranes. The membranes were blocked with 5% normal non-fat milk in TBST (500-mM NaCl, 20-mM Tris-HCl, pH 7.4, 0.1% Tween-20) for 1 hr at room temperature, then incubated with different primary antibodies in the same buffer at 4°C overnight. After several 10-min washes with TBST, membranes were further incubated with the appropriate HRP-conjugated secondary antibodies (1:10,000, Bio-Rad) for 1 hr at room temperature, followed by additional washes. Finally, proteins were detected by using the Enhanced Chemiluminescence (ECL) system (Pierce). Primary antibodies included a mouse anti-bovine rhodopsin (RHO) monoclonal antibody (1D4, 1:50, gift from Dr. Robert Molday, University of British Columbia), a rabbit anti-human  $G_T\alpha$ -subunit polyclonal antibody (SC-389, 1:500, Santa Cruz), a rabbit anti-human  $G_T\beta$ -subunit polyclonal antibody (1:1000, gift from Dr. C.-K. Jason Chen, Baylor College of Medicine), a rabbit anti-human  $G_T\gamma$ -subunit polyclonal antibody (1:1000, gift from Dr. C.-K. Jason Chen), a mouse anti-bovine phosphodiesterase-6 (PDE6) monoclonal antibody (1: 1000, gift from Dr. Theodore Wensel, Baylor College of Medicine), a mouse anti-bovine cyclic-nucleotide channel subunit A1 (CNGA1) monoclonal antibody (PMc1D1, 1:100, gift from Dr. Robert Molday), a mouse anti-bovine CNG channel subunit B1 (CNGB1) monoclonal antibody (GARP4B1, 1:1000, gift from Dr. Robert Molday), a rabbit anti-G-protein-coupled receptor kinase (GRK1) polyclonal antibody (A4101, 1:1000, gift from Dr. C.-K. Jason Chen), a rabbit anti-mouse arrestin-1 (ARR1) polyclonal antibody (1:2500, gift from Dr. C.-K. Jason Chen), a rabbit anti-mouse regulator of G protein signaling isoform 9 (RGS9) polyclonal antibody (1:1000, gift from Dr. Jason C.-K. Chen), a rabbit anti-human retinal

guanylate cyclase isoform 1 (RetGC1) polyclonal antibody (1:1000, gift from Dr. Alexander Dizhoor, Salus University) and a chicken anti-human glyceraldehyde 3-phosphate dehydrogenase (GAPDH) polyclonal antibody (AB2302, 1:500, Millipore). Experiments were repeated at least three times with different animals for each genotype.

To compare quantitatively the  $G_{T\alpha}$  expression levels in  $Gnat1^{Tg};Gnat1^{-/-};Rho^{WT/WT};Gcaps^{-/-}$  retinas and in  $WT$  (i.e.,  $Rho^{WT/WT};Gcaps^{-/-}$ ), we measured the concentrations of total protein extracts from  $WT$  and mutant retinas using the bicinchoninic acid (BCA) Protein Assay Kit (Thermo Fisher Scientific, Waltham, MA). Serial dilutions of  $WT$  protein extracts were prepared; to maintain equal protein content in each lane (verified by GAPDH blotting),  $Gnat1^{-/-};Gcaps^{-/-}$  extract was added accordingly. All extracts were separated in the same gel. After blotting for  $G_{T\alpha}$ , the pixel count of each band was measured by the Gel Analyzer function in ImageJ. The pixel counts of the  $WT$  bands were used to create a calibration curve for determination of the fold-difference in expression of  $G_{T\alpha}$  in  $Gnat1^{Tg};Gnat1^{-/-};Rho^{WT/WT};Gcaps^{-/-}$  rods. The  $G_{T\alpha}$  band intensity in 2.5  $\mu$ g total protein from  $Gnat1^{Tg};Gnat1^{-/-};Rho^{WT/WT};Gcaps^{-/-}$  was equivalent to a ~17.9-fold dilution from  $Rho^{WT/WT};Gcaps^{-/-}$  (i.e. 0.14  $\mu$ g total protein extract according to the calibration curve), indicating that  $G_{T\alpha}$  expression is 17.9-fold lower (~5.6%) in  $Gnat1^{Tg};Gnat1^{-/-};Rho^{WT/WT};Gcaps^{-/-}$ . This expression level ranged from ~5 to 8% in several Western blots.

## 6.12 Immunohistochemistry (Chapter 2)

To examine the subcellular localization of D190N-Rho in  $Rho^{D190N/WT}$  rods, we carried out immunohistochemistry. Cryo-sections were blocked with 10% newborn calf

serum (12023C, Sigma-Aldrich) in phosphate buffered saline containing 0.1% Triton X-100 (PBST) for 1 hour at room temperature, followed by the mouse anti-bovine rhodopsin antibody (156) (1D4 at 1:50 dilution in the same blocking solution at 4°C overnight). On the next day, sections were washed with PBST and incubated with Alexa-488-conjugated goat anti-mouse IgG antibody in blocking solution for 1 hr at room temperature. After several final washes with PBST, sections were mounted with anti-fade medium (H-1200, Vector Laboratories) containing 4',6'-diamidino-2-phenylindole (DAPI), and cover-slipped. Images were taken with Zeiss LSM 510 Confocal Microscope.

### **6.13 Isoelectric focusing to quantify pigment content (Chapter 3)**

Due to the distinct isoelectric point of REY-Rho versus D190N-Rho, we were able to use isoelectric focusing (IEF) to approximate the amount of different pigment species in *Rho*<sup>D190N/REY</sup> rods. Briefly, mice were dark-adapted overnight and euthanized under dim red light. Using only infrared illumination, retinae were separated from the retinal pigment epithelium in phosphate-buffered saline solution, immediately transferred to a 2-mL centrifuge tube and frozen by immersing in liquid nitrogen. Frozen retinae were kept in darkness by wrapping with multiple layers of aluminum foil and stored at -80°C until shipping on dry ice to the University of Southern California for IEF as described previously (81). After thawing, a retina was homogenized in a solution consisting of: 25-mM HEPES, pH 7.5, 100-mM EDTA, 50-mM NaF, 5-mM adenosine, 1-mM phenylmethylsulfonyl fluoride, and protease inhibitors. Homogenized samples were centrifuged for 15 min (19,000 × g, 4°C). After discarding the supernatant, the pellet was rinsed with 1 ml of 10-mM HEPES, pH 7.5, solution and resuspended in 1 ml of a solution containing 10-mM

HEPES, pH 7.5, 1-mM MgCl<sub>2</sub>, 0.1-mM EDTA, 2% BSA (w/v), 50-mM NaF, 5-mM adenosine, and protease inhibitors. The resuspended samples were incubated with 11-*cis*-retinal overnight at 4°C. After pelleting and rinsing again, the pellet was resuspended in 100 µl of a solution containing 10-mM HEPES, pH 7.5, 0.1-mM EDTA, 1-mM MgCl<sub>2</sub>, 10-mM NaCl, 1% dodecyl-maltoside, and 1-mM dithiothreitol) for 3 hrs at 4°C. After a final centrifugation step, samples were loaded with 5% glycerol (v/v) on a polyacrylamide gel (GE Healthcare). Isoelectric focusing proceeded for 2 hrs at 25 W (Pharmacia FBE 300 flatbed) followed by transfer onto a nitrocellulose membrane and detection by a monoclonal antibody (R2-12N) that binds the N-terminal residues of rhodopsin. The bands were visualized (LI-COR Biosciences) and band intensity quantified with ImageJ.

#### **6.14 Histology (Chapter 3)**

To evaluate the extent of retinal degeneration in animals expressing D190N-Rho (*Rho*<sup>D190N/D190N</sup> and *Rho*<sup>D190N/WT</sup>) for comparison with animals lacking transducin alpha (*Rho*<sup>D190N/WT</sup>;*Gnat1*<sup>-/-</sup> and *Rho*<sup>D190N/WT</sup>;*Gnat1*<sup>-/-</sup>), we studied the morphology of retinal sections at various ages collected in our laboratory, with each eye marked at the superior pole for orientation and fixed overnight in ½ Karnovsky Buffer and stored in 0.1 M cacodylate solution (without fixative), pH 7.2 until shipment to the University of Southern California for sectioning and histological staining. Epon sections were processed in the laboratory of Jeannie Chen as described previously (107).

### 6.15 Microspectrophotometry measurements from mouse rods (Chapters 2 and 3)

An eye of an acutely-euthanized mouse was removed under dim red light, with the retina isolated in HEPES (10 mM, pH 7.4)-buffered Ames medium (A1420, Sigma-Aldrich) under infrared illumination. A piece of the retina was transferred to a 2 mm-deep Plexiglass recording chamber, gently flattened by forceps on the bottom quartz cover-slip window of the chamber with the photoreceptors facing the incident light, and then secured by a slice anchor (Warner Instruments). The recording chamber was placed on a microscope stage located in the beam path of a custom-built microspectrophotometer. The retina was superfused at a rate of 4 ml/min with 35–37°C Ames medium (Sigma-Aldrich) buffered with sodium bicarbonate and equilibrated with 95% O<sub>2</sub>/5% CO<sub>2</sub>. We measured the absorption spectra at the edge of the retinal piece where isolated outer segments could be seen projecting transversely across the incident light beam. In this way, the polarization of the incident beam was parallel to the plane of the intracellular disks (T-polarization). Measurements were taken over the wavelength range of 300 – 700 nm with a 2-nm resolution. The  $\lambda_{max}$  was ~500 nm for every sample tested, confirming that the measured area contained predominantly rod photoreceptor outer segments, as opposed to cones. To increase the signal-to-noise ratio, we typically obtained 10 complete sample scans and 10 baseline scans for averaging. We calculated the absorbance spectrum from the Beers' Law,  $OD = \log(I_i/I_t)$ , where  $OD$  is the optical density,  $I_i$  is the light transmitted through a cell-free space close to the outer segments, and  $I_t$  is the light transmitted through the tissue.

### 6.16 Quantitative RT-PCR of D190N-Rho (Chapter 3)

To compare rhodopsin mRNA in *Rho*<sup>D190N/REY</sup> and *Rho*<sup>REY/REY</sup> mice, quantitative RT-PCR is currently being completed with forward primer: 5'-CTTCACAGTCAAGGAGGCG-3' and reverse primer: 5'-GCAGATCAGGAAGAAGATGACC-3'. Briefly, 2 retinæ from a mouse were homogenized in 1 mL TRIzol and incubated at room temperature for 5 min. Then, 0.2 mL chloroform was added and inverted several times for 15 sec and incubated for 5 min. The samples were centrifuged at 4°C for 15 min at 12,000 g. The clear aqueous phase containing RNA was transferred to a new centrifuge tube. 0.6 mL of isopropanol was added to precipitate mRNA. Samples were incubated at -20°C for 30 min and then centrifuged at 4°C for 10 min. The pellet was gently resuspended in ice cold 75% ethanol and then centrifuged for 5 min at 7,500 g at 4°C. The pellet was dried and resuspended in nuclease-free water (pre-heated to 65°C). RNA was stored at -80°C until use in RT-PCR. A SYBR Green kit was used for quantitative RT-PCR.

### 6.17 Generation of *Rho*<sup>Opn1MW</sup> knock-in mice (Chapter 3)

In experiments not discussed in this thesis, we have begun to investigate the thermal isomerization rate of the mouse middle-wavelength-sensitive cone pigment (*mOpn1MW*). To express this pigment in mouse rods, I generated a knock-in mouse line making use of rhodopsin's promoter to drive expression of *mOpn1MW*. *Rho*<sup>mOpn1MW</sup> mice were generated using the CRISPR/Cas method of targeted genetic editing. A linear double-stranded DNA construct (1,491 bp) was inserted immediately upstream of the start codon of rhodopsin to make use of the endogenous 5' untranslated region (5' UTR) and promoter for driving rod-



specific expression of *Opn1MW* complementary DNA (cDNA). The targeting construct included i) Homology arms (35 bp each) in the 5' UTR and in Exon 1 of the rhodopsin locus ii) a chimeric intron from a mammalian expression vector, pRK5, with the goal of enhancing expression (157) ii) a short spacer sequence downstream of the intron iii) the cDNA for middle-wavelength-sensitive mouse cone pigment (*mOpn1MW*) iv) the 3' UTR from mouse *Opn1MW* (107 bp) and v) a stop codon replacing rhodopsin's endogenous start codon. Following a recently reported alteration of the CRISPR/Cas method (158), we used a single-guide RNA (sgRNA) targeting a 20-bp sequence near rhodopsin's start codon (5' – GGG GCC CTC TGT GCC GTT CA - 3') adjacent to protospacer adjacent motif (PAM, 5' - TGG - 3'). The targeting construct was synthesized as a gBlock (IDT; Coralville, Iowa) and the sgRNA was commercially synthesized (Dharmacon; Lafayette, CO). The sgRNA, the targeting construct, and Cas9 were injected into the pronuclei of *Rho*<sup>REY/WT</sup>;*Gcaps*<sup>+/-</sup> embryos from mating B6SJL females with *Rho*<sup>REY/REY</sup>;*Gcaps*<sup>-/-</sup> males. Injections were carried out at the Transgenic Core Laboratory of Johns Hopkins University School of Medicine. Correct insertion of the construct was verified by DNA sequencing of genomic DNA isolated from tails. Animals with the *mOpn1MW* insertion were identified by genotyping PCR. The line was backcrossed for several generations with *Rho*<sup>REY/REY</sup>;*Gcaps*<sup>-/-</sup> mice to remove any nonspecific CRISPR/Cas-mediated mutations and ultimately to obtain *Rho*<sup>*mOpn1MW*/REY</sup>;*Gcaps*<sup>-/-</sup> mice.

## 6.18 Mouse retina

The mouse retina is ideal for biophysical studies of rod phototransduction due to numerous genetically-engineered lines (See **List of mouse lines**), the rod-dominant retina

[(~400,000 mm<sup>-2</sup>,  $6.4 \times 10^6$  rods per retina, and 97% of photoreceptors (159)], and the robust nature of the isolated retina—used successfully for many hours after dissection (typically up to 6 hrs). Mice were raised under 14 hr:10 hr light:dark cycle in a Johns Hopkins University animal facility and dark-adapted overnight for suction-pipette recording experiments. We used both male and female mice that were 1-3 months old. The following mouse lines were used for experiments in certain chapters, but may not have been needed for the final set of figures.

### 6.19 List of mouse lines (Chapters 2, 3)

Mouse Line	Source	Brief description	Chapter
<i>C57BL/6J</i>	Jackson Labs	Wild type control	2,3
<i>Gcaps<sup>-/-</sup></i>	J. Chen	Helps detect small responses by removing a major negative feedback in phototransduction	2,3
<i>Gnat1<sup>-/-</sup></i>	J. Lem	Rod transducin alpha knockout	2,3
<i>Gnat1<sup>Tg-rTr</sup></i>	J. Chen	Bred with <i>Gnat1<sup>-/-</sup></i> , expresses G <sub>T</sub> α at 6.8% of WT in rods.	2
<i>Rho<sup>REY/REY</sup></i>	K-W. Yau	Substantially weakens the efficiency of rhodopsin's signaling to G <sub>T</sub> α	2,3
<i>Rho<sup>D190N/REY</sup></i>	K-W. Yau	Isolates responses and dark noise from D190N-Rho	3
<i>Rho<sup>mOpn1MW/REY</sup></i>	K-W. Yau	Isolates responses and dark noise from mouse middle-wavelength sensitive cone pigment expressed in rods	3
<i>Gnat1<sup>Tg-55</sup></i>	Y. Fu	Overexpresses G <sub>T</sub> α in rods	2
<i>Gnat1<sup>Tg-57</sup></i>	Y. Fu	Bred with <i>Gnat1<sup>-/-</sup></i> , expresses G <sub>T</sub> α at various amounts in rods across the retina.	2
<i>Rgs9<sup>-/-</sup></i>	C-K. J. Chen	Substantially slows the shutoff of G <sub>T</sub> α*	2

<i>Grk1</i> <sup>+/-</sup>	J. Chen	Substantially slows the shutoff of Rho*	2
<i>Pde6b</i> <sup>rd1/WT</sup>	Spontaneous	Truncated PDE6 $\beta$ causing rapid retinal degeneration	3
<i>Crb1</i> <sup>rd8/WT</sup>	Spontaneous	Frameshift mutation in Crb1, resulting in focal degeneration and shortened outer segments	3

## 6.20 Retinae from other vertebrates (Chapters 4, 5)

Many aspects of photoreceptor physiology are conserved across the animal kingdom such as the major rod- and cone-specific phototransduction components (94, 130, 131, 160–162). However, there are differences in the size, shape, and certain biophysical properties in different animals (40).

Goldfish cones (Fig. 6-5a), for example, are larger and more abundant [ $\sim$ 10-20% of photoreceptors, (35)] than mouse cones [ $\sim$ 3% of photoreceptors, (159)], allowing for their isolation from the retina for solution-exchange experiments. Also, having long-wavelength ( $\lambda_{max} = 620$  nm), middle-wavelength ( $\lambda_{max} = 540$  nm), short-wavelength-sensitive ( $\lambda_{max} = 450$  nm) and UV-sensitive ( $\lambda_{max} = 360$  nm) cone opsins, goldfish retinae provide the opportunity to study dark noise and phototransduction from multiple cone types.

In the vast majority of animals, rods express a pigment with biophysical properties similar to bovine rhodopsin and cones express a cone-specific pigment with properties distinct from rhodopsin. The characteristics of each pigment type influence the visual functions executed by each cell type. In some amphibians, a small subpopulation of rods (1.6%) express a short-wavelength-sensitive ( $\lambda_{max} = 430$  nm) cone pigment instead of rhodopsin. While this is unusual, the majority of rods in all other vertebrates express a

typical rhodopsin. Alligators (*A. mississippiensis*) have only a single rod pigment (Fig. 6-5b). Interestingly, this rod pigment ( $\lambda_{max} = 503$  nm) has cone pigment properties, but still supports rod-mediated vision with high sensitivity and slow kinetics. Thus, there are many questions in phototransduction that require the study of non-model organisms.

#### **6.21 Suction-pipette recordings from goldfish cones (Chapter 4)**

Goldfish (*Carassius auratus*) were raised in an indoor aquarium with a 12/12 light cycle, dark-adapted overnight before an experiment and euthanized immediately before recording. The eyes were removed and hemisected under infrared light. Eyecups were stored in fish Ringer's solution (130-mM NaCl, 2.6-mM KCl, 1-mM MgCl<sub>2</sub>, 1-mM CaCl<sub>2</sub>, 10-mM glucose, 10-mM HEPES (pH 7.8), 0.02-mM EDTA). For recording, a piece of tissue was cut from the retina, chopped, and transferred to the recording chamber perfused with fish Ringer's at room temperature.

Suction pipette recordings were conducted as described above. Briefly, guided with an infrared-sensitive camera, the outer segment of an isolated single cone was drawn into a tight-fitting glass pipette coated with tri-*n*-butylchlorosilane (Pfaltz and Bauer Inc., Waterbury, CT) and filled with fish Ringer's solution (Fig. 6-5a). Membrane current was measured with a patch clamp amplifier (Axopatch 200B; Axon Instruments). Signals were low-pass filtered at 20 Hz (RC filter, Krohn-height model 3343) and sampled at 500 Hz. All experiments were performed at ~23°C.

## 6.22 Truncated-cone recordings (Chapter 4)

In brief, conventional suction pipette recording was first made, and then converted to truncated cone recording as follows. A glass probe was brought close to the recorded cone. A lateral stroke of the glass probe sheared off the inner segment and cell body of the recorded cone. As a result, an open-ended outer segment was obtained. Occasionally, a second stroke is needed when the first trial failed. The open end of the outer segment was brought close to the outlet of perfusion tubing that was connected to multiple solution reservoirs. Solenoid Valve (Lee Company) and ValveLink 8 (AutoMate Scientific, Inc.) control switch between solutions.

The recording electrode was filled with: 130-mM NaCl, 0.05-mM CaCl<sub>2</sub>, 1-mM MgCl<sub>2</sub>, 10-mM HEPES (pH 7.8), 1-mM EGTA, and 10-mM D-glucose, with the calculated free [Ca<sup>2+</sup>] of 0.75 nM. The composition of the pseudointracellular (bath) solution is: (in mM) 135-mM L-Arginine, 135-mM L-Glutamate Acid, 1 MgCl<sub>2</sub>-mM, 0.66 CaCl<sub>2</sub>-mM, 10-mM HEPES (pH 7.8), 1-mM BAPTA, with the calculated free [Ca<sup>2+</sup>] concentration of 390-nM. GTP-Mg<sup>2+</sup>, ATP-Mg<sup>2+</sup> and cGMP-Na<sup>+</sup> were dissolved in water and freshly prepared. IBMX was dissolved in DMSO. The final concentrations of ATP, GTP and IBMX were obtained after dilution with the pseudointracellular solution.

## 6.23 Cell identification, light stimuli (Chapter 4)

In goldfish, there are single cones and double cones. Single cones consist of red, green, blue, and UV cones, whereas double cones typically consist of one red and one green cone (35). Identifications of cone types are based on their spectral sensitivity: red, green,

blue, and UV cones are most sensitive to wavelengths of 620, 537, 447, and 360 nm, respectively.

Cones were stimulated with calibrated 10-ms flashes at their optimal monochromatic wavelengths. Dim-flash responses were averaged from 40-60 repeated trials; bright flash responses from 10-20 repeated trials.

#### 6.24 Quantitative analysis of truncated-cone recordings (Chapter 4)

The dissipation of cGMP results from two factors: i) diffusion out of the outer segment and ii) PDE-catalyzed hydrolysis in the outer segment. As the cGMP concentration falls below the Michaelis constant of PDE,  $K_m$  [ $\sim 100 \mu\text{M}$ , (6)], the cGMP hydrolysis becomes a first-order reaction with rate constant  $\beta'$ , where  $\beta' = V_{max}/K_m$ , where  $V_{max}$  is the maximum “intrinsic” enzymatic activity (i.e. independent of  $G_T$ -mediated activation). Likewise, the rate of cGMP diffusion is a first-order process with rate constant  $\gamma$  dictated by cGMP’s diffusion coefficient (125). Thus, cGMP in the outer segment should have a final exponential decay with rate constant  $(\beta' + \gamma)$ . As the cGMP concentration falls far below the half-activation constant,  $K_{1/2}$ , for the dose-response relation of the cGMP-gated channel, the inward cGMP-gated current will also decay exponentially with a rate constant of  $n_H(\beta' + \gamma)$ , where  $n_H$  is the Hill coefficient for channel activation by cGMP. The parameter  $\gamma$  can be independently measured by repeating the above experimental procedure with 1-mM IBMX, an inhibitor of PDE, in the bath solution, thus making  $\beta' = 0$ . From the difference in rate constant of current decline between the absence and presence of IBMX,  $\beta'$  can be evaluated by taking  $n_H = 2.4$  (163).

### **6.25 Weber-Fechner relation in goldfish cones (Chapter 4)**

The Weber-Fechner relation is  $S_F/S_F^D = I_o/(I_B+I_o)$  where  $S_F^D$  is flash sensitivity in darkness,  $S_F$  is flash sensitivity in background light of intensity  $I_B$ , and  $I_o$  is the background intensity that halves the sensitivity. This relation fits the fold-change in flash sensitivity of a rod or a cone as it adapts to steady light.

### **6.26 Application of 11-*cis*-retinal A1 and 11-*cis*-retinal A2 to goldfish cones during a suction-pipette recordings (Chapter 4)**

11-*cis*-retinal was applied to goldfish cones during a suction-pipette recording experiment with the outer segment drawn into the pipette. To avoid adsorption of the hydrophobic chromophore to plastic, we used stainless steel tubing and a custom-fabricated stainless-steel recording chamber. The chromophore was held in a glass syringe reservoir in darkness on the microscope stage until needed. To apply chromophore, a 3-way valve was switched into a position that would allow chromophore in fish Ringer's solution to flow into the chamber.

### **6.27 Suction-pipette recordings from alligator rods (Chapter 5)**

Alligators (*A. mississippiensis*, 1-yr-old) were imported from the Rockefeller Wildlife Refuge (Louisiana Wildlife and Fisheries) to Johns Hopkins University and were housed in a tank with a water reservoir equipped and with overhead ceramic heaters to maintain a ground temperature of 27-32°C. For experiments, an animal was dark-adapted overnight, euthanized, and eyes were hemisected for storing eyecups over several hours. A piece of retina was cut from the eye cup, chopped, and transferred to the recording

chamber perfused with alligator Ames' solution (Ames' medium, A1420, Sigma-Aldrich with added 20-mM NaCl, 3-mM KCl, bubbled with 95% O<sub>2</sub> / 5% CO<sub>2</sub>). An alligator rod outer segment was drawn into a tightly-fitting glass pipette filled with pipette solution (Fig 6-5b). The single-photon response was analyzed from a series of dim-flash responses and dark noise was measured to evaluate the rate of discrete events produced by alligator rhodopsin.

### **6.28 Microspectrophotometry measurements from alligator rods (Chapter 5)**

To evaluate accessibility of alligator rhodopsin's chromophore-binding pocket, we evaluated chromophore exchange in alligator rods using microspectrophotometry. Dark-adapted alligator eyes were isolated at Johns Hopkins University as described above and punctured to facilitate storage solution access to the retina. Acutely isolated eyes were stored on ice in pre-oxygenated HEPES-buffered alligator Ames', pH 7.4 and shipped overnight to Boston University for analysis by Rikard Frederiksen in the laboratory of Carter Cornwall. Microspectrophotometry measurements were made in alligator Ames' solution. Alligator rhodopsin reconstituted with 9-*cis*-retinal has  $\lambda_{max} = 485$  nm, whereas endogenous alligator rhodopsin bound by 11-*cis*-retinal has  $\lambda_{max} = 503$  nm. Thus, the extent of chromophore exchange can be measured by following the gradual blue-shift in a rod's absorbance spectrum during exposure to 9-*cis*-retinal. Three retinal samples were compared: i) dark-adapted control rods, ii) dark-adapted rods exposed to 9-*cis*-retinal for 6 hours, and iii) bleached alligator rods (exposed to enough light to bleach >99% of each rod's rhodopsin content) subsequently regenerated with 9-*cis*-retinal.



## **6.29 Animal care and use (Chapters 2, 3, 4, 5)**

All animal experiments were conducted according to protocols approved by the Institutional Animal Care and Use Committee at Johns Hopkins University.

### 6.30 Figures

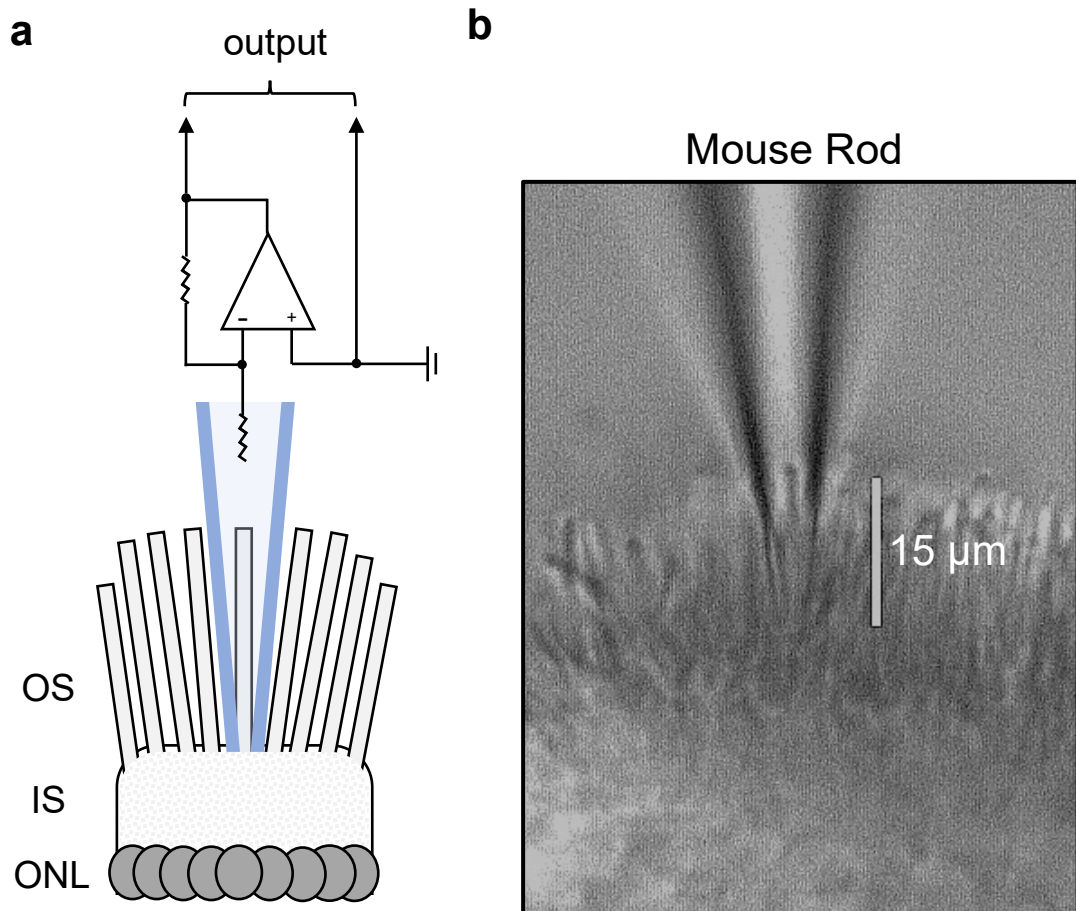


**Figure 6-1. Suction-pipette Recording.** **a**, Schematic diagram illustrating the recording configuration used for recording membrane current from a photoreceptor outer segment (OS) protruding from the cell's inner segment (IS). The photoreceptor cell body can be seen in the outer-nuclear layer (ONL) in a section of the retina. A tightly-fitting glass electrode filled with solution is shown in blue, which records current using a patch-clamp amplifier. **b**, Photomicrograph of a mouse retinal rod drawn into a suction-pipette during an experiment. The retina is illuminated by infrared light (>850 nm) and imaged using an infrared image converter.

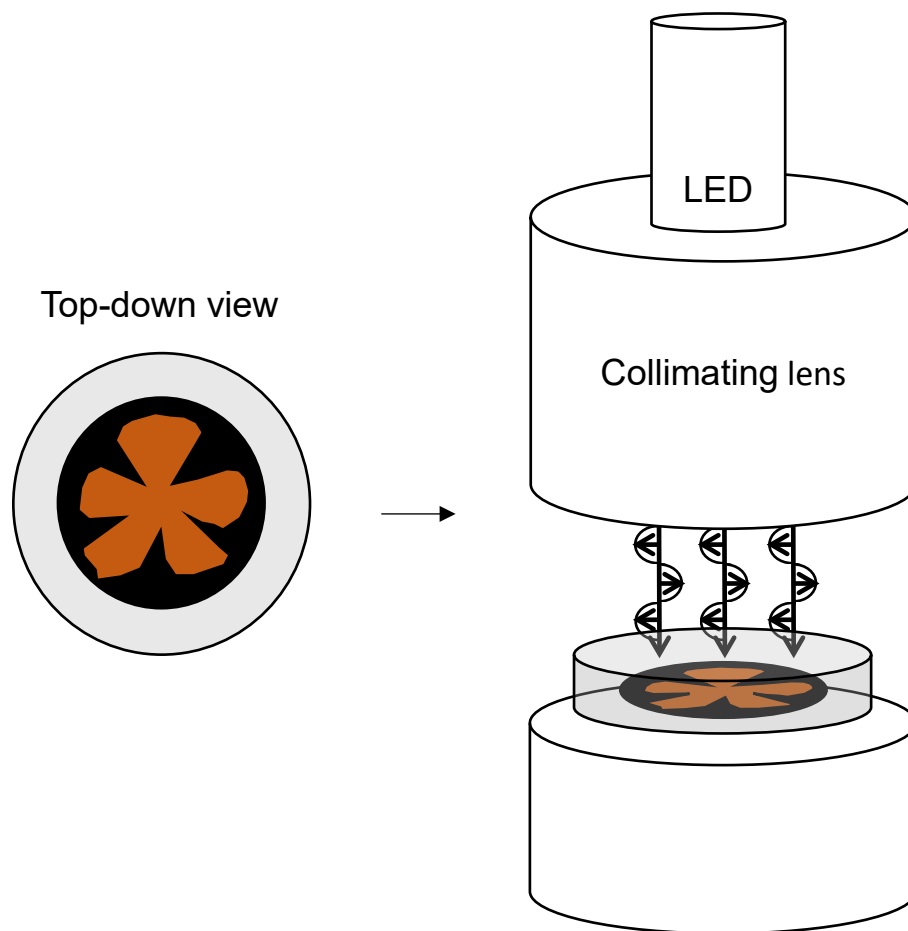


**Figure 6-2. Bleaching to produce apo-opsin in rods.** To carefully control the amount of bleaching light, a mouse retina was flat-mounted on a piece of black filter paper (left). The retina was then exposed to a calibrated light pulse of collimated light to ensure approximately uniform bleaching. A square piece of retina ( $\sim 1$  to  $2 \text{ mm}^2$ ) was cut from the center of the retina where rods were densely packed and commonly pointing upward to further ensure a uniformly-bleached population.

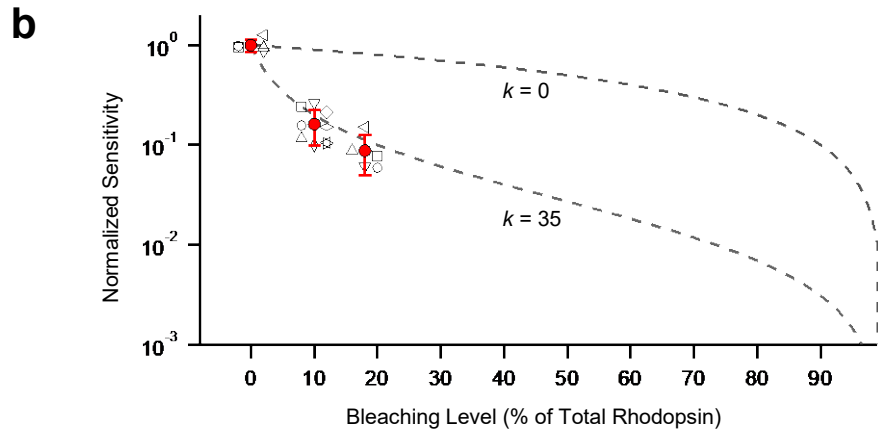
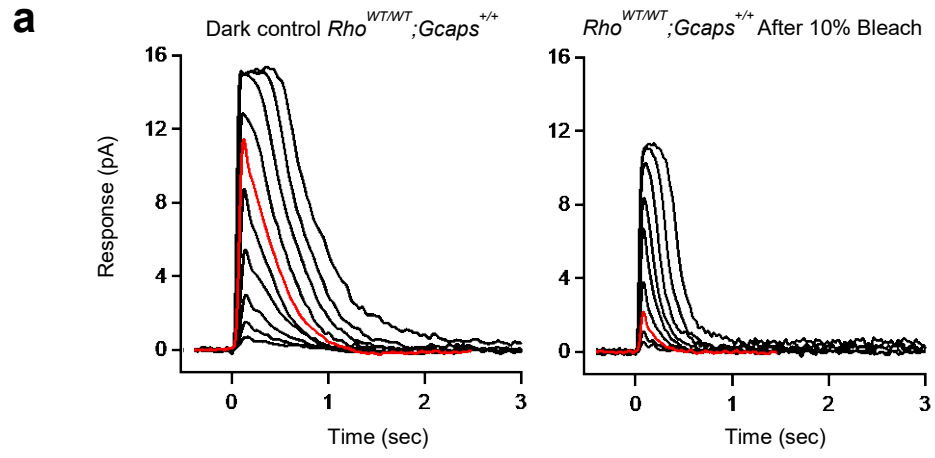


**Figure 6-3. Validation of bleaching procedures and calculations.** **a**, Responses of  $Rho^{WT/WT};Gcap^{+/+}$  rods to various flash strengths in dark-adapted conditions (left) or >60 min after a 10% bleach (right). Responses to the same flash strength are highlighted in red for comparison. **b**, Fold-change in photosensitivity after bleaching 10% and 20% of rhodopsin in  $Rho^{WT/WT};Gcap^{+/+}$  rods, measured from the half-saturating flash strength ( $\sigma$ ) and fit approximately by the relation  $\Delta S = (1-B)/(1+kB)$  where  $\Delta S$  is the fold-change in photosensitivity,  $B$  is the fractional bleach determined by our axial bleaching equation, and  $k$  is a constant related to the amount of bleaching adaptation produced by Opn\* activity [ $k \approx 35$  in mouse rods, as reported previously from bleaching with transverse illumination (70)]. For comparison, shown also is the expected change in sensitivity from loss of photon capture alone ( $k = 0$ ).

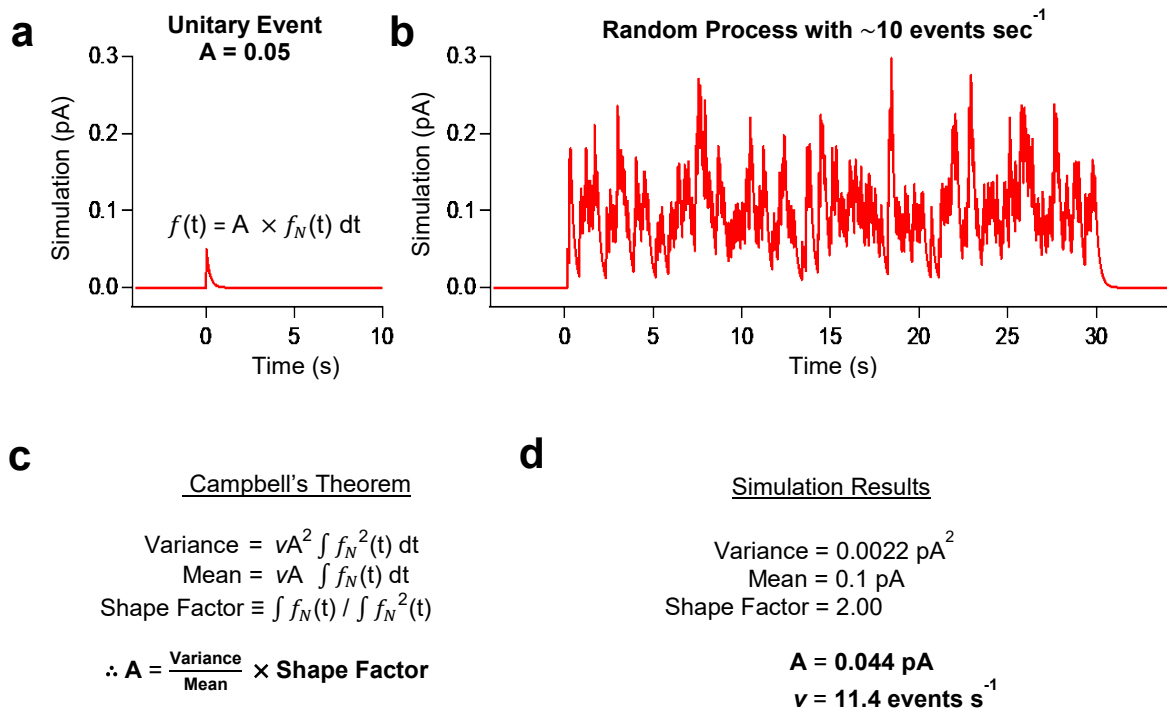


**Figure 6-4. Validation of Campbell's Theorem by Poisson Process Simulation.** **a**, Input unitary event with single-exponential decline waveform and amplitude,  $A = 0.05 \text{ pA}$ . **b**, Poisson process ( $t = 0$  to  $30 \text{ sec}$ ) generated from inter-event intervals randomly selected from an exponential probability distribution with event frequency,  $\lambda = 10 \text{ events sec}^{-1}$ . **c**, Campbell's theorem as applied to our post-bleach noise analysis for calculating  $A$  from noise variance, mean, and shape factor. **d**, Estimates of unitary event amplitude ( $A = 0.044 \text{ pA}$ ) and of event frequency ( $v = 11.4 \text{ events sec}^{-1}$ ) from applying Campbell's theorem analysis to the noise generated in panel **b**. Note that the estimates are within 15% of the actual input values.

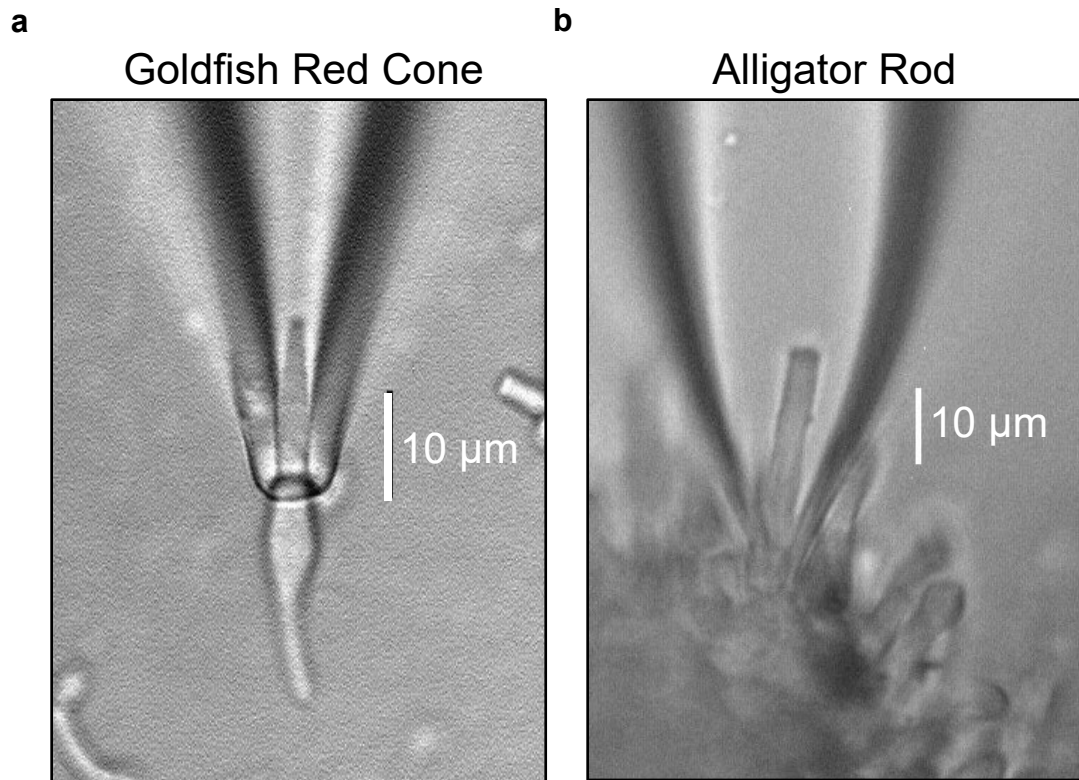


**Figure 6-5. Suction-pipette recording from various animals. a,** Red-sensitive cone ( $\lambda_{\text{max}} = 620 \text{ nm}$ ) isolated from a goldfish retina, with outer segment drawn into a pipette for recording. **b,** Suction-pipette recording with an alligator rod protruding from a piece of retina acutely isolated from an alligator.

## References

1. Luo D-G, Yue WWS, Ala-Laurila P, Yau K-W (2011) Activation of visual pigments by light and heat. *Science* 332(6035):1307–12.
2. Sung CH, et al. (1991) Rhodopsin mutations in autosomal dominant retinitis pigmentosa. *Proc Natl Acad Sci U S A* 88(15):6481–6485.
3. Sung CH, Schneider BG, Agarwal N, Papermaster DS, Nathans J (1991) Functional heterogeneity of mutant rhodopsins responsible for autosomal dominant retinitis pigmentosa. *Proc Natl Acad Sci U S A* 88(19):8840–4.
4. Nathans J (1994) In the eye of the beholder: visual pigments and inherited variation in human vision. *Cell* 78(3):357–60.
5. Vuong TM, Chabre M, Stryer L (1984) Millisecond activation of transducin in the cyclic nucleotide cascade of vision. *Nature* 311(5987):659–661.
6. Leskov IB, et al. (2000) The gain of rod phototransduction: reconciliation of biochemical and electrophysiological measurements. *Neuron* 27(3):525–537.
7. Krispel CM, et al. (2006) RGS expression rate-limits recovery of rod photoresponses. *Neuron* 51(4):409–416.
8. Doan T, Azevedo AW, Hurley JB, Rieke F (2009) Arrestin competition influences the kinetics and variability of the single-photon responses of mammalian rod photoreceptors. *J Neurosci* 29(38):11867–11879.
9. Lamb TD, Kraft TW (2016) Quantitative modeling of the molecular steps underlying shut-off of rhodopsin activity in rod phototransduction. *Mol Vis* 22(March):674–696.
10. Hecht S, Schlaer S, Pirenne MH (1942) Energy, quanta and vision. *J Gen Physiol* 25(6):819–840.
11. Baylor DA, Matthews G, Yau KW (1980) Two components of electrical dark noise in toad retinal rod outer segments. *J Physiol* 309(1):591–621.
12. RetNet (2018) RetNet: Genes and Mapped Loci Causing Retinal Diseases. Available at: <https://sph.uth.edu/retnet/disease.htm#03.202d>.
13. Janz JM, Fay JF, Farrens DL (2003) Stability of dark state rhodopsin is mediated by a conserved ion pair in intradiscal loop E-2. *J Biol Chem* 278(19):16982–16991.
14. Liu MY, et al. (2013) Thermal stability of rhodopsin and progression of retinitis pigmentosa: comparison of S186W and D190N rhodopsin mutants. *J Biol Chem* 288(24):17698–17712.
15. Barlow HB (1956) Retinal noise and absolute threshold. *J Opt Soc Am* 46(8):634–639.



16. Donner K (1992) Noise and the absolute thresholds of cone and rod vision. *Vision Res* 32(5):853–66.
17. Kefalov V, Fu Y, Marsh-Armstrong N, Yau K-W (2003) Role of visual pigment properties in rod and cone phototransduction. *Nature* 425(6957):526–531.
18. Fu Y, Kefalov V, Luo D-G, Xue T, Yau K-W (2008) Quantal noise from human red cone pigment. *Nat Neurosci* 11(5):565–571.
19. Rieke F, Baylor DA (2000) Origin and functional impact of dark noise in retinal cones. *Neuron* 26(1):181–186.
20. Matsumoto H, Tokunaga F, Yoshizawa T (1975) Accessibility of the iodopsin chromophore. *Biochim Biophys Acta - Gen Subj* 404(2):300–308.
21. Kefalov VJ, et al. (2005) Breaking the covalent bond — a pigment property that contributes to desensitization in cones. *Neuron* 46(6):879–890.
22. Imamoto Y, Shichida Y (2014) Cone visual pigments. *Biochim Biophys Acta - Bioenerg* 1837(5):664–673.
23. Kefalov VJ (2012) Rod and Cone Visual Pigments and Phototransduction through Pharmacological, Genetic, and Physiological Approaches. *J Biol Chem* 287(3):1635–1641.
24. Luo D-G, Kefalov V, Yau K-W (2008) 1.10 - Phototransduction in Rods and Cones. *The Senses: A Comprehensive Reference*, eds Masland RH, et al. (Academic Press, New York), pp 269–301.
25. Wald G, Brown PK, Kennedy D (1957) The visual system of the alligator. *J Gen Physiol* 40(5):703–713.
26. Crescitelli F (1988) The gecko visual pigment: the chromophore dark exchange reaction. *Exp Eye Res* 46(2):239–48.
27. Kojima D, et al. (1992) Cone visual pigments are present in gecko rod cells. *Proc Natl Acad Sci* 89(15):6841–6845.
28. Bringmann A, et al. (2018) The primate fovea: Structure, function and development. *Prog Retin Eye Res* 66:49–84.
29. Sinha R, et al. (2017) Cellular and Circuit Mechanisms Shaping the Perceptual Properties of the Primate Fovea. *Cell* 168(3):413–426.e12.
30. Bhandawat V, Reiser J, Yau K-W (2005) Elementary response of olfactory receptor neurons to odorants. *Science* 308(5730):1931–1934.
31. Schäfer E. A. and Thane G. D. (1894) *Organs of the Senses. Quain's Elements of Anatomy.*
32. Sung C-H, Chuang J-Z (2010) The cell biology of vision. *J Cell Biol* 190(6):953–963.
33. Daiger S. P., Browne S. J. SLS (2015) *Genes and Mutations Causing Autosomal*

- Dominant Retinitis Pigmentosa. *Retinal Disorders, Genetic Approaches to Diagnosis and Treatment* (Cold Spring Harbor Perspectives in Medicine), pp 27–39.
34. Lythgoe JN (1972) List of Vertebrate Visual Pigments. *Handbook of Sensory Physiology* (Springer-Verlag, New York), pp 604–624. VII/1.
  35. Stell WK, Hárosi FI (1976) Cone structure and visual pigment content in the retina of the goldfish. *Vision Res* 16(6):647–57.
  36. Sun H, Macke JP, Nathans J (1997) Mechanisms of spectral tuning in the mouse green cone pigment. *Proc Natl Acad Sci U S A* 94(16):8860–5.
  37. Hárosi FI (1975) Absorption Spectra and Linear Dichroism of Some Amphibian Photoreceptors. *J Physiol* 66:357–382.
  38. Hárosi FI, MacNichol EF (1974) Visual pigments of goldfish cones. Spectral properties and dichroism. *J Gen Physiol* 63(3):279–304.
  39. Yau KW, Hardie RC (2009) Phototransduction Motifs and Variations. *Cell* 139(2008):246–264.
  40. Schultz M. (1866) Zur Anatomie und Physiologie der Retina. *Archiv Fur Mikroskopische Anatomie*, pp 175–286.
  41. Pugh EN, Lamb TD (1993) Amplification and kinetics of the activation steps in phototransduction. *Biochim Biophys Acta* 1141(2–3):111–149.
  42. Arshavsky VY, Lamb TD, Pugh EN (2002) G proteins and phototransduction. *Annu Rev Physiol* 64:153–187.
  43. Arshavsky VY, Burns ME (2014) Current understanding of signal amplification in phototransduction. *Cell Logist* 4(May):e29390.
  44. Fung BK, Stryer L (1980) Photolyzed rhodopsin catalyzes the exchange of GTP for bound GDP in retinal rod outer segments. *Proc Natl Acad Sci U S A* 77(5):2500–2504.
  45. Fung BK, Hurley JB, Stryer L (1981) Flow of information in the light-triggered cyclic nucleotide cascade of vision. *Biochemistry* 78(1):152–156.
  46. Liebman PA, Pugh EN (1982) Gain, speed and sensitivity of GTP binding vs PDE activation in visual excitation. *Vision Res* 22(12):1475–1480.
  47. Robinson PR, Radeke MJ, Cote RH, Bownds MD (1986) cGMP influences guanine nucleotide binding to frog photoreceptor G-protein. *J Biol Chem* 261(1):313–318.
  48. Gray-Keller MP, Biernbaum MS, Bownds MD (1990) Transducin activation in electroporated frog rod outer segments is highly amplified, and a portion equivalent to phosphodiesterase remains membrane-bound. *J Biol Chem* 265(25):15323–15332.

49. Yee R, Liebman PA (1978) Light-activated Phosphodiesterase of the Rod Outer Segment. *J Biol Chem* 253(24):8902–8909.
50. Wagner R, Ryba N, Uhl R (1988) Sub-second turnover of transducin GTPase in bovine rod outer segments. A light scattering study. *FEBS Lett* 234(1):44–48.
51. Kahlert M, Hofmann KP (1991) Reaction rate and collisional efficiency of the rhodopsin-transducin system in intact retinal rods. *Biophys J* 59(2):375–386.
52. Heck M, Hofmann KP (2001) Maximal rate and nucleotide dependence of rhodopsin-catalyzed transducin activation: initial rate analysis based on a double displacement mechanism. *J Biol Chem* 276(13):10000–9.
53. Pepperberg DR, Kahlert M, Krause A, Hofmann KP (1988) Photoc modulation of a highly sensitive, near-infrared light-scattering signal recorded from intact retinal photoreceptors. *Proc Natl Acad Sci U S A* 85(15):5531–5535.
54. Gross OP, Burns ME (2010) Control of rhodopsin’s active lifetime by arrestin-1 expression in mammalian rods. *J Neurosci* 30(9):3450–3457.
55. Chen C-K, et al. (2012) Modulation of mouse rod response decay by rhodopsin kinase and recoverin. *J Neurosci* 32(45):15998–16006.
56. Rieke F, Baylor DA (1998) Origin of reproducibility in the responses of retinal rods to single photons. *Biophys J* 75(4):1836–1857.
57. Hamer RD, Nicholas SC, Tranchina D, Liebman PA, Lamb TD (2003) Multiple Steps of Phosphorylation of Activated Rhodopsin Can Account for the Reproducibility of Vertebrate Rod Single-photon Responses. *J Gen Physiol* 122(4):419–444.
58. Lamb TD, Heck M, Kraft TW (2018) Implications of dimeric activation of PDE6 for rod phototransduction. *Open Biol* 8(8):180076.
59. Baylor DA, Lamb TD, Yau K-W (1979) Responses of retinal rods to single photons. *J Physiol* 288:613–634.
60. Leskov IB, et al. (2000) The gain of rod phototransduction: reconciliation of biochemical and electrophysiological measurements. *Neuron* 27(3):525–537.
61. Alberts B, et al. (2015) Second messengers and enzymatic cascades amplify signals. *Molecular Biology of the Cell* (Garland Science, New York), p 869. 6th Ed.
62. Kandel, E.R.; Schwartz J.H.; Jessel T.M.; Siegelbaum S.A.; Hudspeth AJ (2012) Low-level Visual Processing: The Retina. *Principles of Neural Science* (McGraw-Hill Education), p 583. 5th Ed.
63. Nicholls, J.G.; Martin, A.R.; Wallace BG (2011) Transduction and Transmission in the Retina. *From Neuron to Brain* (Sinauer Associates, Inc.), p 417. 5th Ed.
64. Purves D, et al. (2011) Amplification in signal transduction pathways. *Neuroscience* (Sinauer Associates, Inc., Sunderland (MA)), p 143. 5th Ed.

65. Lesk A (2016) G proteins and G-protein-coupled receptors. *Introduction to Protein Science: Architecture, Function, and Genomics* (Oxford University Press Inc., New York), p 84. 3rd Ed.
66. Cornwall MC, Fain GL (1994) Bleached pigment activates transduction in isolated rods of the salamander retina. *J Physiol* 480(Pt2):261–279.
67. Franke RR, König B, Sakmar TP, Khorana HG, Hofmann KP (1990) Rhodopsin mutants that bind but fail to activate transducin. *Science* 250(4977):123–125.
68. Sakmar TP, Franke RR, Khorana HG (1989) Glutamic acid-113 serves as the retinylidene Schiff base counterion in bovine rhodopsin. *Proc Natl Acad Sci* 86(21):8309–8313.
69. Melia TJ, Cowan CW, Angleson JK, Wensel TG (1997) A comparison of the efficiency of G protein activation by ligand-free and light-activated forms of rhodopsin. *Biophys J* 73(6):3182–3191.
70. Nymark S, Frederiksen R, Woodruff ML, Cornwall MC, Fain GL (2012) Bleaching of mouse rods: microspectrophotometry and suction-electrode recording. *J Physiol* 590(10):2353–2364.
71. Mendez A, et al. (2001) Role of guanylate cyclase-activating proteins (GCAPs) in setting the flash sensitivity of rod photoreceptors. *Proc Natl Acad Sci* 98(17):9948–9953.
72. Rieke F, Baylor DA (1996) Molecular origin of continuous dark noise in rod photoreceptors. *Biophys J* 71(5):2553–2572.
73. Lamb TD (1980) Spontaneous quantal events induced in toad rods by pigment bleaching. *Nature* 287(5780):349–51.
74. Leibrock CS, Lamb TD (1997) Effect of hydroxylamine on photon-like events during dark adaptation in toad rod photoreceptors. *J Physiol* 501 ( Pt 1):97–109.
75. Luo D-G, Yau K-W (2005) Rod sensitivity of neonatal mouse and rat. *J Gen Physiol* 126(3):263–269.
76. Xiong W-H, Yau K-W (2002) Rod Sensitivity During *Xenopus* Development. *J Gen Physiol* 120(6):817–827.
77. Tian H, Sakmar TP, Huber T (2017) Measurement of slow spontaneous release of 11-cis-retinal from rhodopsin. *Biophys J* 112(1):153–161.
78. Rice SO (1944) Mathematical Analysis of Random Noise. *Bell Syst Tech J*. doi:10.1002/j.1538-7305.1944.tb00874.x.
79. Katz B, Miledi R (1972) The statistical nature of the acetylcholine potential and its molecular components. *J Physiol* 224(3):665–99.
80. Burns ME, Mendez A, Chen J, Baylor DA (2002) Dynamics of cyclic GMP synthesis in retinal rods. *Neuron* 36(1):81–91.

81. Berry J, et al. (2016) Effect of Rhodopsin Phosphorylation on Dark Adaptation in Mouse Rods. *J Neurosci* 36(26):6973–6987.
82. Strissel KJ, Sokolov M, Trieu LH, Arshavsky VY (2006) Arrestin Translocation Is Induced at a Critical Threshold of Visual Signaling and Is Superstoichiometric to Bleached Rhodopsin. *J Neurosci* 26(4):1146–1153.
83. Sokolov M, et al. (2002) Massive light-driven translocation of transducin between the two major compartments of rod cells: a novel mechanism of light adaptation. *Neuron* 34(1):95–106.
84. Okawa H, et al. (2010) Optimal processing of photoreceptor signals is required to maximize behavioural sensitivity. *J Physiol* 588(11):1947–1960.
85. Gross OP, Pugh EN, Burns ME (2012) Calcium feedback to cGMP synthesis strongly attenuates single-photon responses driven by long rhodopsin lifetimes. *Neuron* 76(2):370–382.
86. Chen C-KK, et al. (1999) Abnormal photoresponses and light-induced apoptosis in rods lacking rhodopsin kinase. *Proc Natl Acad Sci U S A* 96(7):3718–3722.
87. Calvert PD, et al. (2000) Phototransduction in transgenic mice after targeted deletion of the rod transducin alpha -subunit. *Proc Natl Acad Sci U S A* 97(25):13913–13918.
88. Jones Brunette AM, Sinha A, David L, Farrens DL (2016) Evidence that the rhodopsin kinase (GRK1) N-terminus and the transducin  $G\alpha$  C-terminus interact with the same “hydrophobic patch” on rhodopsin TM5. *Biochemistry* 55(22):3123–3135.
89. Kang Y, et al. (2015) Crystal structure of rhodopsin bound to arrestin by femtosecond X-ray laser. *Nature* 523(7562):561–567.
90. Palczewski K, Buczyłko J, Kaplan MW, Polans AS, Crabb JW (1991) Mechanism of rhodopsin kinase activation. *J Biol Chem* 266(20):12949–12955.
91. Szczeppek M, et al. (2014) Crystal structure of a common GPCR-binding interface for G protein and arrestin. *Nat Commun* 5(May):4801.
92. Melia TJ, Malinski JA, He F, Wensel TG (2000) Enhancement of phototransduction protein interactions by lipid surfaces. *J Biol Chem* 275(5):3535–42.
93. Wensel TG, Stryer L (1990) Activation mechanism of retinal rod cyclic GMP phosphodiesterase probed by fluorescein-labeled inhibitory subunit. *Biochemistry* 29(8):2155–2161.
94. Muradov H, Boyd KK, Artemyev NO (2010) Rod phosphodiesterase-6 PDE6A and PDE6B subunits are enzymatically equivalent. *J Biol Chem* 285(51):39828–39834.
95. Qureshi BM, et al. (2018) It takes two transducins to activate the cGMP-

- phosphodiesterase 6 in retinal rods. *Open Biol* 8(8):180075.
96. Bennett N, Clerc A (1989) Activation of cGMP phosphodiesterase in retinal rods: mechanism of interaction with the GTP-binding protein (transducin). *Biochemistry* 28(18):7418–7424.
  97. Su CY, Menuz K, Carlson JR (2009) Olfactory perception: receptors, cells, and circuits. *Cell* 139(1):45–59.
  98. Tolkovsky AM, Levitzki A (1978) Mode of coupling between the  $\beta$ -adrenergic receptor and adenylate cyclase in turkey erythrocytes. *Biochemistry* 17(18):37953810.
  99. Tolkovsky AM, Braun S, Levitzki A (1982) Kinetics of interaction between beta-receptors, GTP protein, and the catalytic unit of turkey erythrocyte adenylate cyclase. *Proc Natl Acad Sci U S A* 79:213–217.
  100. Pedersen SE, Ross EM (1982) Functional reconstitution of beta-adrenergic receptors and the stimulatory GTP-binding protein of adenylate cyclase. *Proc Natl Acad Sci U S A* 79:7228–7232.
  101. Senogles SE, et al. (1987) The D2-dopamine receptor of anterior pituitary is functionally associated with a pertussis toxin-sensitive guanine nucleotide binding protein. *J Biol Chem* 262(10):4860–4867.
  102. Rushton WA (1965) Visual adaptation. *Proc R Soc London Ser B Biol Sci* 162(986):20–46.
  103. Gross OP, Pugh EN, Burns ME (2015) cGMP in mouse rods: the spatiotemporal dynamics underlying single photon responses. *Front Mol Neurosci* 8(March):6.
  104. Yue WWS, et al. (2017) Spontaneous activation of visual pigments in relation to openness/closedness of chromophore-binding pocket. *Elife* 6. doi:10.7554/eLife.18492.
  105. Hinshelwood CN (1940) *The kinetics of chemical change* (The Clarendon Press, Oxford).
  106. Baylor DA, Nunn BJ, Schnapf JL (1984) The photocurrent, noise and spectral sensitivity of rods of the monkey *Macaca fascicularis*. *J Physiol* 357:575–607.
  107. Wang T, Chen J (2014) Induction of the Unfolded Protein Response by Constitutive G-protein Signaling in Rod Photoreceptor Cells. *J Biol Chem* 289(42):29310–29321.
  108. Sancho-Pelluz J, et al. (2012) Mice with a D190N mutation in the gene encoding rhodopsin: a model for human autosomal-dominant retinitis pigmentosa. *Mol Med* 18(12):549–555.
  109. Lem J, et al. (1999) Morphological, physiological, and biochemical changes in rhodopsin knockout mice. *Proc Natl Acad Sci U S A* 96(2):736–41.
  110. Sieving PA, et al. (2001) Constitutive &quot;light&quot; adaptation in rods from

- G90D rhodopsin: a mechanism for human congenital nightblindness without rod cell loss. *J Neurosci* 21(15):5449–60.
111. Sakami S, et al. (2011) Probing Mechanisms of Photoreceptor Degeneration in a New Mouse Model of the Common Form of Autosomal Dominant Retinitis Pigmentosa due to P23H Opsin Mutations. *J Biol Chem* 286(12):10551–10567.
  112. Sung CH, Makino C, Baylor D, Nathans J (1994) A rhodopsin gene mutation responsible for autosomal dominant retinitis pigmentosa results in a protein that is defective in localization to the photoreceptor outer segment. *J Neurosci* 14(10):5818–33.
  113. Sung CH, Davenport CM, Nathans J (1993) Rhodopsin mutations responsible for autosomal dominant retinitis pigmentosa. Clustering of functional classes along the polypeptide chain. *J Biol Chem* 268(35):26645–9.
  114. Janz JM, Farrens DL (2003) Assessing structural elements that influence Schiff base stability: Mutants E113Q and D190N destabilize rhodopsin through different mechanisms. *Vision Res* 43(28):2991–3002.
  115. Tsui I, Chou CL, Palmer N, Lin CS, Tsang SH (2008) Phenotype-genotype correlations in autosomal dominant retinitis pigmentosa caused by RHO, D190N. *Curr Eye Res* 33(11):1014–1022.
  116. Dartnall HJA (1972) Photosensitivity. *Handbook of Sensory Physiology* (Springer-Verlag, New York), pp 122–145. VII/1.
  117. Hao W, et al. (2002) Evidence for two apoptotic pathways in light-induced retinal degeneration. *Nat Genet* 32(2):254–260.
  118. Athanasiou D, et al. (2017) The role of the ER stress-response protein PERK in rhodopsin retinitis pigmentosa. *Hum Mol Genet* 26(24):4896–4905.
  119. Kroeger H, Chiang W-C, Felden J, Nguyen A, Lin JH (2018) ER stress and unfolded protein response in ocular health and disease. *FEBS J*. doi:10.1111/febs.14522.
  120. Kaushal S, Khorana HG (1994) Structure and function in rhodopsin. 7. Point mutations associated with autosomal dominant retinitis pigmentosa. *Biochemistry* 33(20):6121–6128.
  121. Schnapf JL, Nunn BJ, Meister M, Baylor DA (1990) Visual transduction in cones of the monkey *Macaca fascicularis*. *J Physiol* 427:681–713.
  122. Cao L-H, Luo D-G, Yau K-W (2014) Light responses of primate and other mammalian cones. *Proc Natl Acad Sci U S A* 111(7):2752–7.
  123. Perry RJ, McNaughton PA (1991) Response properties of cones from the retina of the tiger salamander. *J Physiol* 433:561–87.
  124. Palacios AG, Varela FJ, Srivastava R, Goldsmith TH (1998) Spectral sensitivity of cones in the goldfish, *Carassius auratus*. *Vision Res* 38(14):2135–46.

125. Koutalos Y, Nakatani K, Yau KW (1995) Cyclic GMP diffusion coefficient in rod photoreceptor outer segments. *Biophys J* 68(1):373–382.
126. Nakatani K, Yau K-W (1988) Calcium and light adaptation in retinal rods and cones. *Nature* 334(6177):69–71.
127. Pugh EN, Nikonov S, Lamb TD (1999) Molecular mechanisms of vertebrate photoreceptor light adaptation. *Curr Opin Neurobiol* 9(4):410–418.
128. Fain GL, Matthews HR, Cornwall MC, Koutalos Y (2001) Adaptation in vertebrate photoreceptors. *Physiol Rev* 81(1):117–151.
129. Sampath AP, Matthews HR, Cornwall MC, Bandarchi J, Fain GL (1999) Light-dependent changes in outer segment free-Ca<sup>2+</sup> concentration in salamander cone photoreceptors. *J Gen Physiol* 113(2):267–77.
130. Bennett N, Dupont Y (1985) The G-protein of retinal rod outer segments (transducin). Mechanism of interaction with rhodopsin and nucleotides. *J Biol Chem* 260(7):4156–68.
131. Lerea CL, Bunt-Milam AH, Hurley JB (1989) Alpha transducin is present in blue-, green-, and red-sensitive cone photoreceptors in the human retina. *Neuron* 3(3):367–76.
132. Quazi F, Molday RS (2014) ATP-binding cassette transporter ABCA4 and chemical isomerization protect photoreceptor cells from the toxic accumulation of excess 11- *cis* -retinal. *Proc Natl Acad Sci* 111(13):5024–5029.
133. Dean DM, Nguitragool W, Miri A, McCabe SL, Zimmerman AL (2002) All-trans-retinal shuts down rod cyclic nucleotide-gated ion channels: A novel role for photoreceptor retinoids in the response to bright light? *Proc Natl Acad Sci* 99(12):8372–8377.
134. Brown PK, Gibbons IR, Wald G (1963) The visual cells and visual pigments of the mudpuppy, *Necturus*. *J Cell Biol* 19:79–106.
135. Baylor DA (1987) Photoreceptor signals and vision. Proctor lecture. *Invest Ophthalmol Vis Sci* 28(1):34–49.
136. Yau KW (1994) Phototransduction mechanism in retinal rods and cones. The Friedenwald Lecture. *Invest Ophthalmol Vis Sci* 35(1):9–32.
137. Burns ME (2010) Deactivation Mechanisms of Rod Phototransduction: The Cogan Lecture. *Investig Ophthalmology Vis Sci* 51(3):1283.
138. Lamb TD, Pugh EN (2006) Phototransduction, dark adaptation, and rhodopsin regeneration the proctor lecture. *Investig Ophthalmol Vis Sci* 47(12):5137–5152.
139. Wald G, Brown PK, Smith PH (1955) Iodopsin. *J Gen Physiol* 38(5):623–681.
140. Mahroo OAR, Lamb TD (2004) Recovery of the human photopic electroretinogram after bleaching exposures: estimation of pigment regeneration



- kinetics. *J Physiol* 554(2):417–437.
141. Sillman AJ, Ronan SJ, Loew ER (1991) Histology and microspectrophotometry of the photoreceptors of a crocodilian, *Alligator mississippiensis*. *Proc R Soc London Ser B Biol Sci* 243(1306):93–98.
  142. Smith WC, et al. (1995) Alligator rhodopsin : sequence and biochemical properties. *Exp Eye Res* 61(5):569–578.
  143. Crescitelli F, Dartnall HJA, Loew ER (1977) The gecko visual pigments: a microspectrophotometric study. *J Physiol* 268:559–573.
  144. Crescitelli F (1979) The gecko visual pigments. The behavior of opsin. *J Gen Physiol* 73(5):541–52.
  145. Crescitelli F (1984) The gecko visual pigment: the dark exchange of chromophore. *Vision Res* 24(11):1551–3.
  146. Zhang X, Wensel TG, Yuan C (2006) Tokay gecko photoreceptors achieve rod-like physiology with cone-like proteins. *Photochem Photobiol* 82(6):1452–60.
  147. Nemet I, Ropelewski P, Imanishi Y (2015) Rhodopsin Trafficking and Mistrafficking: Signals, Molecular Components, and Mechanisms. *Prog Mol Biol Transl Sci* 132:39–71.
  148. Pearring JN, Salinas RY, Baker SA, Arshavsky VY (2013) Protein sorting, targeting and trafficking in photoreceptor cells. *Prog Retin Eye Res* 36:24–51.
  149. Baylor DA, Lamb TD, Yau KW (1979) The membrane current of single rod outer segments. *J Physiol* 288:589–611.
  150. Yau K-W, Lamb TD, Baylor DA (1977) Light-induced fluctuations in membrane current of single toad rod outer segments. *Nature* 269(5623):78–80.
  151. Marty A, Neher E (1995) Tight-Seal Whole-Cell Recording. *Single-Channel Recording* (Springer US, Boston, MA), pp 31–52.
  152. Frederiksen R, et al. (2016) Rhodopsin kinase and arrestin binding control the decay of photoactivated rhodopsin and dark adaptation of mouse rods. *J Gen Physiol* 148(1):1–11.
  153. Chabre M, Breton J (1979) The orientation of the chromophore of vertebrate rhodopsin in the ‘meta’ intermediate states and the reversibility of the meta II-meta III transition. *Vision Res* 19(9):1005–18.
  154. Baylor DA, Lamb TD (1982) Local effects of bleaching in retinal rods of the toad. *J Physiol* 328:49–71.
  155. Mercer D (1960) Analytical methods for the study of periodic phenomena obscured by random fluctuations. *Cold Spring Harb Symp Quant Biol* 25:73–86.
  156. Molday RS, MacKenzie D (1983) Monoclonal antibodies to rhodopsin: characterization, cross-reactivity, and application as structural probes.

*Biochemistry* 22(3):653–660.

157. Palmiter RD, Sandgren EP, Avarbock MR, Allen DD, Brinster RL (1991) Heterologous introns can enhance expression of transgenes in mice. *Proc Natl Acad Sci U S A* 88(2):478–82.
158. Paix A, et al. (2017) Precision genome editing using synthesis-dependent repair of Cas9-induced DNA breaks. *Proc Natl Acad Sci* 114(50):E10745–E10754.
159. Jeon CJ, Strettoi E, Masland RH (1998) The major cell populations of the mouse retina. *J Neurosci* 18(21):8936–46.
160. Imamoto Y, Shichida Y (2014) Cone visual pigments. *Biochim Biophys Acta - Bioenerg* 1837(5):664–673.
161. Imai H, et al. (2005) Molecular properties of rod and cone visual pigments from purified chicken cone pigments to mouse rhodopsin in situ. *Photochem Photobiol Sci* 4(9):667–674.
162. Chen C-K, et al. (2010) Replacing the rod with the cone transducin subunit decreases sensitivity and accelerates response decay. *J Physiol* 588(2010):3231–3241.
163. Haynes L, Yau KW Cyclic GMP-sensitive conductance in outer segment membrane of catfish cones. *Nature* 317(6032):61–4.

## Appendix

### A.1 Convolution of 2 exponential-decay functions:

$$g(x) = e^{-\lambda_1 x}, \quad \text{where } \lambda_1 = \frac{1}{\tau_1}$$

$$f(x) = e^{-\lambda_2 x}, \quad \text{where } \lambda_2 = \frac{1}{\tau_2}$$

$$\begin{aligned}(f * g)(x) &= \int_0^x f(x-t) \times g(t) dt \\ &= \int_0^x e^{-[\lambda_2(x-t)]} \times e^{-\lambda_1(t)} \\ &= \int_0^x e^{-[\lambda_2(x-t)] - \lambda_1(t)}\end{aligned}$$

u-substitution

$$u = -[\lambda_2(x-t)] - \lambda_1(t)$$

$$u = -\lambda_2(x) + \lambda_2(t) - \lambda_1(t)$$

$$\frac{1}{\lambda_2 - \lambda_1} du = dt$$

$$(f * g)(x) = \frac{1}{\lambda_2 - \lambda_1} \int_0^x e^u du$$

$$= \frac{1}{\lambda_2 - \lambda_1} \left[ e^{-[\lambda_2(x-t)] - \lambda_1(t)} \right]_{t=0}^{t=x}$$

$$= \frac{1}{\lambda_2 - \lambda_1} \left[ e^{-\lambda_1(x)} - e^{-\lambda_2(x)} \right]$$

$$(f * g)(x) = e^{-\frac{x}{\tau_2}} * e^{-\frac{x}{\tau_1}} = \left( \frac{1}{\tau_2} - \frac{1}{\tau_1} \right)^{-1} \left[ e^{-\frac{x}{\tau_1}} - e^{-\frac{x}{\tau_2}} \right]$$

## A.2 Convolution of 3 exponential-decay functions:

$$g(x) = \frac{1}{\lambda_2 - \lambda_1} [e^{-\lambda_1(x)} - e^{-\lambda_2(x)}], \quad \text{where } \lambda_1 = \frac{1}{\tau_1} \text{ and } \lambda_2 = \frac{1}{\tau_2}$$

$$f(x) = e^{-\lambda_3 x}, \quad \text{where } \lambda_3 = \frac{1}{\tau_3}$$

$$\begin{aligned} (f * g)(x) &= \int_0^x f(x-t) \times g(t) dt \\ &= \int_0^x e^{-\lambda_3(x-t)} \times \frac{1}{\lambda_2 - \lambda_1} [e^{-\lambda_1(t)} - e^{-\lambda_2(t)}] dt \\ &= \frac{1}{\lambda_2 - \lambda_1} \int_0^x e^{-\lambda_3(x-t)} \times [e^{-\lambda_1(t)} - e^{-\lambda_2(t)}] dt \\ &= \frac{1}{\lambda_2 - \lambda_1} \int_0^x \{ [e^{-\lambda_3(x-t) - \lambda_1(t)}] - [e^{-\lambda_3(x-t) - \lambda_2(t)}] \} dt \\ &= \frac{1}{\lambda_2 - \lambda_1} \left( \int_0^x [e^{-\lambda_3(x-t) - \lambda_1(t)}] dt - \int_0^x [e^{-\lambda_3(x-t) - \lambda_2(t)}] dt \right) \end{aligned}$$

$$\begin{aligned} \int_0^x [e^{-\lambda_3(x-t) - \lambda_1(t)}] dt &= \frac{1}{\lambda_3 - \lambda_1} [e^{-[\lambda_3(x-t) - \lambda_1(t)]}]_{t=0}^{t=x} \\ &= \frac{1}{\lambda_3 - \lambda_1} [e^{-\lambda_1(x)} - e^{-\lambda_3(x)}] \end{aligned}$$

$$\int_0^x [e^{-\lambda_3(x-t) - \lambda_2(t)}] dt = \frac{1}{\lambda_3 - \lambda_2} [e^{-\lambda_2(x)} - e^{-\lambda_3(x)}]$$

$$\begin{aligned} &\frac{1}{\lambda_2 - \lambda_1} \left( \int_0^x [e^{-\lambda_3(x-t) - \lambda_1(t)}] dt - \int_0^x [e^{-\lambda_3(x-t) - \lambda_2(t)}] dt \right) \\ &= \frac{1}{\lambda_2 - \lambda_1} \left( \frac{1}{\lambda_3 - \lambda_1} [e^{-\lambda_1(x)} - e^{-\lambda_3(x)}] - \frac{1}{\lambda_3 - \lambda_2} [e^{-\lambda_2(x)} - e^{-\lambda_3(x)}] \right) \\ &= \left( \frac{1}{\lambda_2 - \lambda_1} \right) \left( \frac{1}{\lambda_3 - \lambda_1} \right) [e^{-\lambda_1(x)} - e^{-\lambda_3(x)}] - \left( \frac{1}{\lambda_2 - \lambda_1} \right) \left( \frac{1}{\lambda_3 - \lambda_2} \right) [e^{-\lambda_2(x)} - e^{-\lambda_3(x)}] \end{aligned}$$

$$e^{-\frac{x}{\tau_3}} * e^{-\frac{x}{\tau_2}} * e^{-\frac{x}{\tau_1}} = \left\{ \left( \frac{1}{\tau_2} - \frac{1}{\tau_1} \right)^{-1} \left( \frac{1}{\tau_3} - \frac{1}{\tau_1} \right)^{-1} \left[ e^{-\frac{x}{\tau_1}} - e^{-\frac{x}{\tau_3}} \right] \right\} - \left\{ \left( \frac{1}{\tau_2} - \frac{1}{\tau_1} \right)^{-1} \left( \frac{1}{\tau_3} - \frac{1}{\tau_2} \right)^{-1} \left[ e^{-\frac{x}{\tau_2}} - e^{-\frac{x}{\tau_3}} \right] \right\}$$

### A.3 Convolution of 4 exponential-decay functions:

$$g(x) = \frac{1}{\lambda_2 - \lambda_1} \left( \frac{1}{\lambda_3 - \lambda_1} [e^{-\lambda_1(x)} - e^{-\lambda_3(x)}] - \frac{1}{\lambda_3 - \lambda_2} [e^{-\lambda_2(x)} - e^{-\lambda_3(x)}] \right), \text{ where } \lambda_1 = \frac{1}{\tau_1}, \lambda_2 = \frac{1}{\tau_2}, \lambda_3 = \frac{1}{\tau_3}$$

$$f(x) = e^{-\lambda_4 x}, \text{ where } \lambda_4 = \frac{1}{\tau_4}$$

$$\begin{aligned} (f * g)(x) &= \int_0^x f(x-t) \times g(t) dt \\ &= \frac{1}{\lambda_2 - \lambda_1} \int_0^x \left\{ \left[ \frac{1}{\lambda_3 - \lambda_1} (e^{-\lambda_4(x-t) - \lambda_1(t)} - e^{-\lambda_4(x-t) - \lambda_3(t)}) \right] \right. \\ &\quad \left. - \left[ \frac{1}{\lambda_3 - \lambda_2} (e^{-\lambda_4(x-t) - \lambda_2(t)} - e^{-\lambda_4(x-t) - \lambda_3(t)}) \right] \right\} dt \end{aligned}$$

$$\begin{aligned} &e^{-\frac{x}{\tau_4}} * e^{-\frac{x}{\tau_3}} * e^{-\frac{x}{\tau_2}} * e^{-\frac{x}{\tau_1}} \\ &= + \left( \frac{1}{\tau_2} - \frac{1}{\tau_1} \right)^{-1} \left( \frac{1}{\tau_3} - \frac{1}{\tau_1} \right)^{-1} \left( \frac{1}{\tau_4} - \frac{1}{\tau_1} \right)^{-1} \left[ e^{-\frac{x}{\tau_1}} - e^{-\frac{x}{\tau_4}} \right] \\ &\quad - \left( \frac{1}{\tau_2} - \frac{1}{\tau_1} \right)^{-1} \left( \frac{1}{\tau_3} - \frac{1}{\tau_1} \right)^{-1} \left( \frac{1}{\tau_4} - \frac{1}{\tau_3} \right)^{-1} \left[ e^{-\frac{x}{\tau_3}} - e^{-\frac{x}{\tau_4}} \right] \\ &\quad - \left( \frac{1}{\tau_2} - \frac{1}{\tau_1} \right)^{-1} \left( \frac{1}{\tau_3} - \frac{1}{\tau_2} \right)^{-1} \left( \frac{1}{\tau_4} - \frac{1}{\tau_2} \right)^{-1} \left[ e^{-\frac{x}{\tau_2}} - e^{-\frac{x}{\tau_4}} \right] \\ &\quad + \left( \frac{1}{\tau_2} - \frac{1}{\tau_1} \right)^{-1} \left( \frac{1}{\tau_3} - \frac{1}{\tau_2} \right)^{-1} \left( \frac{1}{\tau_4} - \frac{1}{\tau_3} \right)^{-1} \left[ e^{-\frac{x}{\tau_3}} - e^{-\frac{x}{\tau_4}} \right] \end{aligned}$$

## A.4 Shape Factor for the convolution of 2 exponential-decay functions

### Shape Factor in Noise Analysis

I. Campbell's theorem:

$$\sigma^2 = v \times a^2 \int_0^\infty f(t)_N^2 dt$$

$$m = v \times a \int_0^\infty f(t)_N dt$$

II. Estimating elementary event amplitude of shot noise, a:

$$a = \frac{\sigma^2}{m} \times \frac{\int_0^\infty f(t)_N dt}{\int_0^\infty f(t)_N^2 dt}$$

Where  $\frac{\int_0^\infty f(t)_N dt}{\int_0^\infty f(t)_N^2 dt}$  is referred to as a "shape factor" because it varies according to the equation used to describe the elementary event (Katz & Miledi, 1972)

$1 \leq \frac{\int_0^\infty f(t)_N dt}{\int_0^\infty f(t)_N^2 dt} \leq 2$  for equations used to describe the time course of physiological responses (e.g. a square wave, a single-exponential decay, a convolution of exponential-decay functions)

### Shape Factor for a convolution of 2 exponential-decay functions ( $\tau_1 = 0.247$ s and $\tau_2 = 0.08$ s)

I. Convolution of 2 exponential-decay functions:

$$(f * g)(x) = e^{-\frac{x}{\tau_2}} * e^{-\frac{x}{\tau_1}} = \left(\frac{1}{\tau_2} - \frac{1}{\tau_1}\right)^{-1} \left[ e^{-\frac{x}{\tau_1}} - e^{-\frac{x}{\tau_2}} \right]$$

II. Calculate Shape Factor:  $\frac{\int_0^\infty f(t)_N dt}{\int_0^\infty f(t)_N^2 dt}$

$$\int_0^\infty f(t)_N dt = \int_0^\infty N \times \left[ \left(\frac{1}{\tau_2} - \frac{1}{\tau_1}\right)^{-1} \left[ e^{-\frac{x}{\tau_1}} - e^{-\frac{x}{\tau_2}} \right] \right]$$

$$= \left[ N \times \left(\frac{1}{\tau_2} - \frac{1}{\tau_1}\right)^{-1} \right] \left[ \left[ -\tau_1 \times e^{-\frac{x}{\tau_1}} \right]_0^\infty - \left[ -\tau_2 \times e^{-\frac{x}{\tau_2}} \right]_0^\infty \right]$$

$$\int_0^\infty f(t)_N dt = 0.42$$

where N is a normalization factor required to adjust the peak of the function to unity ( $N = 21.2$ )

$$\int_0^\infty f(t)_N^2 dt = \int_0^\infty N^2 \times \left[ \left(\frac{1}{\lambda_2 - \lambda_1}\right)^2 (e^{-2\lambda_1(t)} - e^{-\lambda_1(t) - \lambda_2(t)} - e^{-\lambda_2(t) - \lambda_1(t)} + e^{-2\lambda_2(t)}) \right]$$

$$= \left[ N^2 \times \left(\frac{1}{\lambda_2 - \lambda_1}\right)^2 \right] \times \left[ \frac{1}{-2\lambda_1} e^{-2\lambda_1(t)} - \frac{1}{-\lambda_1 - \lambda_2} (e^{-\lambda_1(t) - \lambda_2(t)} - 1) - \frac{1}{-\lambda_2 - \lambda_1} (e^{-\lambda_2(t) - \lambda_1(t)} - 1) + \frac{1}{-2\lambda_2} e^{-2\lambda_2(t)} \right]_0^\infty$$

$$\int_0^\infty f(t)_N^2 dt = 0.27$$

where  $\lambda_1 = 1/\tau_1$  and  $\lambda_2 = 1/\tau_2$

$$\boxed{\frac{\int_0^\infty f(t)_N dt}{\int_0^\infty f(t)_N^2 dt} = 1.56}$$

## A.5 Convolution of the single-G<sub>T</sub>\*PDE\* electrical response with the REY-Rho\*

### G<sub>T</sub>\*PDE\* lifetime probability density function:

Single-G<sub>T</sub>\*PDE\* electrical response (approximation from apo-opsin noise analysis):

$$g(t) = A \times \frac{1}{\lambda_2 - \lambda_1} [e^{-\lambda_1(t)} - e^{-\lambda_2(t)}], \quad \text{where } \lambda_1 = \frac{1}{\tau_1} \text{ and } \lambda_2 = \frac{1}{\tau_2} \text{ and } A \text{ is an amplitude factor}$$

Probability density function of REY-Rho\* G<sub>T</sub>\*PDE\* (time integral equal to 1):

Convolution of two exponential probability density functions:

$$f(t) = [\lambda_3 e^{-\lambda_3 t}] * [\lambda_4 e^{-\lambda_4 t}], \quad \text{where } \lambda_1 = \frac{1}{\tau_1} \text{ and } \lambda_2 = \frac{1}{\tau_2} \text{ and } A \text{ is an amplitude factor}$$

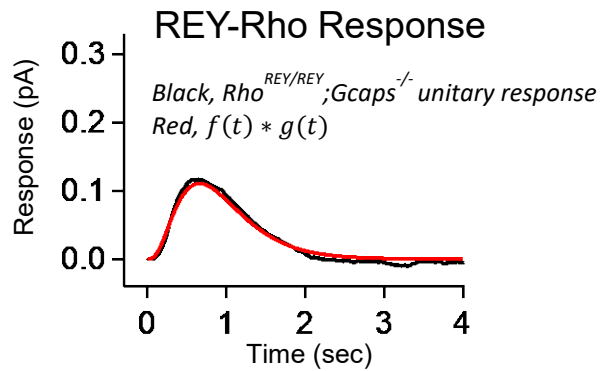
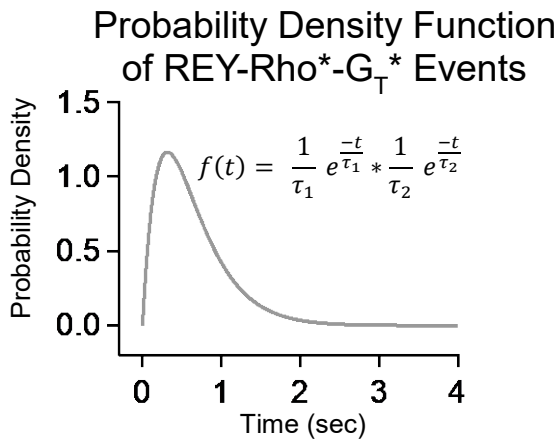
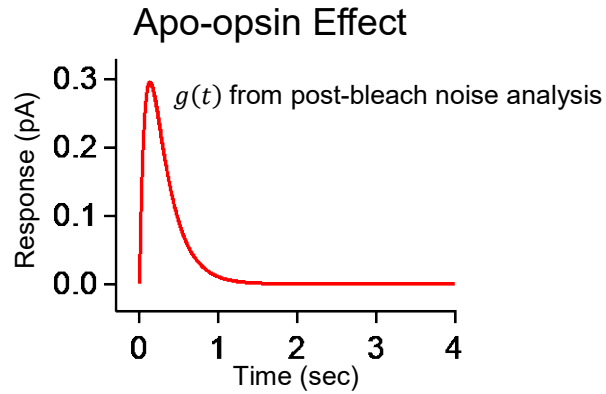
Measured REY-Rho\* quantal responses (Single-G<sub>T</sub>\*PDE\* event stretched by the above probability density function)

$$f(t) * g(t)$$

$$\begin{aligned} & \left( A \times \frac{1}{\lambda_2 - \lambda_1} [e^{-\lambda_1(t)} - e^{-\lambda_2(t)}] \right) * \left( [\lambda_3 e^{-\lambda_3 t}] * [\lambda_4 e^{-\lambda_4 t}] \right) \\ & = +\{[(A \times \lambda_4 \times \lambda_3) \times (\lambda_2 - \lambda_1) - 1] \times (\lambda_3 - \lambda_1) - 1 \times (\lambda_4 - \lambda_1) - 1 \times (e^{-\lambda_1(t)} - e^{-\lambda_4(t)})\} \\ & \quad -\{[(A \times \lambda_4 \times \lambda_3) \times (\lambda_2 - \lambda_1) - 1] \times (\lambda_3 - \lambda_1) - 1 \times (\lambda_4 - \lambda_3) - 1 \times (e^{-\lambda_3(t)} - e^{-\lambda_4(t)})\} \\ & \quad -\{[(A \times \lambda_4 \times \lambda_3) \times (\lambda_2 - \lambda_1) - 1] \times (\lambda_3 - \lambda_2) - 1 \times (\lambda_4 - \lambda_2) - 1 \times (e^{-\lambda_2(t)} - e^{-\lambda_4(t)})\} \\ & \quad +\{[(A \times \lambda_4 \times \lambda_3) \times (\lambda_2 - \lambda_1) - 1] \times (\lambda_3 - \lambda_2) - 1 \times (\lambda_4 - \lambda_3) - 1 \times (e^{-\lambda_3(t)} - e^{-\lambda_4(t)})\} \end{aligned}$$

## A.6 Convolution of the single- $G_T^*$ response with the REY-R\* lifetime distribution

(Example):





## A.7 Simulating a Poisson Process in MATLAB:

```
% Install Wavelet toolbox before simulation
lambda=10; % arrival rate per second
T=30; % simulation time in second
delta=0.01; % simulation step size in second
N=T/delta; % number of simulation steps
event=zeros(N,1); % array recording at each step if a "packet"
arrived.

% initialize it to zeros
R=rand(size(event)); % generate a random array (with elements in
[0,1]) of the same size as "event"
event(R<lambda*delta)=1; % set each element of event to 1 with
probability lambda*delta
inds=find(event==1); % getting indices of arrival
int_times=diff(inds)*delta; % interarrival times in seconds
edges=0:0.01:1; % define histogram bin
count=histc(int_times,edges);
figure; bar(edges,count,'histc'); % draw histogram of absolute
count
figure; bar(edges,count/sum(count)/(edges(2)-edges(1)),'histc');
% hdraw histogram of normalized counts
hold;plot(edges,lambda*exp(-lambda*edges),'r'); % plot
theoretical result
legend('simulation','theoretical');
cumint_times = cumsum(int_times)
t = 0:0.01:T; %create time base
numWaves = length(int_times); %define number of waves to create
waves = zeros(numWaves,length(t)); %create strings of zeroes of
length t
allwaves = [];
for i = 1:numWaves %Repeat statements a specific number of times
    randExpBeg = cumint_times(i); %Generate exponentially
    distributed up times
    ExpBeg(i) = randExpBeg; %Defines upTime for each wave

    %Exponential-decay function%
    Tau = 0.2; %define Tau
    wave = 1*exp(-t/Tau); %define exponential decay function

    % 1-D extension length.
    l = single((sym(randExpBeg) ./ 0.01));
    r = length(wave) - 1;

    % Zero-padding extensions 1-D.
    xextzpdLEFT = wextend('1D','zpd',wave,l,'l');
    xextzpdRIGHT = wextend('1D','zpd',xextzpdLEFT,r,'r');
    x = 0:0.01:(length(xextzpdRIGHT)-1)*0.01);
    xextzpdLEFT;
    xextzpdRIGHT;
```

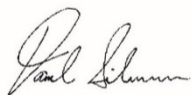
```
    allwaves = [allwaves ; xextzpdRIGHT];
    ALLWAVES = abs(allwaves);
    hold on %stores each wave on graph

end

randomnoise = sum(ALLWAVES);
z = 0:0.01:((length(xextzpdRIGHT)-1)*0.01);
figure(3);
plot(z,randomnoise); %plot simulated Poisson process
```

## CURRICULUM VITAE FOR Ph.D. CANDIDATES

The Johns Hopkins University School of Medicine



---

Name (Daniel Silverman)

October 30, 2018

---

Date of this version

### **Educational History:**

Ph.D. expected	2018	Biochemistry, Cellular and Molecular Biology Adviser: King-Wai Yau, Ph.D.	Johns Hopkins University School of Medicine
B.S.	2010	Biochemistry and Molecular Biology; Minor in Statistics	The Pennsylvania State University

### **Other Professional Experience:**

Research fellow	2010-2012	Laboratory of Joseph A. Mindell, MD/Ph.D.	NIH, NINDS
Research assistant	2008	Laboratory of J. Greg Ferry, Ph.D.	The Pennsylvania State University
Summer intern	2007	Laboratory of Jonathan L. Katz, Ph.D.	NIH, NIDA

### **Scholarships, fellowships, or other external funding:**

Visual Science Training Program fellowship, EY007143, 2016-2018  
2-year stipend and travel funding  
NIH Intramural Research Training Award, 2010-2012  
2-year stipend and travel funding  
Center for Environmental Chemistry and Geochemistry summer fellowship, 2008  
3-month stipend

### **Academic and other honors:**

Schreyer Honors College Ambassador Travel Grant, 2009  
Dean's List, Eberly College of Science, semester GPA  $\geq 3.50$ , 6 out of 8 semesters

### **Publications, peer reviewed:**

Yue W.W.S.\*, Silverman D.\*, Ren X., Frederiksen R., Sakai K., Yamashita T., Shichida Y., Cornwall M.C., Chen J., Yau K-W. Elementary Response Triggered by Transducin in Retinal Rods. Manuscript being reviewed for publication in *Proc. Natl. Acad. Sci., USA*.

\*Equal contribution

**Posters and abstracts:**

**Silverman D.**, Yue W.W.S., Ren X., Frederiksen R., Sakai K., Yamashita T., Shichida Y., Cornwall M.C., Chen J., Yau K-W. The apo-opsin effect in retinal rods. FASEB: Retinal Neurobiology and Visual Processing. Olean, NY. June 24-29, 2018. (Poster)

**Silverman D.**, Yue W.W.S., Ren X., Frederiksen R., Sakai K., Yamashita T., Shichida Y., Cornwall M.C., Chen J., Yau K-W. The apo-opsin effect in retinal rods. Biochemistry, Cellular and Molecular Biology program retreat. Cambridge, MD. October 8, 2017. (Invited talk)

Yue W.W.S.\*, **Silverman D.\***, Ren X., Frederiksen R., Sakai K., Yamashita T., Shichida Y., Cornwall M.C., Chen J., Yau K-W. Effect of a single transducin molecule in mouse rods. FASEB: Biology and Chemistry of Vision. Steamboat Springs, CO. June 25-30, 2017. (Invited talk given by W.W.S. Yue)

**Silverman D.**, Mindell J.A. Dissection of Proton-Inhibition Mechanism in the Cl<sup>-</sup>/H<sup>+</sup> exchanger, ClC-7. 57<sup>th</sup> Annual Meeting of the Biophysical Society. Philadelphia, PA. February 2-6, 2013.

\*Equal contribution

**Service and Leadership:**

University Health Services Wellness Committee, 2018

Monthly meetings to discuss projects aiming to support mental health and wellness of graduate students at Johns Hopkins University

Junior Biomedical Scholars Program, 2013

Worked with a high school student from Paul Laurence Dunbar High School to prepare a poster from a literature review; student awarded 1st place in public health research.